TRIBOELECTRIC SENSOR DESIGNED FOR PARKINSON'S DISEASE MONITORING

SIRINYA UKASI

Graduate School Srinakharinwirot University

2023

การออกแบบไทรโบอิเล็กทริกเซ็นเซอร์สำหรับการติดตามโรคพาร์กินสัน

สิรินยา อุกาสี

TRIBOELECTRIC SENSOR DESIGNED FOR PARKINSON'S DISEASE MONITORING

SIRINYA UKASI

A Thesis Submitted in Partial Fulfillment of the Requirements

for the Degree of MASTER OF SCIENCE

(Materials Science)

Faculty of Science, Srinakharinwirot University

2023

THE THESIS TITLED

TRIBOELECTRIC SENSOR DESIGNED FOR PARKINSON'S DISEASE MONITORING

BY

SIRINYA UKASI

HAS BEEN APPROVED BY THE GRADUATE SCHOOL IN PARTIAL FULFILLMENT

OF THE REQUIREMENTS FOR THE MASTER OF SCIENCE

IN MATERIALS SCIENCE AT SRINAKHARINWIROT UNIVERSITY

(Assoc. Prof. Dr. Chatchai Ekpanyaskul, MD.)

Dean of Graduate School

ORAL DEFENSE COMMITTEE

.... Major-advisor

(Dr.Thitirat Charoonsuk)

.... Co-advisor

(Prof. Dr.Naratip Vittayakorn)

.... Chair

(Assoc. Prof. Dr.Saichon Sriphan)

.... Committee

(Asst. Prof. Dr.Panitarn Wanakamol)

Title	TRIBOELECTRIC SENSOR DESIGNED FOR PARKINSON'S DISEASE MONITORING
Author	SIRINYA UKASI
Degree	MASTER OF SCIENCE
Academic Year	2023
Thesis Advisor	Dr. Thitirat Charoonsuk
Co Advisor	Prof. Dr. Naratip Vittayakorn

Parkinson's disease (PD) is a neurodegenerative disorder that affects movement control and monitoring the progression of PD, is crucial for effective management and treatment. Current wearable sensors for PD monitoring are bulky and uncomfortable due to battery dependence. Therefore, it is essential to seek out new alternatives for wearable sensing devices. This work introduces a wristwatch-like triboelectric sensor (WW-TES) inspired by automatic watches for PD tremor monitoring. The WW-TES features a free-standing mode with a stainless-steel oscillating plate and a surface-modified PTFE film housed in a 3D-printed PLA frame. The designed device is circular with a diameter of 34 mm, a height of 7 mm, and a side wall thickness of 2 mm, featuring a central platform for a metal oscillating plate and two contact points for. Key parameter of electrode distance was optimized to enhance the sensor's output signal and found that 5 mm distance produced the highest peak amplitude. The fabricated device was also tested by changing input frequency of mechanical vibration to observe the discriminant of electrical output signal. The results showed that this device could effectively respond to frequency changes, allowing differentiation of tremor severity through tracking the electrical output signal amplitude. Operating this device through activities of daily living (ADLs) such as pouring, eating and writing was also validated. The Wavelet Packet Transform (WPT) software was used to analyze the signal and confirmed the demonstration of varying signal amplitudes corresponding to tremor severity levels within the MDS-UPDRS Scale. It can be concluded WW-TES holds significant potential for enhancing PD monitoring technology, aiding in screening the disease and leading to more effective treatments and quality of life for patients.

Keyword : Triboelectric sensor (TES), Parkinson's disease (PD), Tremor sensor

ACKNOWLEDGEMENTS

SIRINYA UKASI

TABLE OF CONTENTS

LIST OF TABLES

LIST OF FIGURES

CHAPTER 1

INTRODUCTION

Background and Significance of the Research

Parkinson's disease (PD) is a progressive nervous system disorder causing involuntary movements, tremors, stiffness, and coordination issues (1, 2). PD typically impairs daily functioning, making routine activities more challenging and gradually diminishing the patient's quality of life. Severity of the PD symptoms can be controlled by medications, causing side effects with long-term taking. Some individuals may experience sudden changes in movement, especially dyskinesia (3), when the body reaches the maximum dose of medication (4). The specialist must adjust the proper medication doses to limit these side effects. To do this, quantifying the progression of PD and creating personalized treatment plans by tracking PD symptoms and drug response are critical.

Patients with PD typically engage in symptom monitoring through daily diaries (5), and subsequently meet with clinicians on a monthly basis. They primarily self-report their symptoms, which may introduce inherent bias into the self-reporting process (6). The current state of symptom tracking has obvious limitations, including inconvenient daily diaries, infrequent clinical sessions, and incompletely self-reported symptoms. To address these challenges, wearable electronic (WE) devices are being proposed to provide autonomous tracking, continuous monitoring during functional activities, and collecting of a complete symptom profile. Those WE devices could have an impact on the diagnosis, treatment, and drug development of PD. The clinician can be helped to assess the current state of PD patients and assist them in deciding about the right type and amount of medication at the right time. Over the last decade, wearable sensors for PD applications have received increased attention. The most widely use of PD sensors are the internal sensors such as gyroscopes (GYRO) (7), three-triaxial accelerometers (ACC) (8), magnetometers and electromyographic (EMG) (9) that commonly combined in an inertial measurement unit (IMU)s (10, 11). Previous studies have used those kinds

of sensor to detect and distinguish motor and non-motor PD symptoms by detecting signal for identifying unique traits, such as the patient's shuffling steps, hesitations, sudden movement changes, and abnormal shaking (8, 12-15). However, these WE sensors use traditional electrochemical batteries, which need to be recharged or replaced. Also, their bulky size and heavy weight normally cause discomfort or restriction of patient's mobility. This inconvenience can deter patients from using the devices consistently. Moreover, the devices may also experience structural issues under repeated stress and may not excel at detecting low-frequency body motion (16, 17). Therefore, these challenges need to be addressed in order to develop a new kind of PD sensor.

Triboelectric nanogenerators (TENG) offer significant promise as a valuable component of WE devices with their energy harvesting capabilities. TENG can generate electricity by converting mechanical energy, such as motion or vibrations, through the triboelectric effect and electrostatic induction of two different materials (18-20). Owing to its ability to generate electrical signals from mechanical energy at low frequency, the TENG can be served as self-power sensor, especially by detecting signal from human motion. Using principle of triboelectric effect for inventing sensor is called triboelectric sensor (TES) that has been applied to various fields of applications such as physical activity tracking in sports and fitness (21-23) and healthcare for health monitoring (23-26). Hence, TES technology holds the potential to be applied as a sensor for measuring symptoms of PD (27). In recent years, research has been conducted to adapt TES as PD sensors or assistive devices. Li R *et al.* (28) designed a self-powered smart wearable based on a TENG composed of polytetrafluoroethylene (PTFE) and iron (Fe) ball as tribomaterials to generate electrical signal associated with the wearer's movement for tracking physical activities. Nonetheless, due to the closed cylindrical configuration, the Fe ball can exhibit motion in both a circular and vertical direction, potentially causing interference among the resulting electrical signals from undistinguished ball direction. Vera Anaya D *et al.* (29) designed a stretchable triboelectric sensor based on Ecoflex[TM] and aluminum for measuring muscle movements of PD patients. The sensor captured

data for disease progression insights, yet challenging sensor placement on finger tendons may impact performance, as hand tremors affect all hand muscle groups. Moreover, sensors that measure muscle are limited by individual variations in fat and tissue characteristics. Kim J N *et al.* (30) developed a self-powered tremor sensor for PD patients using a self-healing hydrogel TENG composed of catechol, chitosan, and diatom. The M-shaped TENG sensor detects tremors, with the output signal containing information about tremor frequency, amplitude, and patterns in individuals with PD. Although previous publications have developed sensors for PD using the concept of TES, the challenges still remain, including unsuitable structures for body attachment, causing discomfort to wear and potential interference with daily life or activities. Also, the presence of interference normally provides low signal-to-noise ratio of electrical output, resulting in the difficulty to distinguish between the small signal amplitude and ambient noise (31). Therefore, further design and development of TES with important characteristics of high signal-to-noise ratio, light weight, comfortable to wear with cost-effective is in demand. Therefore, the aim of the work is to design and develop a wrist-wearable sensor inspired by an automatic-watch for PD symptom tracking, without compromising its performance. In order to design the TES for PD monitoring, many parameters should be considered, including material selection and modification, appropriate operation mode fabrication and suitable structural design. Material pair should be selected with contrasting electron affinities to enhance the abilities of electron donating and receiving (32, 33). The modification of the material surface is needed to create surface structures to improve contact efficiency and the sensitivity to mechanical forces (34-36). The appropriate operating mode is critical to design because each mode contain their own character for specific application (37-39). The structural design was also important (40) to demonstrate the effectiveness of TES for capturing biomechanical movements and gestures (41, 42). The mentioned parameters contain the significant potential to enhance the signal-to-noise ratio of the TES, increase the responsiveness to mechanical forces, and facilitate the integration into practical applications.

A wearable triboelectric sensor (WTES) will be custom-built for the purpose of monitoring PD tremor in this study. The development process will involve designing a TES in the free-standing mode using stainless steel and polytetrafluoroethylene (PTFE), with a focus on optimizing the effective parameters on its electrical output, including material surface modification, electrode distance, and frequency. Material characteristics will also be investigated and confirmed. To examine the surface morphology and identification of functional groups of PTFE, scanning electron microscopy (SEM), atomic force microscopy (AFM), and Attenuated Total Reflectance Fourier Transform Infrared Spectroscopy (ATR-FTIR) will be utilized. Electron Backscatter Diffraction (EBSD) will be used to identify stainless steel. The electrical output characteristics, including open circuit output voltage (V_{OC}) and short circuit output current (I_{SC}) of TES, will be studied in relation to the aforementioned parameters using an oscilloscope and a digital multimeter (DMM). Upon achieving the optimum condition, practical application of TES for PD will be studied through activity testing, including several tasks such as water pouring, eating, writing, and more. Overall, the results of this research will provide valuable insights into the development and optimization of wearable sensors for monitoring PD tremor.

Objective of the Study

1. To develop a triboelectric sensor (TES) device that can be used for monitoring Parkinson's disease (PD).

2. To investigate the impact of crucial parameters of the TES device on the electrical output signal.

3. To comprehend the mechanism of charge transfer on the designed triboelectric sensor.

4. To evaluate the practical application of the TES device for detecting PD activity.

Scope of the Study

      1. Develop a TES device for monitoring PD in free-standing mode, utilizing stainless steel and polytetrafluoroethylene (PTFE) as triboelectric materials.

      2. Investigate the impact of crucial parameters such as material surface roughness, electrode distances, and frequency on the electrical output signal, based on open circuit voltage (V_{OC}) and short circuit current (I_{SC}).

      3. Analyze the mechanism of charge transfer on the triboelectric sensor designed for the study.

      4. Evaluate the practical application of the TES device for detecting PD activity by simulating patient situations involving daily activities such as water pouring, eating, and writing.
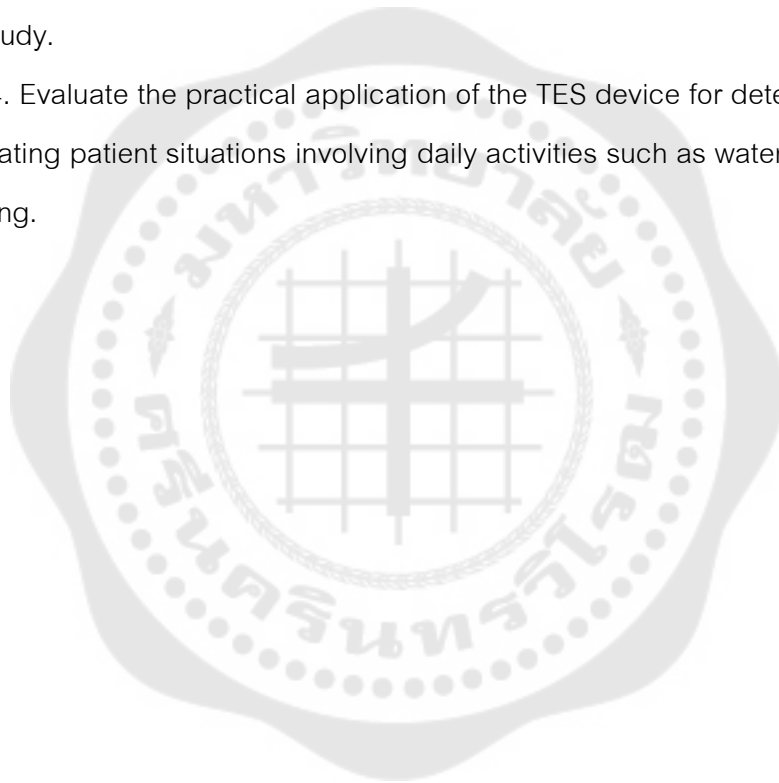
Conceptual Framework
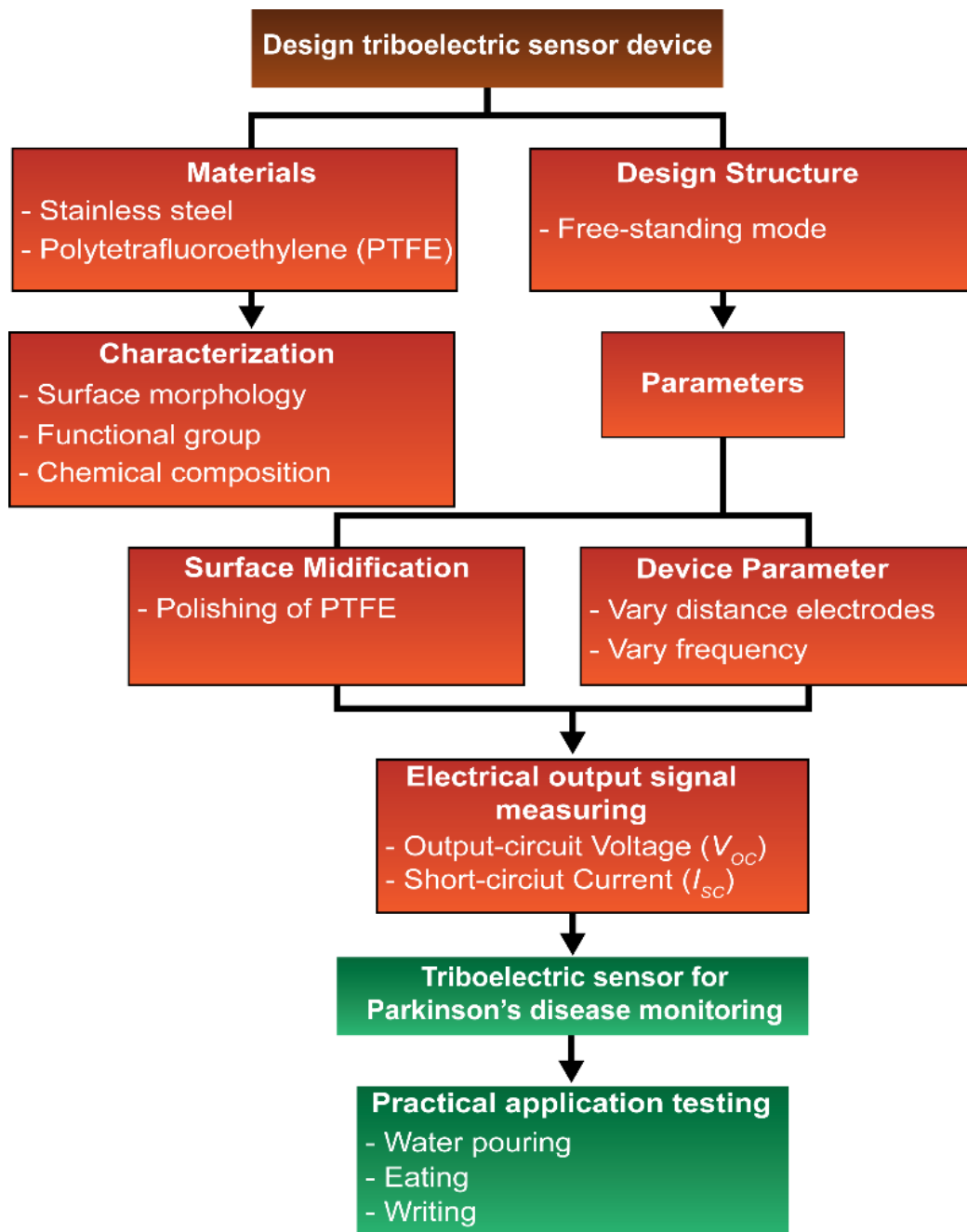
Figure 1 Conceptual Framework

Expected Outcome

        The findings from this work can be used to benefit as follow:

        1. Obtain TES device for Parkinson's disease (PD) monitoring.

        2. Understand the effect of important parameters, including material surface roughness, electrode distances and frequency on the electrical output signal based on open circuit voltage (V_{OC}) and short circuit current (I_{SC}).

        3. Understand the charge transferred mechanism in designed triboelectric sensor.

        4. Obtain the signal of PD activity detection from the designed TES device by simulating patient situation with daily activities, including water pouring, eating and writing.
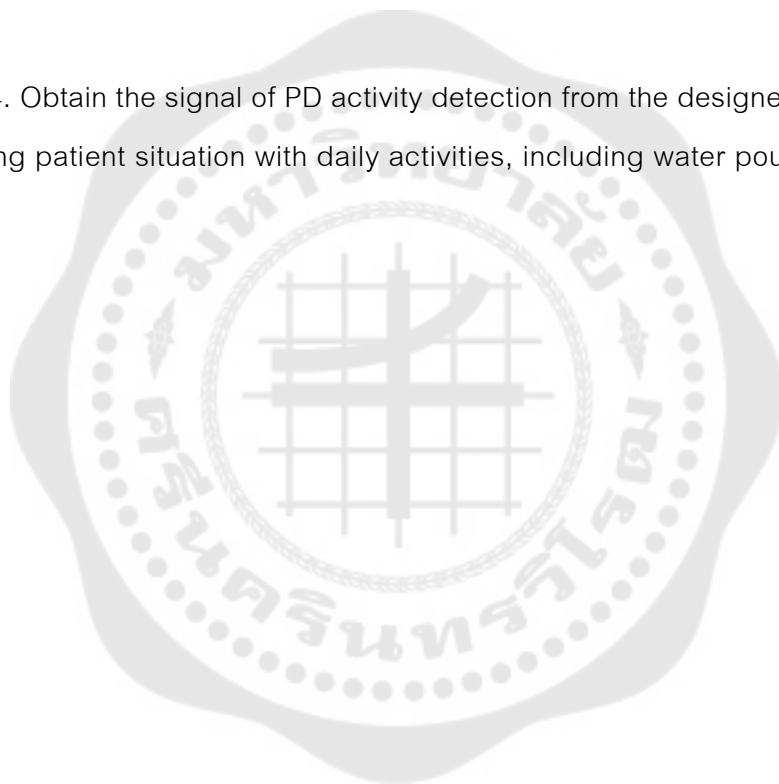
CHAPTER 2

LITERATURE REVIEW

2.1 Parkinson's Disease (PD)

Parkinson's disease (PD) is the second most common neurodegenerative disease after Alzheimer's disease (AD) (43). The number of people with Parkinson's disease will be on the rise until 2030 (Figure 2). PD is commonly associated with a progressive neurodegenerative disorder that primarily affects movement control. The exact cause of Parkinson's disease is not known, although it is believed to be a combination of genetic and environmental factors. Mutations in certain genes have been related to a higher risk of developing the disease (1). One of the key features of PD is a deficiency of the neurotransmitter dopamine in certain areas of the brain (44). Dopamine plays a crucial role in regulating various motor and non-motor functions in the brain, and its deficiency leads to the characteristic symptoms of PD. PD is characterized by a range of motor and non-motor symptoms, which is the results from the loss of dopamine-producing neurons in a specific area of the brain called the substantia nigra (45).
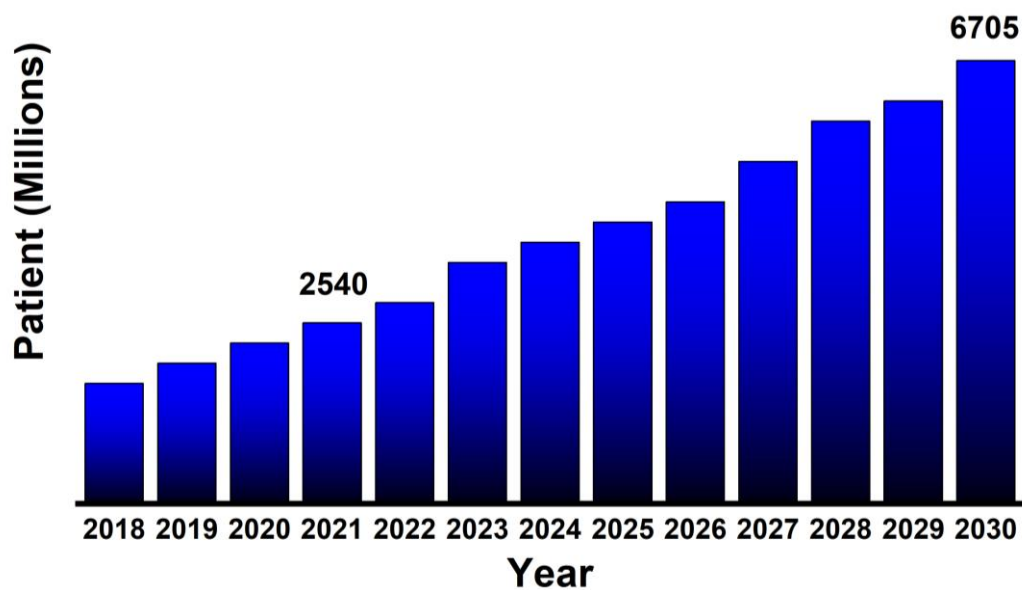
Figure 2 Parkinson's disease trend from 2018 to 2030

Source:https://www.globenewswire.com/newsrelease/2022/09/05/2509862/0/en/Parkinso
n-s-Disease-Market-Size-Will-Achieve-USD-6-705-Million-by-2030-growing-at-11-5-
CAGR-Exclusive-Report-by-Acumen-Research-and-Consulting.html

2.1.1 Motor Symptoms

PD associated with the loss of dopamine-producing neurons in the substantia nigra. Dopamine is a neurotransmitter that plays a crucial role in regulating movement. As dopamine levels decrease, it leads to motor symptoms. As dopamine-producing neurons die off, there is a significant reduction in dopamine levels in the brain. This deficiency disrupts the normal communication between brain regions responsible for motor control. The hallmark motor symptoms of PD, including resting tremors, bradykinesia (slowness of movement), rigidity, and postural instability, are directly related to this dopamine deficiency. Motor symptoms include: 1) Tremors: Involuntary shaking, usually starting in one hand often described as a resting tremor (46). 2) Bradykinesia: Slowness of movement (47) , making tasks like buttoning a shirt or walking difficult. 3) Rigidity: Stiffness of muscles (48) , which can lead to joint pain and limited range of motion. 4) Postural instability: Difficulty maintaining balance (49), leading to a

higher risk of falls. These symptoms typically become more pronounced as the disease progresses and dopamine levels continue to decline. In addition to motor symptoms, dopamine deficiency in Parkinson's disease can also lead to non-motor symptoms, including mood disorders, cognitive changes, and autonomic dysfunction.

2.1.2 Non-motor Symptoms

PD is often recognized for its motor symptoms, such as tremors, bradykinesia (slowness of movement), rigidity, and postural instability. However, PD can also manifest a variety of non-motor symptoms, which can significantly impact a person's quality of life.

Non-motor symptoms may include depression, anxiety, sleep disturbances, constipation, and cognitive changes (50-52). It's important to mention that non-motor symptoms of Parkinson's disease (PD) can vary greatly from person to person, and not everyone with PD will experience all of them. In addition, non-motor symptoms can have a significant impact on a person's daily life and should be discussed with a healthcare professional for appropriate management and treatment. Addressing non-motor symptoms is an important aspect of comprehensive care for people with PD.

2.2 Diagnosis

The diagnosis of PD typically involves a combination of clinical evaluation, medical history assessment, and sometimes specialized tests. Here is an overview of the diagnostic process for Parkinson's disease:

2.2.1 Medical History and Clinical Examination

A healthcare provider, often a neurologist or movement disorder specialist, will start by taking a detailed medical history. The patient's symptoms, progression and family history are asked. A thorough physical examination is carried out to assess motor function, muscle stiffness, balance and coordinate (53).

2.2.2 Observation of Symptoms

PD is primarily diagnosed by the presence of characteristic motor symptoms. To confirm the diagnosis, the clinicians will monitor the symptoms over time to determine whether symptoms meet the criteria for Parkinson's disease (54).

2.2.3 Neuroimaging

In some cases, neuroimaging studies like magnetic resonance imaging (MRI) (55) or dopamine transporter imaging (DaTscan) may be recommended (56). These tests can help rule out other conditions that may mimic PD or provide supportive evidence for the diagnosis.

For patients' health, a timely and accurate diagnosis of PD is essential. It opens the door to tailored treatment options, access to clinical trials and improved quality of life. It also addresses the wider emotional, psychological and practical aspects of living with the disease.

2.3 Symptoms Tracking and Monitoring

For following a PD diagnosis, continuous symptom tracking and monitoring play a pivotal role in effectively managing the condition. Regular monitoring can help people with PD and the healthcare team make informed decisions about the treatment plan. Several methods are commonly used to monitor PD symptoms.

2.3.1 Symptom Diary or Journal

A PD symptom diary or journal (6) is a valuable tool used by individuals with PD to track and record their symptoms, medication schedules, and daily experiences. By consistently recording symptoms and medication intake, individuals can assess the effectiveness of their treatment plans over time. This information can be invaluable in discussions with healthcare providers when adjusting medication or exploring alternative therapies. However, there are challenges associated with diary design, including selecting an appropriate format, determining the frequency of data collection, and ensuring cultural sensitivity (57). In addition, since symptom diaries rely heavily on patient self-description, there is the potential for inherent bias in the self-reporting process. The example of a completed symptom diary that was given to the participants is shown in Table 1.

Table 1 The example symptom diary provided for participants

Time (AM) Start at Midnights	ON	On with troublesome dyskinesia	OFF	Asleep
12:00-1:00 am				X
1:00-2:00 am				X
2:00-3:00 am				X
3:00-4:00 am				X
4:00-5:00 am				X
5:00-6:00 am				X
6:00-7:00 am				X
7:00-8:00 am			X	
8:00-9:00 am	X			
9:00-10:00 am	X			
10:00-11:00 am		X		
11:00-12:00 pm			X	

2.3.2 Telemedicine and Video Conferencing

PD telemedicine and video conferencing refer to the use of digital communication technologies to provide medical care and support to individuals living with PD. This approach allows patients to consult with healthcare providers, specialists, or support groups remotely, using video calls, online platforms, or other digital means (58). It can involve a range of services, including remote consultations, monitoring of symptoms and treatment progress, and the provision of education and emotional support. All deliver through telecommunication technologies. Healthcare providers can use video conferencing to remotely assess and interact with patients, monitor their symptoms, adjust treatment plans as needed, and provide ongoing support (Figure 3). While this approach offers several advantages, it also presents challenges, including the

need for reliable internet connections, concerning about the privacy and security of medical data, and getting limitations in terms of physical examinations (59).

Figure 3 Telemedicine and Video Conferencing between patient and the healthcare provider.

Source: https://www.pexels.com/photo/people-on-a-video-call-4225920/

2.3.3 Mobile Apps and Digital Platforms

Mobile apps and digital platforms (Figure 4) refer to software and online tools that are specifically designed to help individuals with PD, monitor symptoms, and tracking patient progression (60). Several apps offer exercise routines and physical therapy programs tailored to individuals with PD. These exercises can help to improve mobility, balance, and overall physical well-being. It's worth noting that the effectiveness of these apps can vary, and not all may be suitable for everyone. The choice of app should be based on an individual's specific needs and preferences (61).
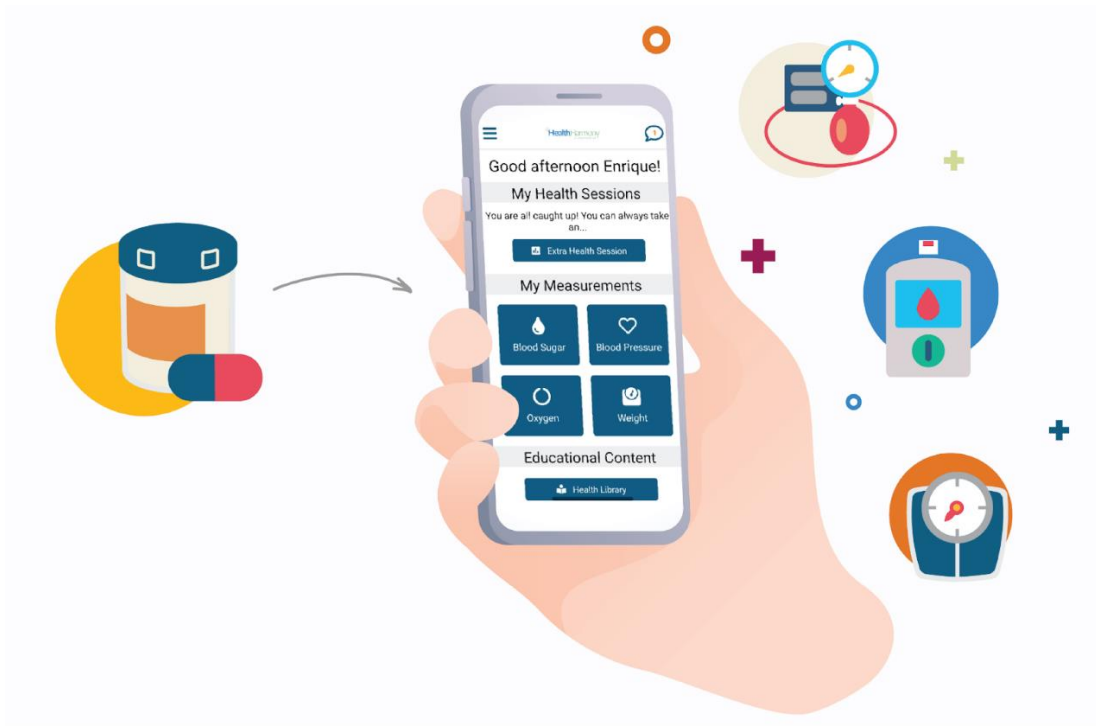
Figure 4 Mobile apps and digital platform of Parkinson's disease monitoring

Source: https://www.dusuniot.com/blog/parkinsons-disease-monitoring/

These tracking methods rely on self-reporting, which can be subjective and influenced by individual perceptions and memory. Patients may underreport or misinterpret the symptoms, leading to inaccuracies in data. Hence, there is a quest for new technology to assist in monitoring Parkinson's disease symptoms. Wearable technology has emerged to address the limitations of traditional methods for tracking these symptoms by offering continuous, objective, and comprehensive data.

2.4 Wearable Sensor Technology

Wearable sensor technology has been increasingly employed in the management and monitoring of PD (62). These innovative devices offer several benefits for both patients and healthcare professionals in tracking and improving the care of individuals with PD.

2.4.1 Gyroscopes (GYRO)

GYRO measure angular velocity and are often used in conjunction with accelerometers to provide a more comprehensive view of a patient's movements. These sensors play a help monitor and comprehend the motor symptoms and movement abnormalities associated with PD. By providing valuable data on alterations in posture, balance, and tremors, gyroscopes sensors ultimately enhance the diagnosis, treatment, and ongoing management of the condition. GYRO sensor has been featured to assist PD monitor. Nguyen A, *et al.* (7) developed a PD sensor using GYRO. In this work, the sensor was attached to the shoes, as shown in Figure 5, to monitor and analyze the walking patterns of PD classifying patients' severity levels based on their gait characteristics. GYRO-derived features have demonstrated a noteworthy correlation with the clinical assessment of dyskinesia severity in the work of Burkhard PR *et al.* (63). In this study, the participants were recorded for ten-second periods during the test. The data were evaluated to scale the severity of dyskinesia. Nonetheless, evaluating over extended time periods necessitates multiple recordings. Therefore, continuous long-term recording would present challenges because the recordings are confined to only ten-second as shown in Figure 6. Salarian A, *et al.* (64) employed a forearm sensor equipped with three gyroscopes for monitoring tremor in individuals with PD. The data of PD patients were recorded for periods of 3-5 hours, as shown in Figure 7a and b, with the 3-D gyroscopic sensor. The gyroscope data indicates the presence and amplitude of the tremor. GYRO sensors hold potential as valuable tools for assessing motor symptoms in PD. However, their application is constrained by their highly power consumption rate, which could ultimately hinder their capacity for extended monitoring.
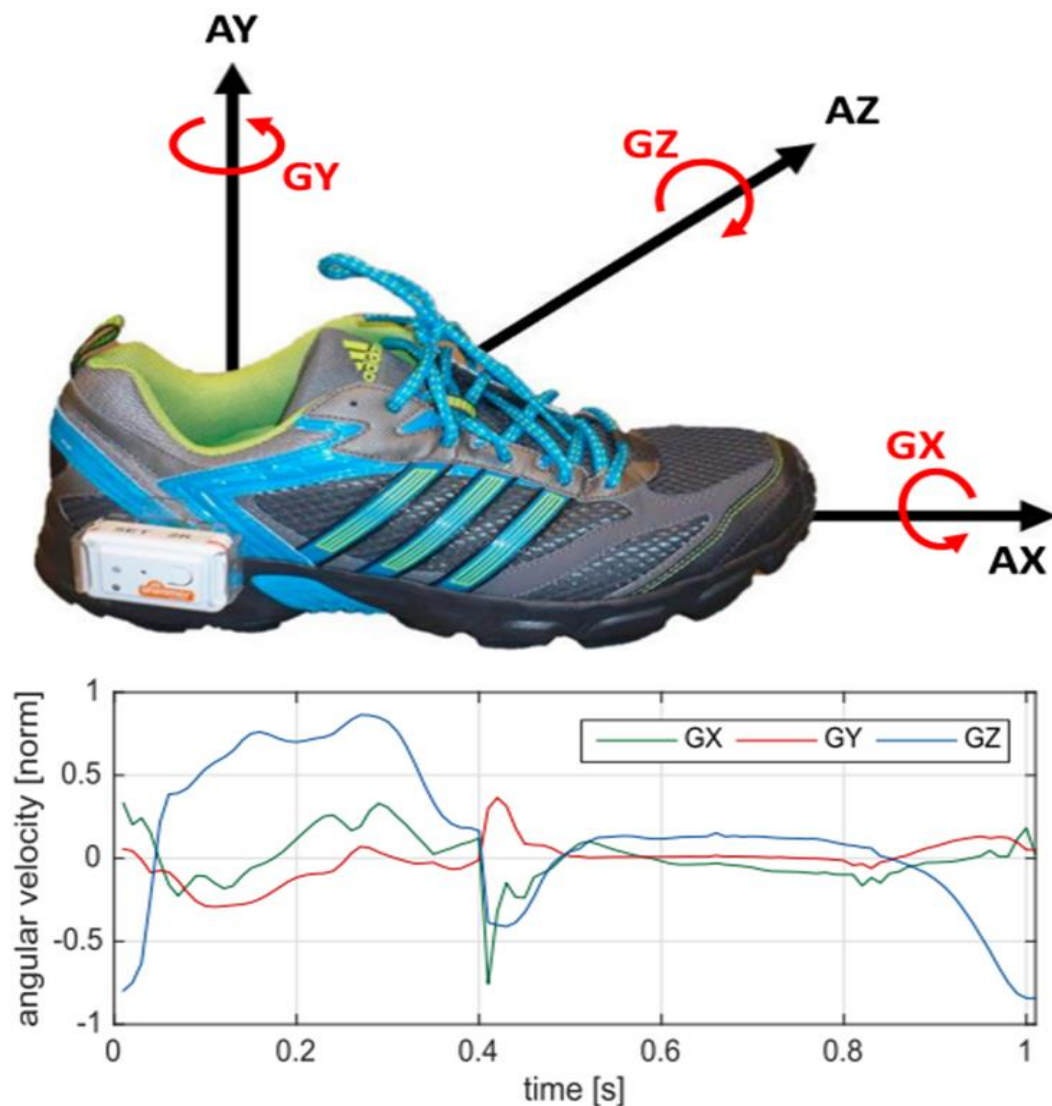
Figure 5 Sensor placement on the lateral side of each shoe and gyroscope data

Source: Nguyen. (2019) J Neuroeng Rehabil 16:77
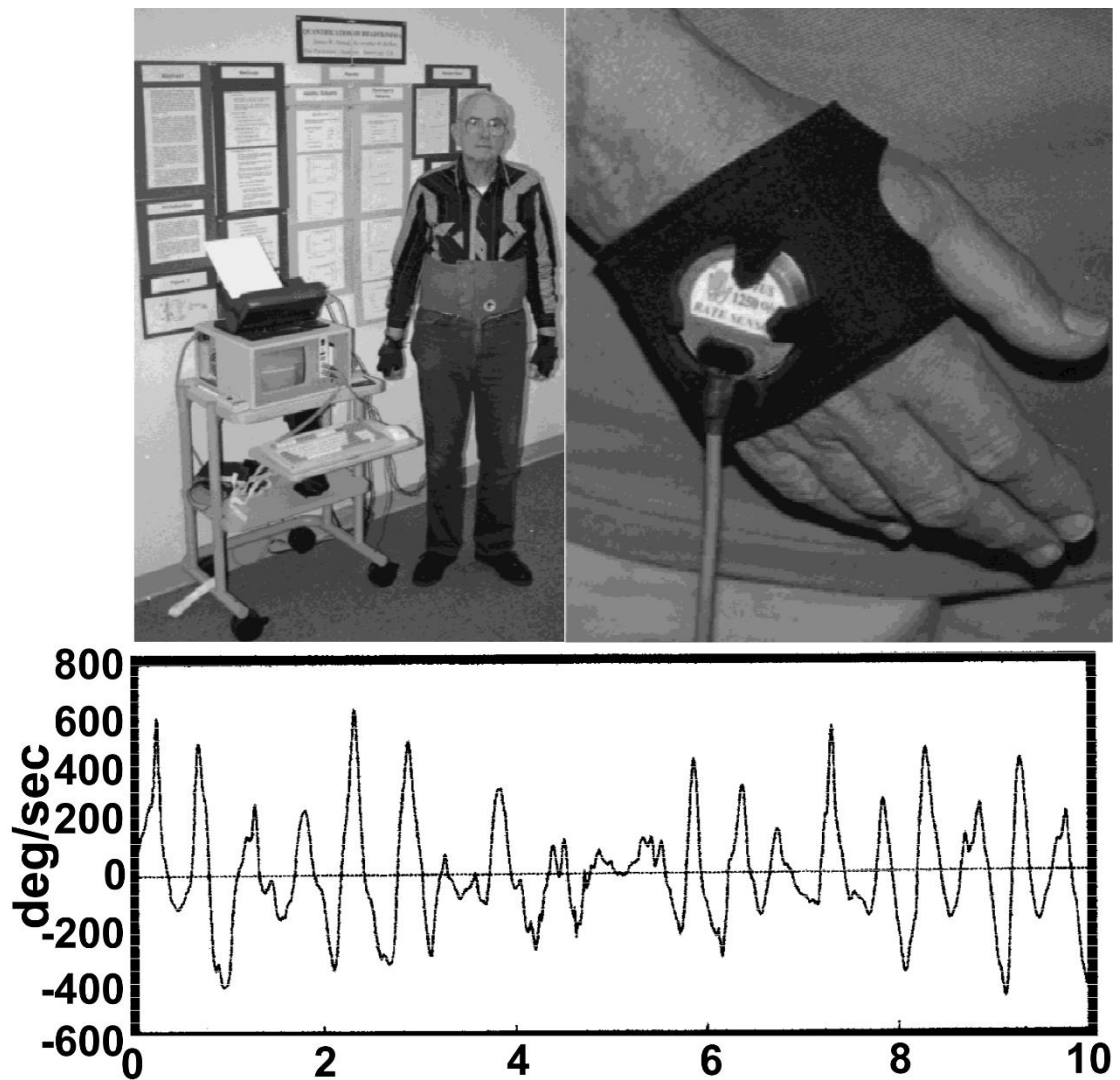
Figure 6 The dyskinesia recording session and gyroscope data

Source: Burkhard PR (1999) Movement Disorders p. 754-63
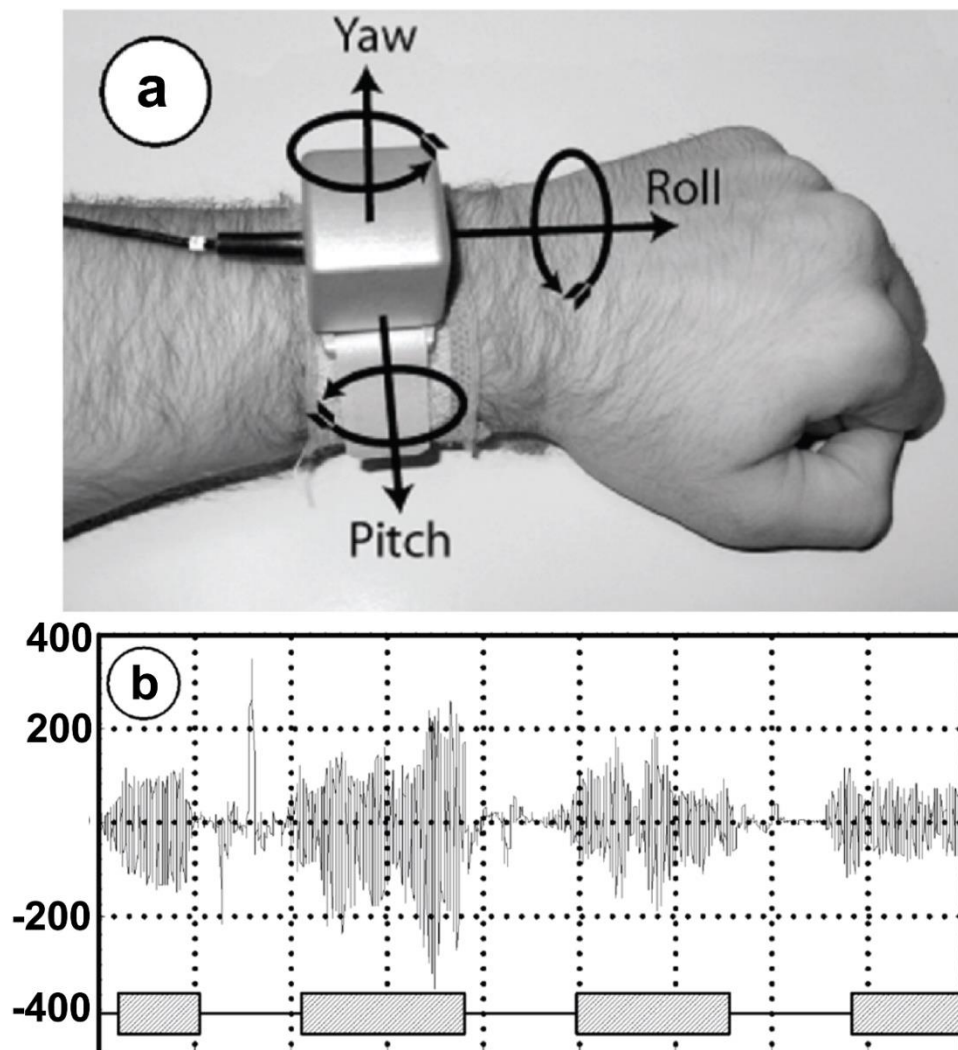
Figure 7 a) the 3D gyroscopic sensor and b) gyroscope data present of tremor and the amplitude the tremor

Source: Salarian (2007) IEEE Trans Biomed Eng. p. 313-22.

2.4.2 Accelerometers (ACC)

ACC are commonly integrated into wearable devices like smartwatches or fitness trackers. They measure acceleration and movement in various directions, making them useful for detecting changes in gait, balance, and tremors. In the work of Aich S, *et al.* (65), freezing of gait (FoG) was studied using an ACC. The sensor successfully detected the gait parameter associated with the progression of FoG, as shown in Figure

8a. However, as seen in Figure 8b, the wearable device was connected via wires to the accelerometer, potentially further limiting movement and introducing the possibility of interference with the movements being measured.
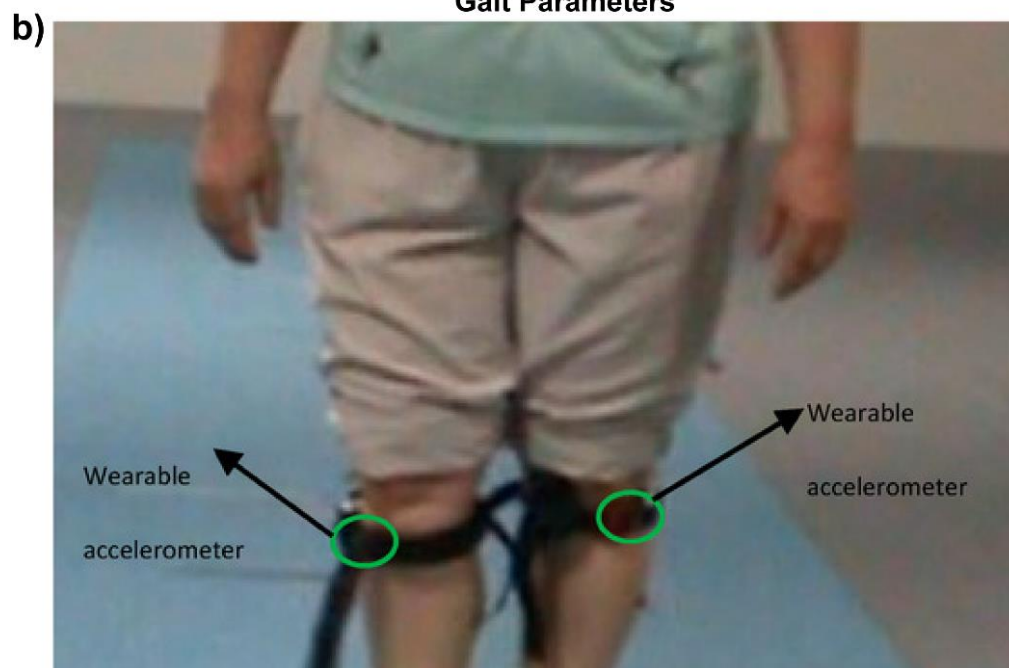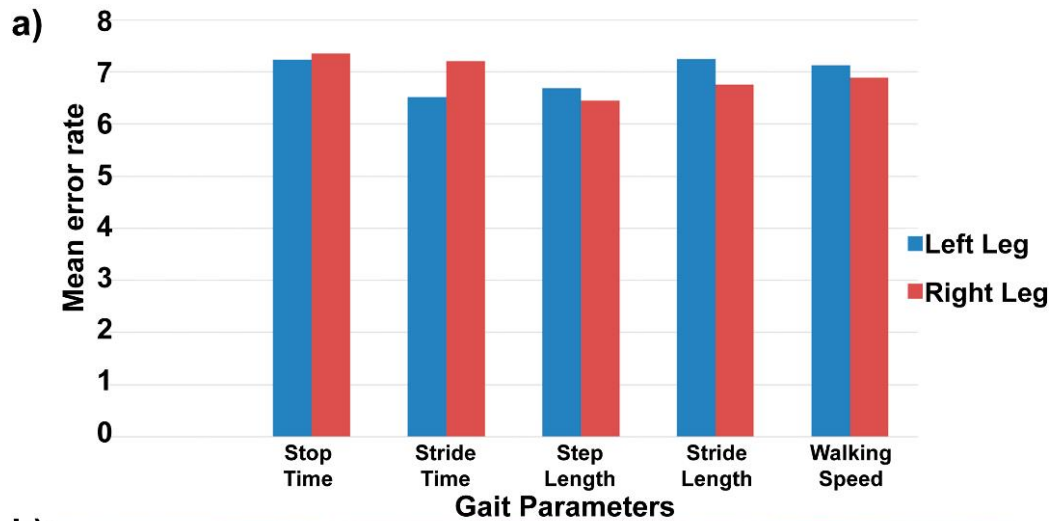
Figure 8 a) Gait parameters for left and right legs obtained from wearable accelerometer-based, b) The wearable accelerometer

Source: Aich S (2018) Sensors p.3287

2.4.3 Electromyography (EMG) Sensors

EMG sensors detect electrical activity in muscles. They can be used to monitor muscle tremors and rigidity, which are common motor symptoms of PD. Vescio B, *et al.* (66), studied the use of EMG as PD sensor to analysis and diagnosis of tremors. Figure 9a shows the characteristics of tremor patterns of PD patient, which have been proven to be useful for monitoring. However, as shown in Figure 9b, the EMG typically involves wires. Moreover, EMG necessitates the placement of electrodes on the skin overlying the muscles of interest, which is an invasive procedure (67).
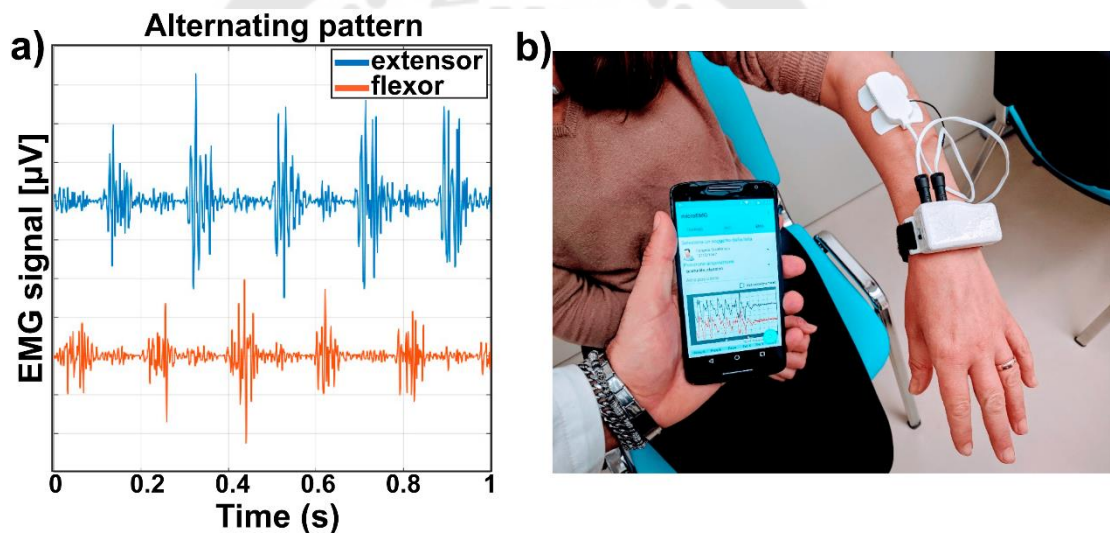
Figure 9 a) Spectral characteristics of tremor patterns, b) EMG device

Source: Vescio B (2021) Frontiers in Neurology p.12

The use of the above sensors in monitoring and managing PD symptoms is a promising avenue of research and development. However, ongoing research and development are needed to address some challenges such as continuous long-term recording is constrained by power consumption, interference, and invasiveness. Therefore, it is essential to explore new technologies as potential alternatives to these sensors.

2.5 Triboelectric Nanogenerator (TENG)

Triboelectric Nanogenerator (TENG) is a device that generates electrical energy through the triboelectric effect, which is the generation of an electric charge when two dissimilar materials come into contact and then separate. There is a transfer of electrons between materials. This electron transfer leads to the creation of an electric potential difference. This effect is responsible for the familiar phenomenon of static electricity. TENGs are designed to harness this effect and convert mechanical energy into electrical energy. The concept and development of TENG can be attributed to the pioneering work of Professor Zhong Lin Wang and co-workers in 2012. Initial research focused on basic TENG prototypes and demonstrating their potential for energy harvesting from a variety of mechanical motions, such as tapping, sliding, and even walking. Over the years, the TENG technology evolved with the development of new materials, improved device designs, and increased energy conversion efficiency. This progress made TENGs more practical for real-world applications.

2.5.1 Working Principle and Mechanism of Triboelectric Nanogenerator (TENG)

The TENG typically consists of two components, one that serves as an electron donor and another as an electron acceptor. These components are separated by a small gap. When an external force is applied to bring the materials into contact and then separate them, the triboelectric effect occurs, generating an electric charge. This charge can be collected and used to power electronic devices. The mechanism of TENG is shown in Figure 10. At stage (i), the two materials are separated from each other because no external force is applied. Therefore, no electrical output is generated. At stage (ii), the two materials are physically brought into contact. As the two materials make contact, the triboelectric effect takes place. This is where electrons are transferred from one material to the other due to differences in their electronegativity. The material with higher electronegativity attracts electrons from the material with lower electronegativity. The electron donor loses electrons and becomes positively charged, while the electron acceptor gains electrons and becomes negatively charged. When the two materials start to separate at stage (iii), the two surfaces are separated from each

other. Positive charges on the surface of an electron donor material induce negative charges on the electrode, while negative charges on the surface of an electron acceptor material induce positive charges on the electrode. Resulting in an electric potential difference between the electrodes, this drives free electrons to begin flowing through an external load until equilibrium is reached, completing the separation in stage (iv). When the materials begin to close again (stage v), the cycle described above is repeated, generating a reverse current in the external load. The alternative current is obtained.
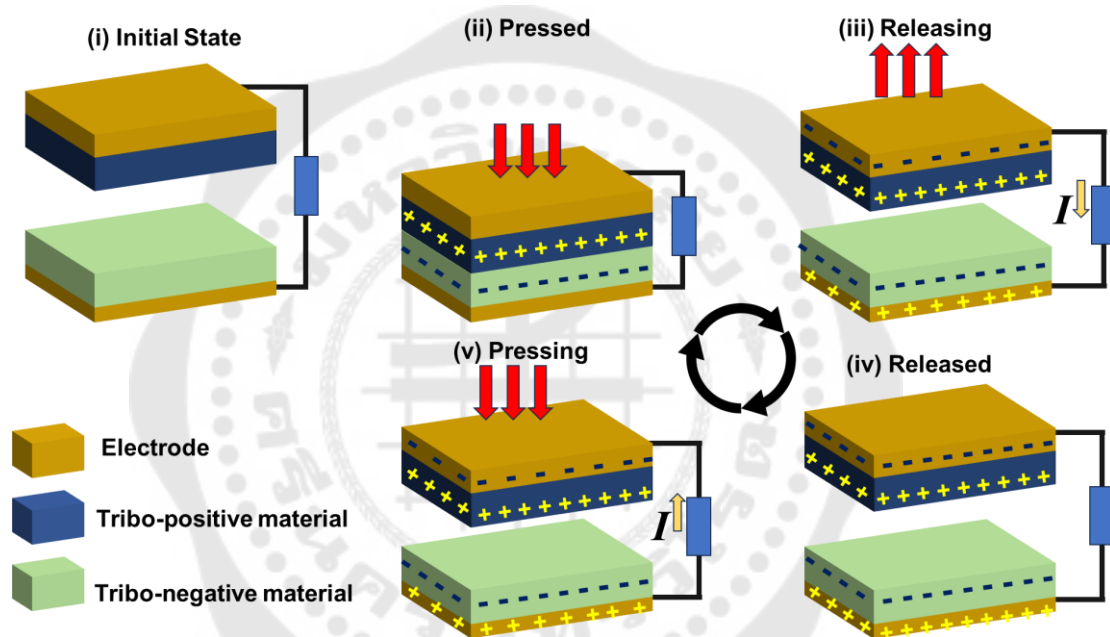
Figure 10 Mechanism diagram of TENG

2.5.2 Operating Modes of Triboelectric Nanogenerator (TENG)

TENG can operate in various modes, each suited to different types of mechanical motions and applications. The key operating modes of TENG are detailed as follows.

2.5.2.1 Vertical Contact-separation (VSC) Mode

VSC is the simplest design of TENG as schematically described Figure 11a. In this mode, two dissimilar materials have electrodes deposited on both the upper and lower surfaces, which are interconnected to an external load. When these two

materials physically come into contact with each other in a vertical direction, the two dielectric films create oppositely charged surfaces. As an external force lifts and separates the two surfaces by a small gap, a potential difference is generated. This could drive free electrons from one electrode could move to the other electrode, creating an opposing potential to balance the electrostatic field. When the gap is closed again, the free electron flows in the opposite direction (68, 69).

2.5.2.2 Lateral Sliding (LS) Mode

LS mode is schematically described in Figure 11b, where the two materials slide laterally against each other. The electric charge generation is due to the relative motion between them. The construction is almost similar to the VSC, but the displacement has occurred sideward. When the friction layers start to slide, triboelectric charges form on their inner surfaces, inducing opposite charges on the electrodes. Subsequently, the charge would flow to the external load. An AC output is generated by periodic sliding apart and closing. The LS modes can be modified to accommodate relative sliding in planar, rotational, and cylindrical configurations (36, 69).

2.5.2.3 Single Electrode (SE) Mode

The two kinds of modes mentioned above contain two friction layers and two electrodes interconnected by an external load. SE mode is a mode where only one material is employed, and a conductive electrode is positioned nearby to collect the charge generated during contact and separation as shown in Figure11c. Such a design has a single friction layer with a back electrode connected to the ground. The external object, whether contacting or sliding on the TENG, will act as a supplementing friction layer. External mechanical force, in the form of contact-separation or relative sliding, result in the generation of alternating current between the electrode and the ground (69). The SE mode of TENG is often used in applications where simplicity and compactness are essential.

2.5.2.4 Free-standing (FS) Mode

FS mode is illustrated in Figure 11d. In this mode, a freestanding triboelectric layer is capable of deforming or vibrating. The motion of this layer generates

charge separation. The FS mode structure comprises a connected pair of electrodes. The electrode size should be the same as that of the free-standing layer, so it can only cover one of the electrodes. When the free-standing layer makes contact with one of the electrodes, a current flow between these two electrodes due to varying electrostatic field (69). Freestanding TENGs are commonly used in flexible and wearable devices that need to adapt to various body movements.

The choice of operating mode depends on the specific application and the type of mechanical motion available. TENG technology's versatility and ability to capture energy from various sources make it a promising technology for self-powered and energy-efficient devices in a wide range of fields, including health monitoring.
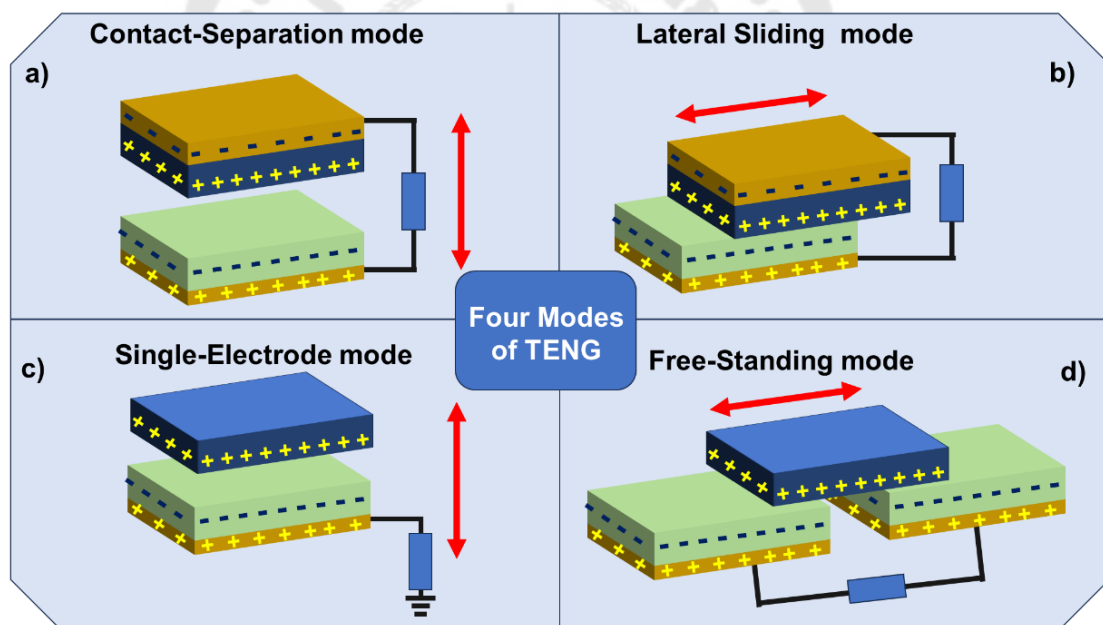
Figure 11 Four modes of TENG

2.5.3 Materials for Triboelectric Nanogenerator (TENG)

TENG use materials with different triboelectric properties to generate electricity through the contact and separation of these materials. The selection of materials depends on the specific application and design of the TENG, but commonly used

materials include Polymer, which are often used as the base materials for TENG. Metals, which are used as electrode or dispersed phase. Fabrics, certain types of fabrics can be used as triboelectric materials, especially when designing wearable TENG. Organic Materials, some organic materials with specific triboelectric properties can be used, such as graphene and conducting polymers. One of the key factors in selecting materials for a TENG is to base the choice on the triboelectric series, involving the selection of materials that are significantly far apart on the series. This maximizes the charge separation and enhances the TENG's efficiency.

2.5.3.1 Triboelectric Series

The triboelectric series is a ranking of materials arranged according to their ability to gain or lose electrons when in contact with each other, as shown in Figure 12. A material's placement within the triboelectric series indicates whether it has a tendency to become positively charged (losing electrons) or negatively charged (gaining electrons) when it is rubbed against a material positioned lower on the list. When two materials on the triboelectric series come into contact and then separate, the one higher on the list will become positively charged, while the one lower on the list will become negatively charged. However, the selection of materials depends on the specific application, the desired triboelectric properties, and the type of mechanical motion the TENG will be subjected to. This will improve TENG efficiency and versatility for a wide range of applications.
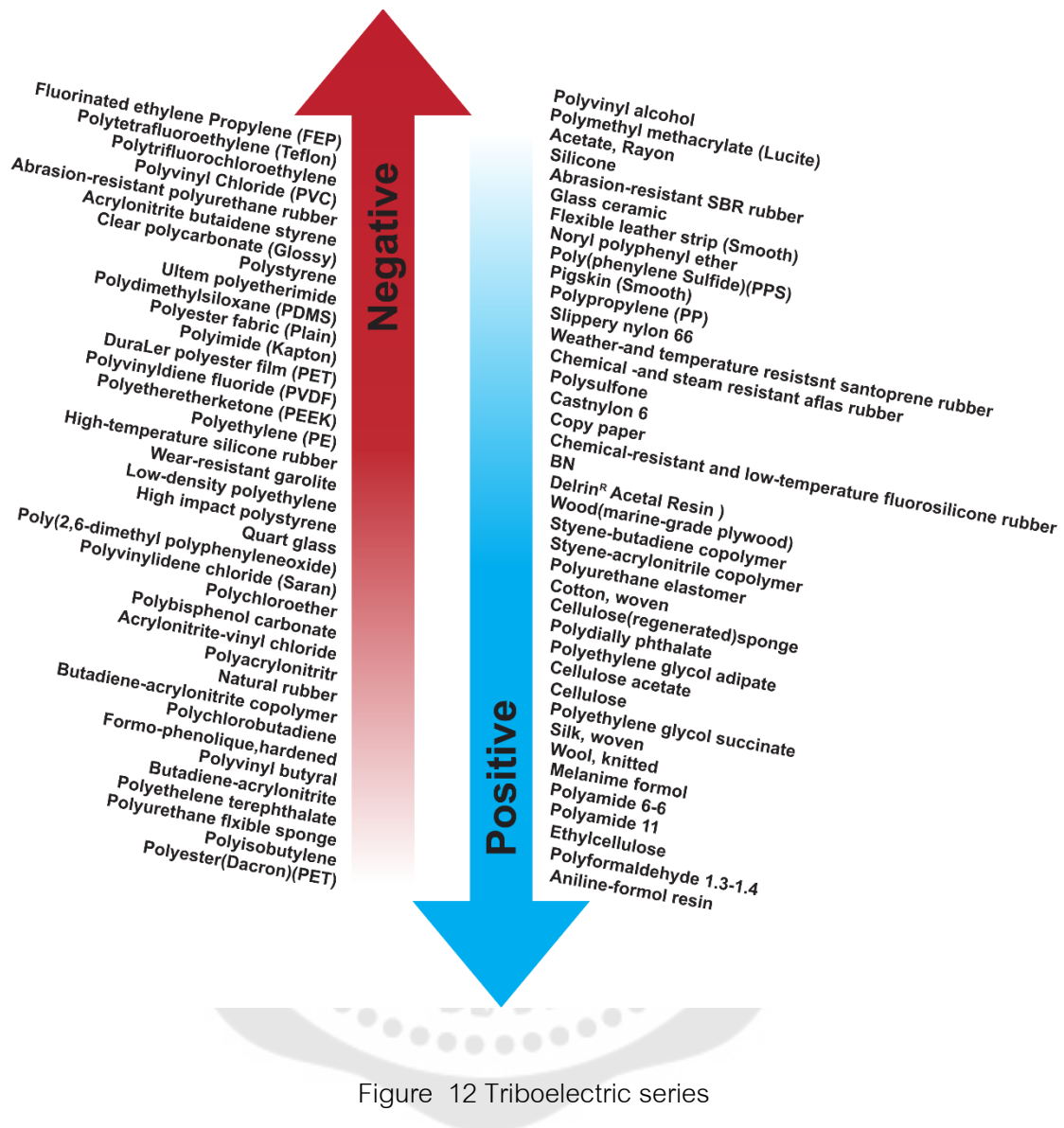
Figure 12 Triboelectric series

Source: Liu Y. (2021) Adv. Funct. Mater p.2004714

2.5.4 Triboelectric Sensor (TES)

Due to TES's ability to convert mechanical energy into electrical energy, it has been applied in self-powered mechanical sensing across various fields such as human-machine interaction (HMI) (70), gas sensor (71), self-powered smart agriculture senser (72), humidity sensor (73). Also, TENG can be designed into wearable devices as a health monitoring sensor, such as to monitor PD symptoms. Li R *et al.*(28) designed a

personal healthcare sensor composed of PTFE and Fe, which can be worn as a foot or hand ring see as shown in Figure 13a. The sensor converts mechanical energy from body motion into electrical signals. The output signal amplitude corresponds to different body movements as shown in Figure 13b and c. The device in this work has a closed cylindrical structure with a Fe ball moving inside. The Fe ball can move both in a circumferential direction and up and down, potentially leading to interference between the output signals.
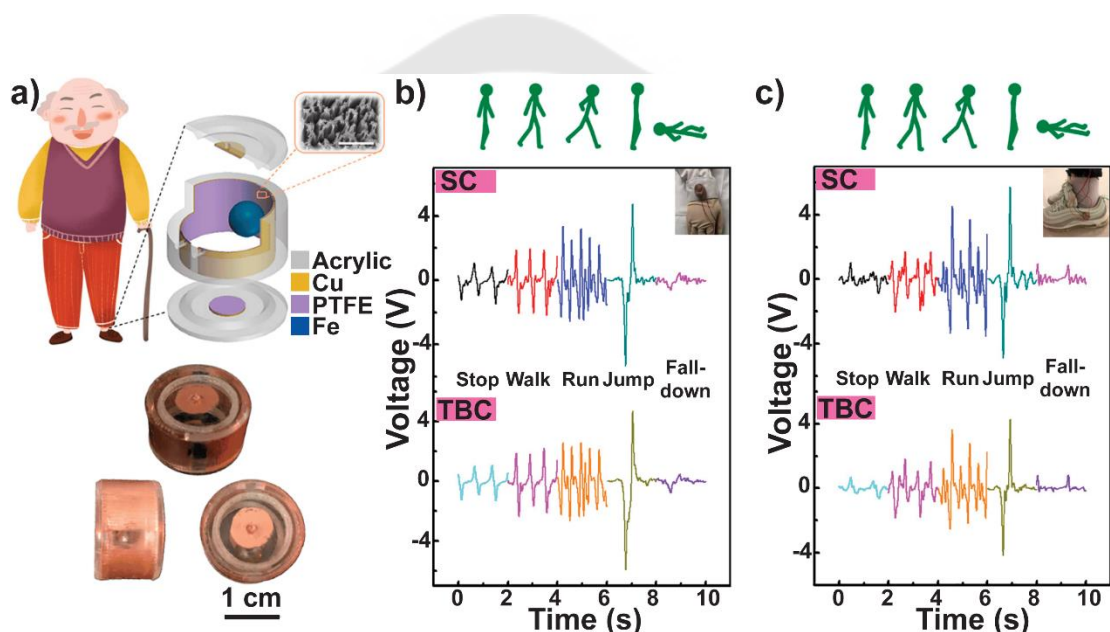
Figure 13 a) Sensor schematic and digital image, Motion state monitoring signals (Step, Walk, Run, Jump, Fall-down) of the sensor in different wearing parts b) wrist and c) shoe.

Source: Li R (2021) Micromachines p.352

Vera Anaya D, *et al.* developed a PD sensor constructed from Ecoflex with aluminum (Al) electrode. The structure and mechanism of the device is illustrated in Figure 14a, b. This device is employed to monitor forearm muscle and tendon movements for the purpose of detecting and tracking the symptoms and progression of PD. The voltage signal produced by the proposed sensor exhibits distinct waveform shapes, time durations, and amplitudes corresponding to the progression of the disease

as shown in Figure 14c (29). The design of the device made it bulky and the sensor placement can be uncomfortable, which can restrict the patient's movements.
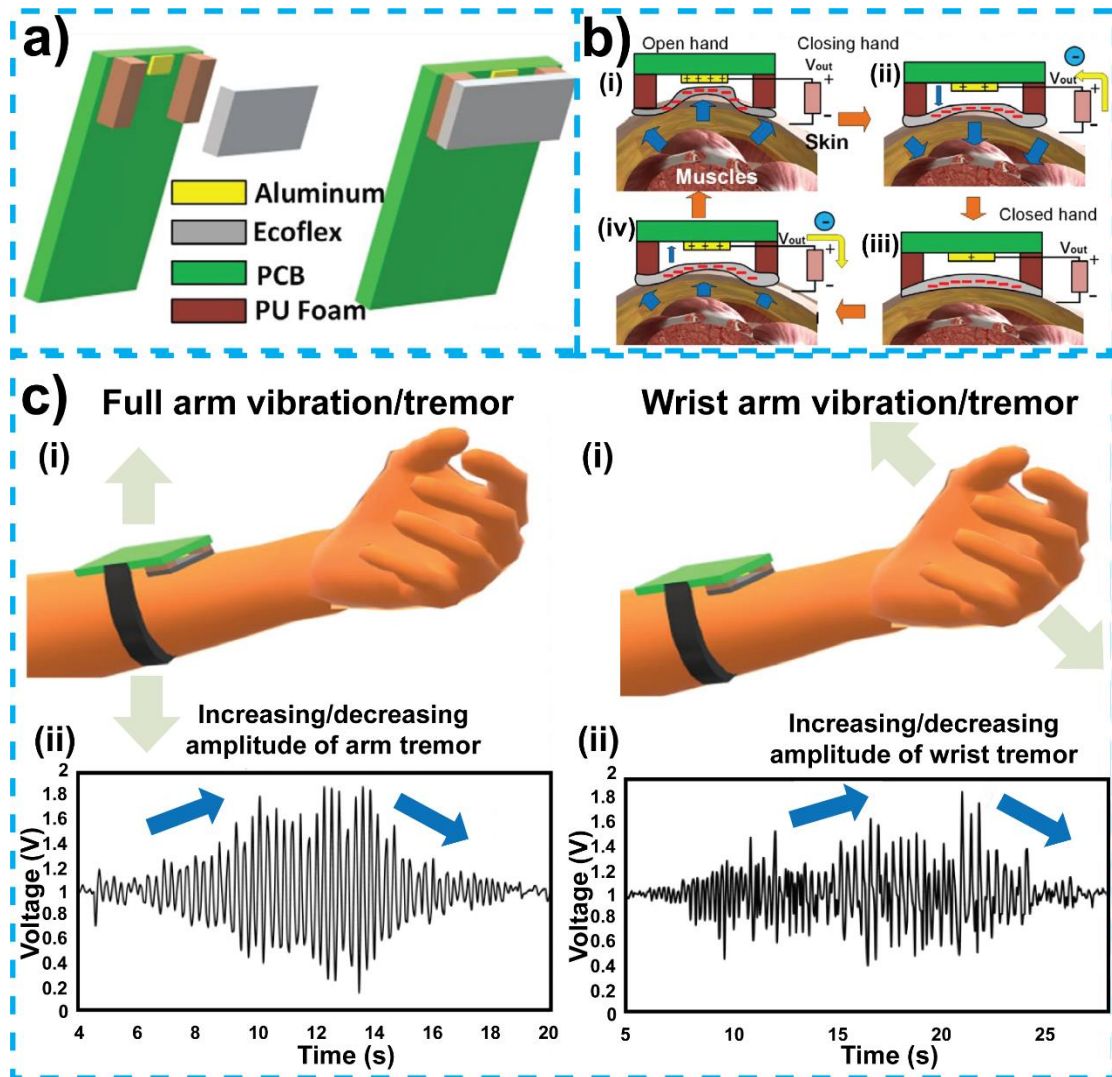
Figure 14 a) structure and b) mechanism of the forearm triboelectric sensor. c) Output due to the emulation of arm tremor. d) Output due to the emulation of wrist tremor.

Source: Vera Anaya And Yuce (2021) Medical Devices & Sensors p.10154.

Another group of research, Kim J-N, *et al.* developed self-powered tremor sensor for monitoring and assisting individuals with PD. The study introduces a highly stretchable and self-healing hydrogel conductor, made from biomaterials, including

catechol, chitosan, and diatom referred to as the catechol-chitosan-diatom hydrogel (CCDHG) as shown in Figure 15a. The self-powered tremor sensor, which includes an M-shaped Kapton film and the CCDHG-TENG, is specially designed to monitor the health conditions of PD patients (Figure 15b). The sensor collects data on the electrical charge generated by the triboelectric effect in response to tremors. These electrical signals are proportional to the amplitude and frequency of the tremors as illustrated in Figure 15c. However, the fabrication of the catechol-chitosan-diatom hydrogel can be complex and challenging due to the involvement of several steps (30).
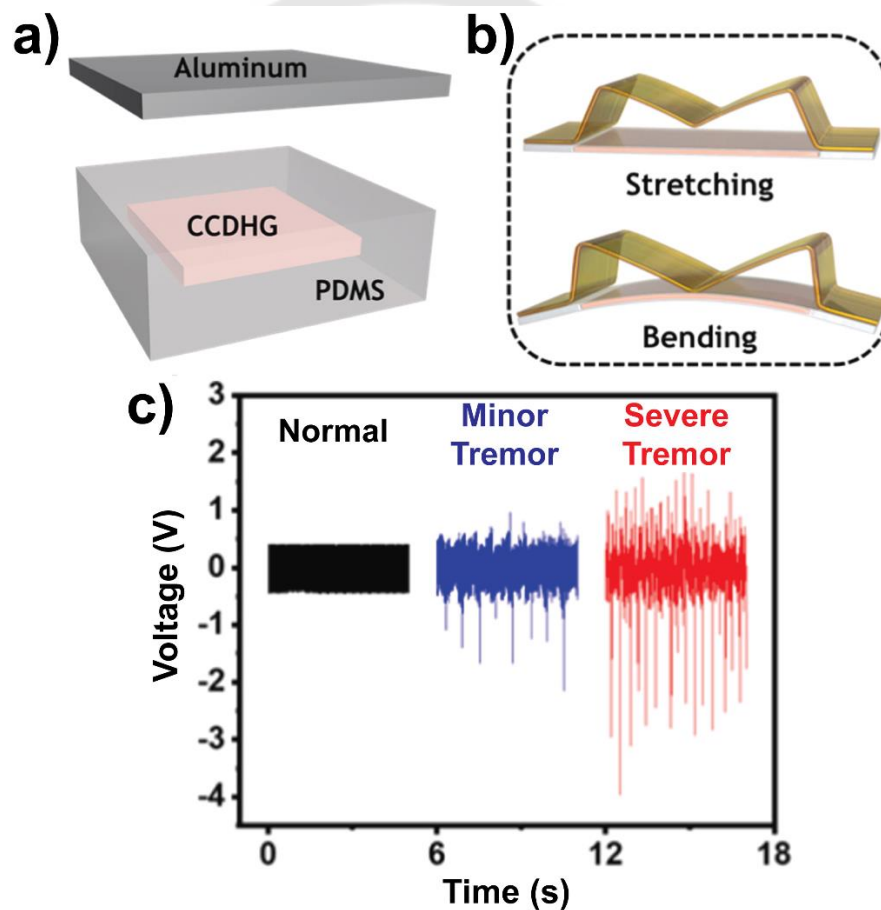
Figure 15 a) Structure of CCDHG-TENG, b) Schematic image of tremor sensor while stretching and bending and c) Voltage signals of tremor sensor with three motions.

Source: J.-N. Kim (2021) Nano Energy p.105705.

In the previously mentioned literature, it is observed that the output has low signal-to-noise ratio. This poses a challenge in distinguishing the small signal amplitude from ambient noise, leading to inaccuracies and instability. The current design of the device remains cumbersome and impractical for everyday use, posing potential constraints on the patient's mobility and lifestyle. Hence, it is imperative to undergo further design and development to create a structure that is lightweight, functional, and convenient. This development should also incorporate clear electrical signals that effectively indicate symptoms of PD.

There are some parameters that can be considered for designing effective TES, capable of measuring the amplitude, frequency, and severity of tremors, and providing valuable data to healthcare professionals for diagnosis and treatment monitoring.

2.6 Parameters for triboelectric sensor (TES) design

2.6.1 Material Selection

Numerous factors influence TENG performance, with material selection playing a pivotal role. This is because the physical and chemical properties of triboelectric materials can significantly impact TENG performance. A variety of materials, including polymers, metals, and inorganic substances, are utilized as triboelectric layers. Notably, frequently used dielectric polymers like PTFE, FEP, PDMS, and Kapton are mentioned (33). Ramaswamy SH, et al., investigated the potential use of diamond-like carbon (DLC) films as dielectric materials for TENG and compared the characteristics of DLC films with conventional dielectric materials such as PTFE and Kapton. The results indicate that TENG utilizing hydrogenated DLC (H-DLC) in combination with PTFE as a triboelectric pair produced the highest output, with a peak voltage of 38 V, current of 3.5 μA and a power density of up to 57 mW/m^2. This performance outperformed other conventional dielectric pairs as shown in Figure 16 (74).
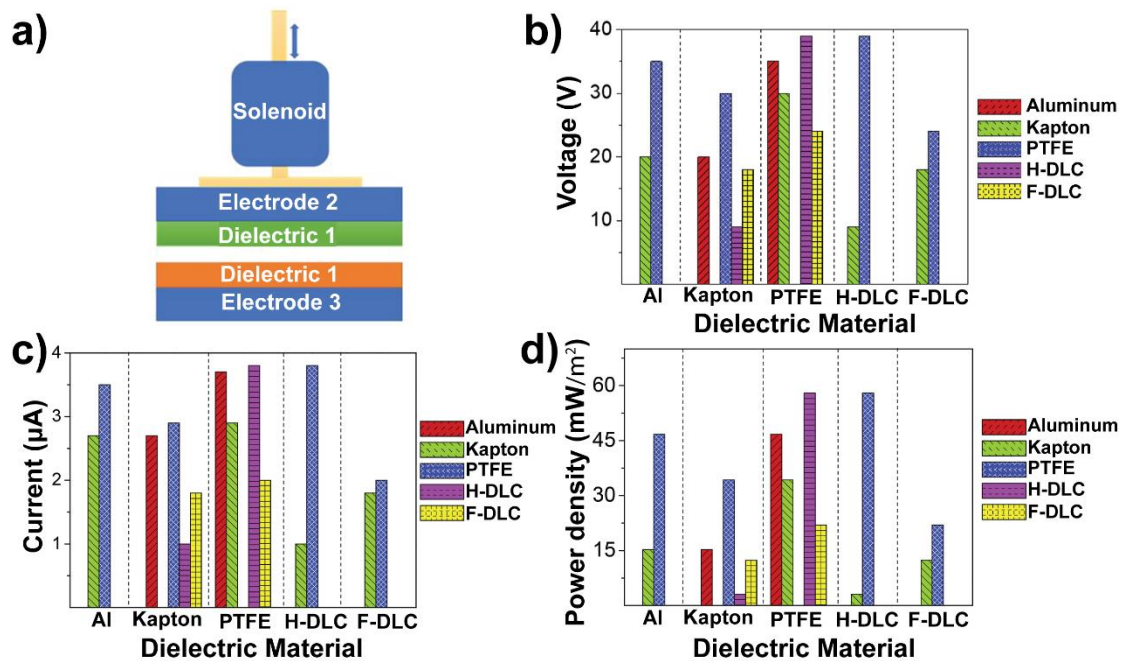
Figure 16 a) Schematic representation of TENG. B) Summary graph of b) V_{OC}, c) I_{SC} and d) power density displaying each of the dielectric material pairs

Source: S.H. Ramaswamy (2019) Nano Energy p.875-885.

Wang H, *et al.* explored the concept of programmed-triboelectric nanogenerators, which represent devices specifically engineered for effective energy manipulation, highlighting the pivotal roles of material choice in their functionality. In this study, two materials, namely FEP and PTFE film, were chosen as dielectric coatings. As depicted in Figure 17a, the study involved testing both FEP vs. FEP and FEP vs. PTFE configurations. The results show that FEP vs. PTFE has higher electrical output of voltage and power around 1300 V, 3 mW (Figure 17b-c). The performance of charging a 0.1 µF capacitor is shown in Figure 17d, the FEP vs PTFE can charge it to 18 V. (75)
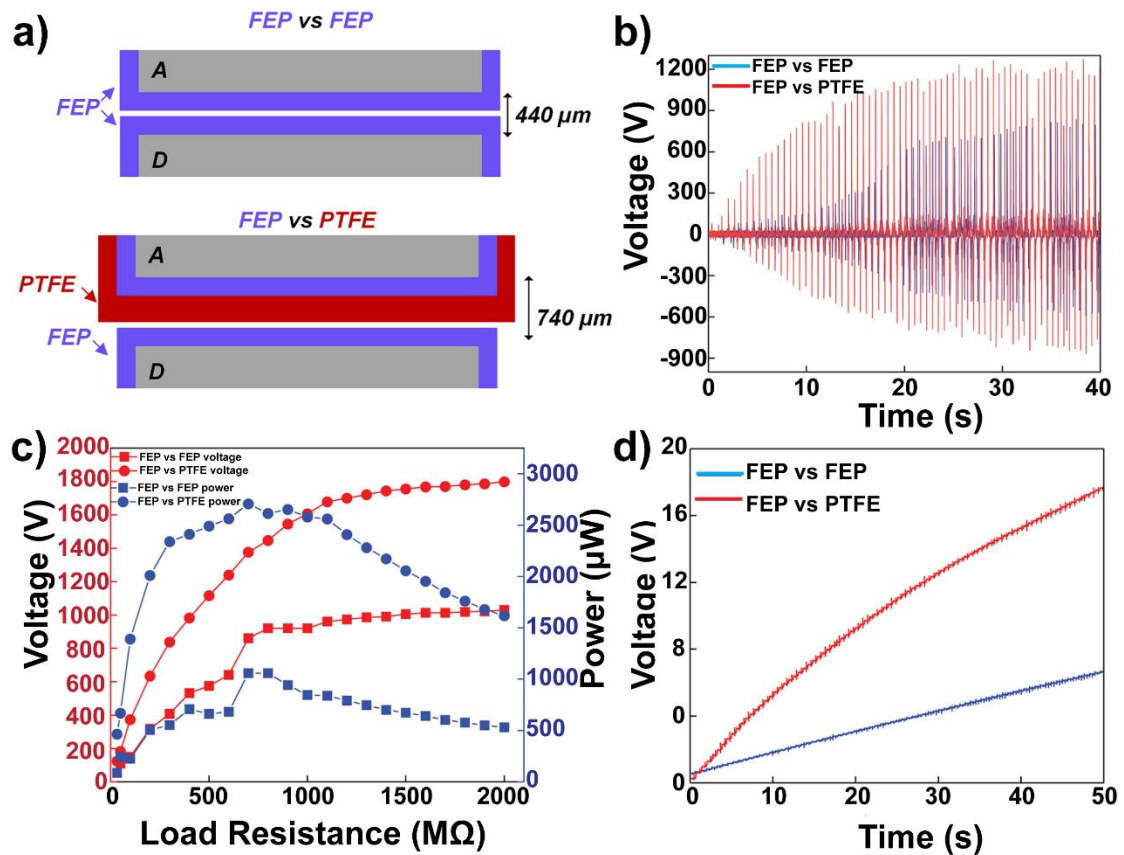
Figure 17 a) the two dielectric layer groups in tests, b) The output voltage, c) the voltage and peak power by changing load resistance and d) The performance of charging a 0.1 µF of the two groups

Source: H. Wang (2020) Nano Energy p.105241.

The selection of materials for TES is crucial as it directly impacts the device's performance and efficiency. TES relies on the triboelectric effect, which generates electricity through the friction and separation of materials with different electrostatic properties. However, it is important to note that material selection for TES can vary significantly depending on the application. Therefore, it is essential to thoroughly assess the specific requirements and constraints of the application when choosing the appropriate materials to enhance TES performance.

2.6.2 Material Surface Modification

The pursuit of high signal-to-noise ratio for TES is indeed a significant challenge, especially when operating in atmospheric conditions. While TENG have shown the ability to efficiently convert low-frequency mechanical energy into electricity, achieving high output performance directly in the atmosphere is a complex task. Surface engineering plays a crucial role in overcoming these challenges (34). Ibrahim M, *et al.* develop a multiscale micro- and nano-structured magneto-mechano-triboelectric nanogenerator (MMTENG) using salt particle imprinting process (Figure 18a and 18b). The aim was to use this MMTENG to power an Internet of Things (IoT) sensor. The salt-imprinted MMTENG can generate the V_{OC}, the I_{SC} and peak power of up to 851 V, 155 µA and 10.3 mW, respectively (Figure 18c-f). The electricity generated by the surface-enhanced MMTENG can be used to power an IoT temperature sensor, showcasing the feasibility of using this energy harvesting technology in real-world IoT applications (76).
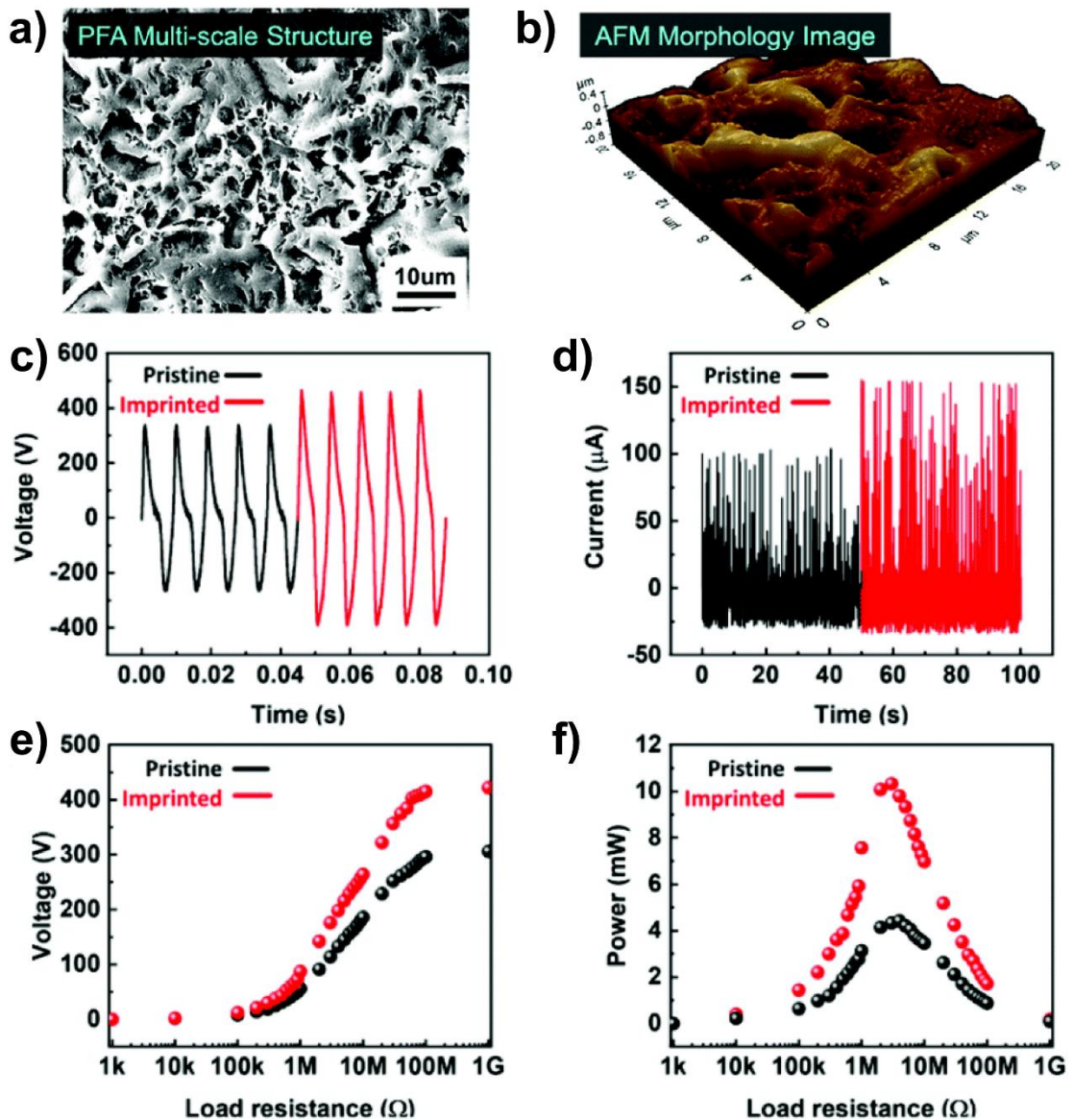
Figure 18 a) SEM image of the surface of PFA film after surface modification, b) 3D AFM image of the surface of salt-imprinted PFA film. c) V_{OC}, d) I_{SC}, e) The measured absolute peak voltages under different external load resistances and f) The peak power values

Source: Kwak MS (2021) Nanoscale p.8418–8424

Zhu G, et al. created flexible triboelectric sensors that generate electrical energy from tactile interactions. The sensors are based on the principle triboelectric

effect. Surface modifications play a crucial role in the sensor's ability to generate voltage signals in response to physical contact. Therefore, in this study, the authors created vertically aligned polymer nanowires on the FEP surface using plasma dry etching as illustrated in Figure19a-19c. As depicted in Figure 19d, when subjected to a contact force, the triboelectric sensor (TES) generates a consistent square-wave output voltage with a peak amplitude of 35 V. The ultrasensitive tactile sensing without an external power source was successfully developed (77).
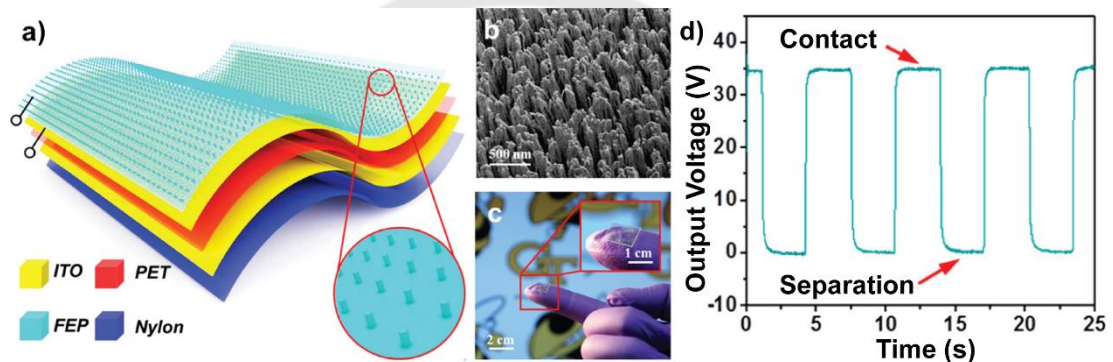
Figure 19 a) Structure of TES, b) SEM image of polymer nanowires g, c) Photograph of an as-fabricated TES and d) Output voltage of TES.

Source: Zhu G (2014) Nano Letters p.3208-13.

Surface modification plays an important role in the design of TES, which will help improve the ability of TES to generate triboelectric phenomena. Customizing surface modifications for specific applications enables TES to serve as self-powered sensors.

2.6.3 Triboelectric Nanogenerator Mode Selection

TENG has a wide range of applications, including self-powered sensors, wearable electronics, and more. The mode selection is a crucial aspect of optimizing the TES's performance for a given application. Xu Z, et al. explored the output performance of both the vertical contact separation mode TENG (CS-TENG) and the lateral sliding

mode TENG (LS-TENG). Subsequently, the author sought to combine these two modes to develop a hybrid TENG aimed at enhancing the output power. The friction layers were made of PTFE and PVA. The finding shows that operation mode of TENG effect the electrical output. As shown in Figure 20a-e, the voltage output curve of CS-TENG mode is about 131.63 V while LS-TENG mode is about 25.76 V. Therefore, the CS-TENG mode was chosen to design self-powered sensors for body motion detection, offering potential in healthcare for post-rehabilitation training and enhancing patient mobility and recovery. (78).
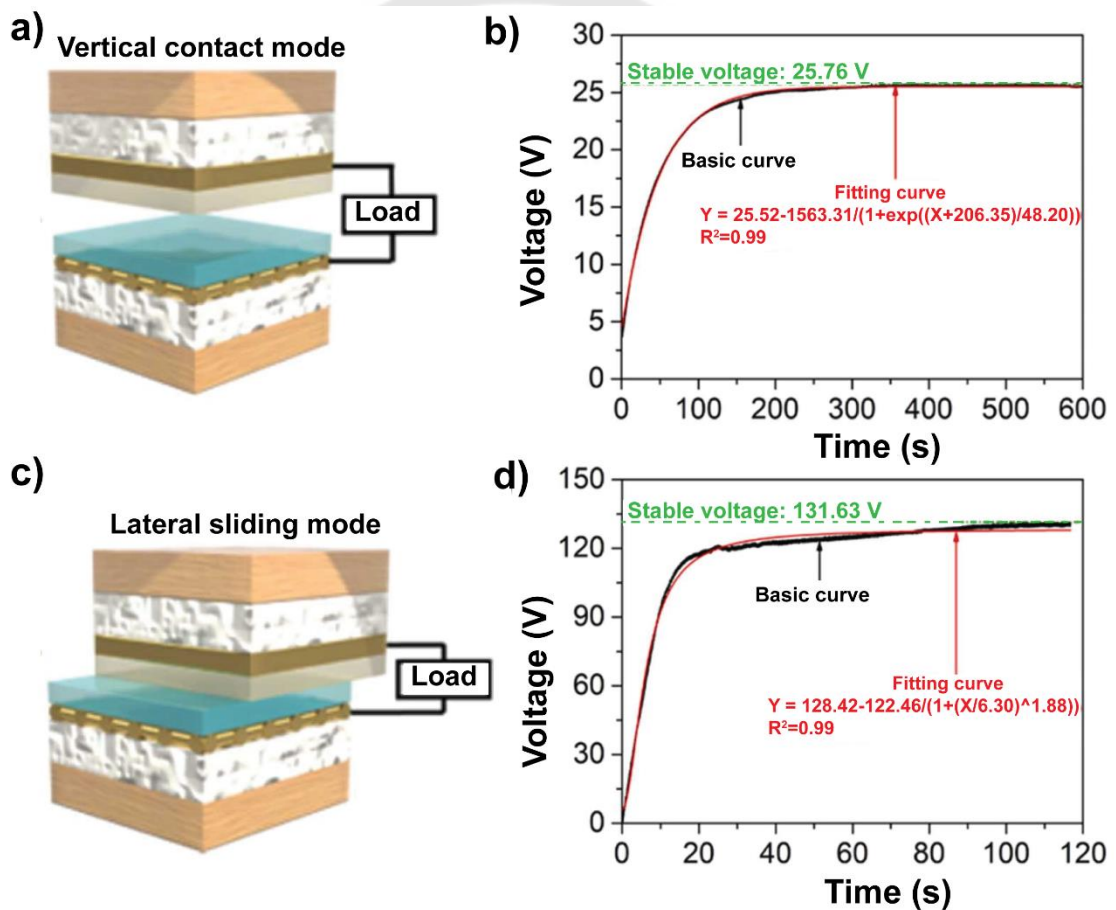
Figure 20 a) the structure diagram and b) electrical output of contact-separation mode. c) the structure diagram and e) electrical output of lateral sliding mode.

Source: Z. Xu (2022) Nano Energy p.107719.

In Zhang Z, et al. study, the single-electrode (SE) mode and the freestanding-triboelectric-layer (FTL) mode were determined (79). SE mode and FTL mode are two of the fundamental operating modes of triboelectric nanogenerators. Materials used as triboelectric pairs in this work were Kapton and Cu. The authors first evaluated the outputs of FTL mode, the I_{SC} was detected with a peak value of 60 µA and the V_{OC} was peaked at 110 V as shown in Figure 21a-21c. For SE mode, the I_{SC} and V_{OC} 4 µA was 12 V were obtained as demonstrated in Figure 21d-21f.
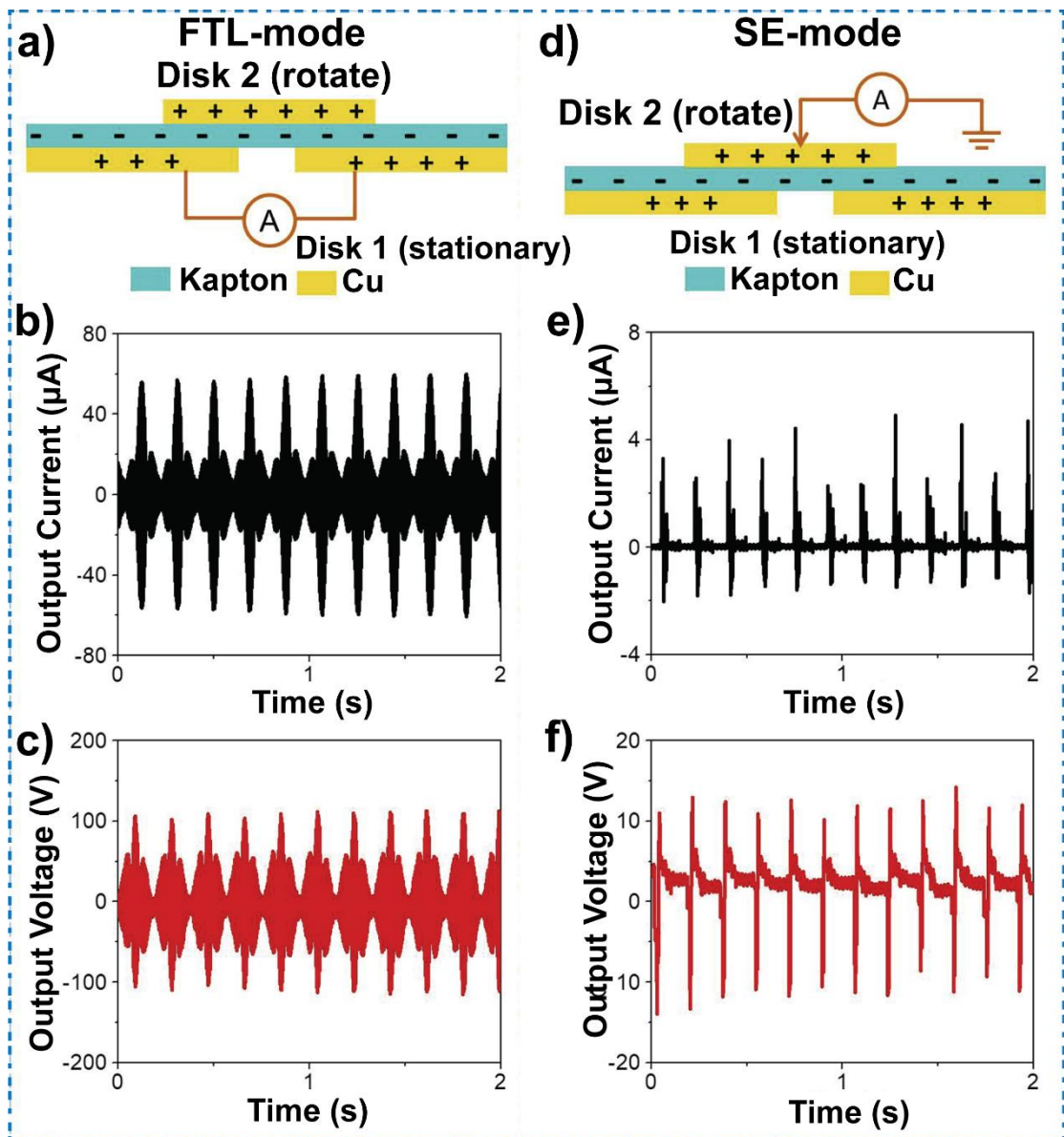
Figure 21 a) Free-standing layer (FTL) mode, b-c) Output current and output voltage of FTL mode. d) Single electrode (SE) mode, e-f) Output current and output voltage of SE mode.

Source: Z. Zhang (2019) Nano Energy p.104169

It should be noted that TES mode selection depends on the specific application, available motion types, and efficiency requirements. Researchers often design TESs to align with the mechanical energy source and the target device or system's requirements.

2.6.4 Structure Modification

Structure modification of TES refers to altering the physical design or configuration of the TES. Structure modification is important because it can improve the efficiency, durability, and functionality of TES, making them more practical and effective for self-powered sensor applications. Z. Lin, *et al.* introduced a novel energy harvesting device known as pendulum-inspired triboelectric nanogenerator (P-TENG) (Figure 22a-22c). The P-TENG consisted of PTFE and Cu as the triboelectric pair. The results show that the pendulum-inspired structure allows it to efficiently capture ultra-low-frequency mechanical energy. In addition, the device demonstrates high output signals. As shown in Figure 22d, the V_{OC} and I_{SC} of the P-TENG is value of around 55 V and 0.6 μA, respectively.
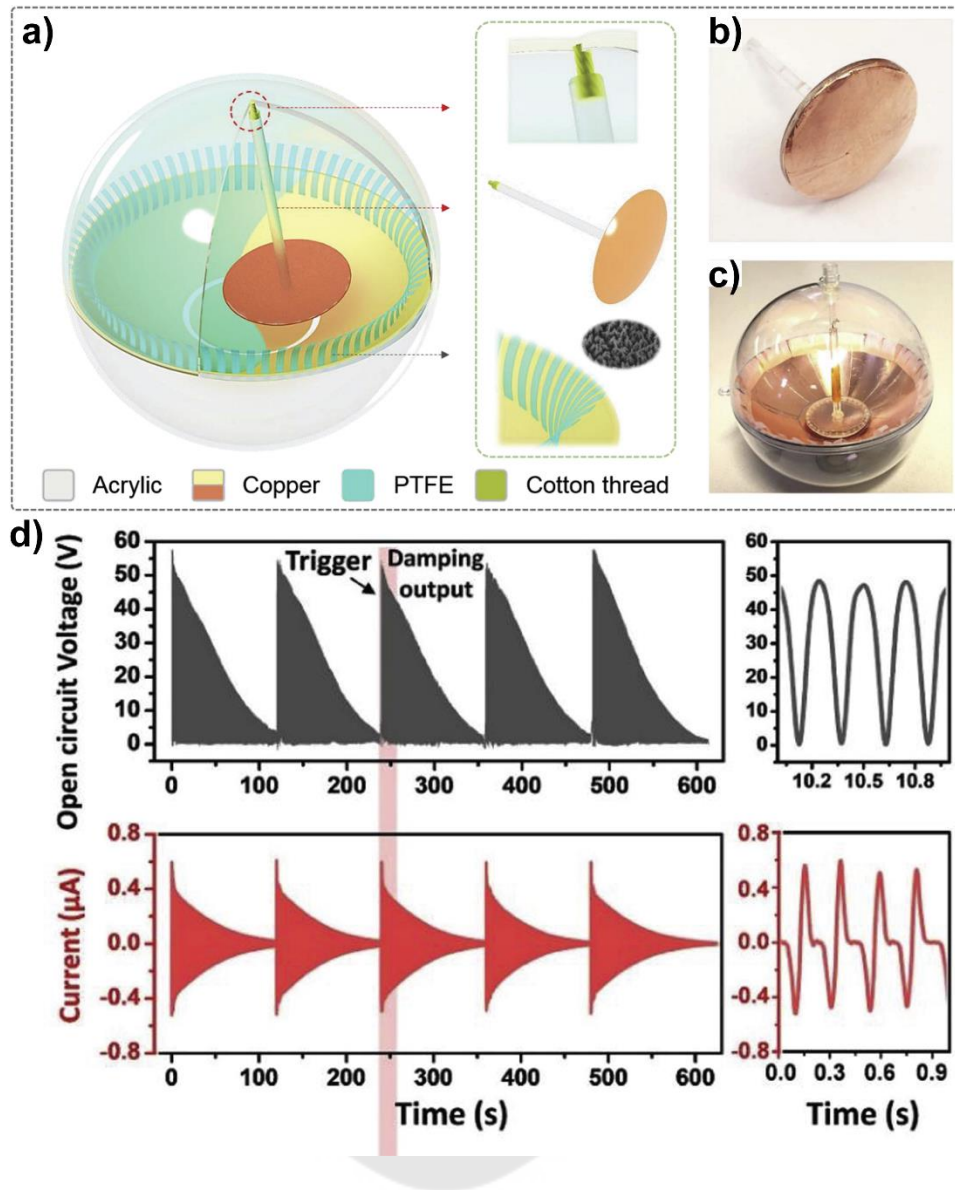
Figure 22 a-c) Schematic illustrations of the P-TENG, d) The V_{OC} and I_{SC} of the P-TENG.

Source: Z. Lin (2019) Nano Energy p.103908.

Liao J, *et al,* (42) designed a nestable arched triboelectric nanogenerator (NA-TENG). The device component consisted of two silicone rubber arch layers: one has aluminum (Al) film on the silicone rubber surface while the other is silicone rubber as shown in Figure 23a. The device can be made for many layers. With the increasing of layers, the electrical output will be enhanced. As illustrated in Figure 23b, the peak value

of the V_{OC} is around ~2.4-2.7 V, while the peak value of the I_{SC} is around ~10-15 nA. In this study, NA-TENG was employed as a sensor detect the movements of knuckles (Figure 23b-23c). With the structural design, it can not only optimize the outputs but also provide an interesting approach to design new style of TES devices for wearable sensor applications.
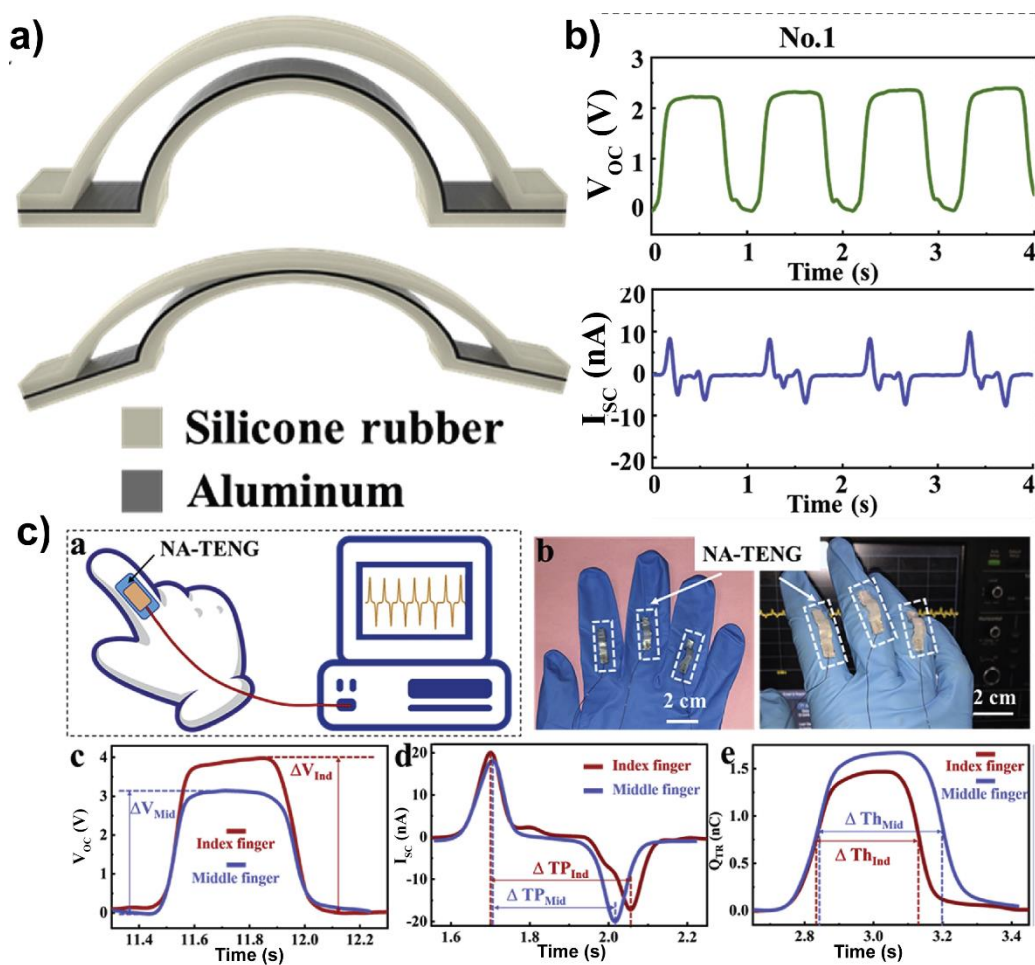
Figure 23 a) NA-TENG structure, b) V_{OC} of the two devices and I_{SC} of the two devices and c) Diagram of NA-TENG applied on finger and comparison of V_{OC}, I_{SC} and QTR of NA-TENGs applied on index and middle figures.

Source: J. Liao (2020) Nano Energy p.104417.

Modifying the structure of the TES can improve its performance and versatility. With the appropriate structure, the performance of the TES device can be improved or adapted for specific applications. In the design process, the mentioned parameters hold significance for developing a TES proficient in detecting low-frequency mechanical forces and producing a clear electrical signal. This adaptability paves the way for the device to evolve into a functional application. Consequently, this study aims to develop a TES for PD monitoring, with careful consideration of these diverse parameters during the design process.

2.7 Automatic Watch

The automatic self-winding watch is believed to have been first invented in the 1770s. Collecting energy from the wearer's movements is the core idea behind the automatic winding device. The automatic winding mechanism is able to harness the kinematic energy of the body's movements to power the mechanical watch movement (80). The digital images of automatic watch are shown in Figure 24a. The oscillating plate (rotor) is a key component of the automatic movement, and its function is essential to the watch's ability to wind itself and operate without the need for manual winding or a battery. The motion of the wearer's wrist and the rotor's movement in an automatic watch work together. As the wearer moves their wrist, the oscillating plate rotates, and this motion generates kinetic energy. This energy is transferred to the mainspring, which powers the watch's movement. The image of oscillating weight is demonstrated in Figure 24b.
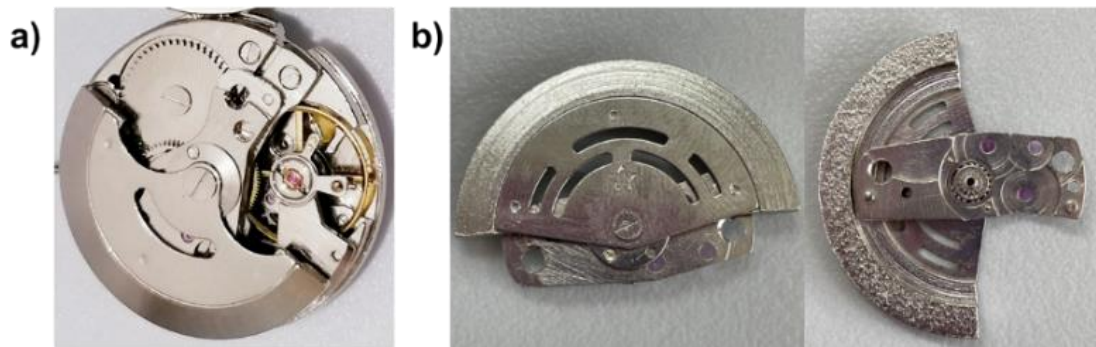
Figure 24 a) Automatic watch, b) oscillating plate front and back

Source: https://www.ebay.com/itm/304345920560

2.7.1 Automatic Watch Mechanism-based sensor

The mechanism used in automatic watches, which captures and stores energy from motion, has inspired research and development of energy harvesting devices. These devices are designed to convert various forms of mechanical motion into electrical energy for a wide range of applications, including powering small electronic devices, sensors, and wearable technology. Zurbuchen A, *et al*. colleagues explored the potential of energy harvesting devices as an alternative power source for pacemakers. The authors adapted the mechanism found in automatic wristwatches to convert the kinetic energy of the heart's contractions into electrical energy. The results indicated the new design's promise in harnessing heart motion for powering medical implants. The component of automatic watch and the harvesting device structure are shown in Figure 25a-b (81).
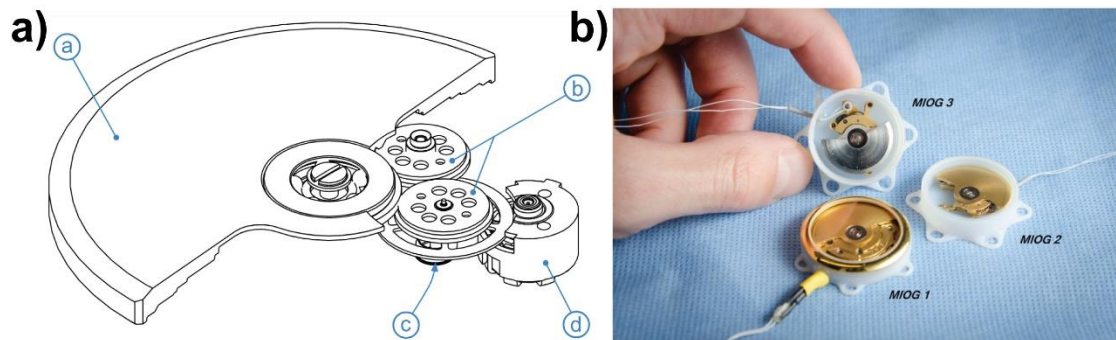
Figure 25 a) Schematic and component of automatic watch, b) The harvesting devices

Source: Zurbuchen A (2017) IEEE Trans. Biomed. Circuits Syst p.78-86.

Similarly, Zurbuchen A, *et al.* demonstrated the potential for battery-free cardiac pacing using a custom-made pacemaker. The device powered by an energy harvesting mechanism inspired by the automatic clockwork of a wristwatch. The energy harvesting mechanism is shown in Figure 26a. The in vivo experiment was performed. The results show that when heart movements accelerated, it allowed the harvesting mechanism to extract enough energy to power the internal pacemaker electronics. Moreover, the device can perform continuous at 120 beats/min and the heart beats signal is shows in Figure 26c (82).
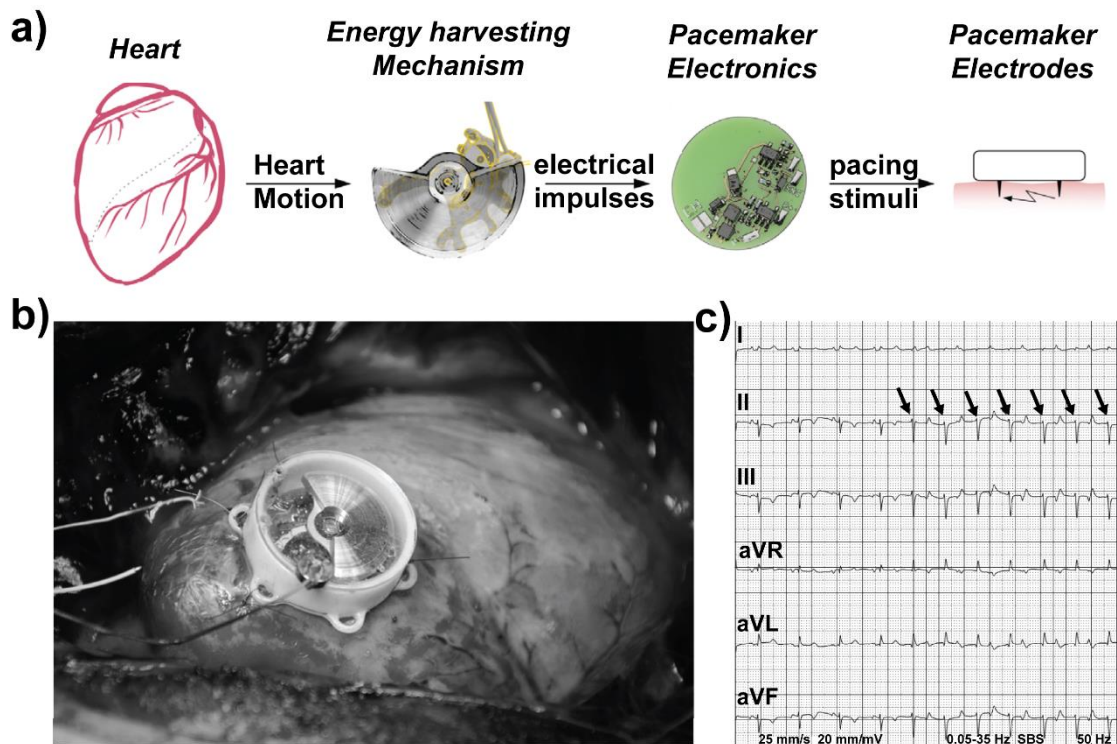
Figure 26 a) Working principle of the device, b) In vivo pacing: Pacemaker sutured on the heart and c) Electrocardiogram of the pacing period

Source: Zurbuchen A (2017) Heart Rhythm p.294-9.

Using an automatic watch mechanism for energy harvesting in health monitoring applications is an interesting concept. The motion of the wearer's wrist, which winds the watch's mainspring, could potentially be harnessed to generate electrical power for sensors or other components in a health monitoring device. Furthermore, applying the automatic watch mechanism to monitor Parkinson's disease (PD) symptoms has not yet been studied. Therefore, in this work, the author is interested in adapting the automatic watch mechanism with a triboelectric nanogenerator (TENG) for developing a triboelectric sensor for PD monitoring.

CHAPTER 3
RESEARCH METHODOLOGY

The fabrication of a TES for PD monitoring is outlined in a seven-part experiment. First, materials were prepared by selecting an oscillating plate from an automatic watch and PTFE as the tribo-positive and tribo-negative materials, respectively. The PTFE surface was then modified by sandpaper polishing to improve performance. All materials were characterized using techniques such as SEM, EDS, AFM and ATR-IR. Next, a regular free-standing triboelectric sensor (FS-TES) was fabricated to optimize operating parameters such as electrode spacing and operating frequency. The wristwatch-like triboelectric sensor (WW-TES) device frame was then designed using Shapr3D and fabricated using 3D printing. The electrical output signals from both FS-TES and WW-TES devices were evaluated using an oscilloscope and digital multimeter. Finally, the application of the sensor for PD monitoring was tested through activities based on the Unified Parkinson's Disease Rating Scale (UPDRS).

3.1 Materials Preparation

3.1.1 Materials and Equipment

- Oscillating plate

- Polytetrafluoroethylene (PTFE) (commercial grade, Polytechindustry)

- Conductive aluminum tape (Al tape) (RS Components Co., Ltd)

- Electrical wire

- PLA filament

- 3D printer (Raise3D)

- Double-sided adhesive tape

- Vortex shaker (GENIE2)

- Orbital shaker (SK-O330-Pro)

3.2 Material Surface Modification

Firstly, the PTFE was carefully cut into a 2cm x 2cm square to ensure uniformity of size. It was then thoroughly cleaned by immersion in ethanol, followed by ultrasonic cleaning for 10 minutes. After ultrasonic cleaning, the PTFE sample was allowed to air dry naturally. Finally, enhancing the surface area of PTFE for increased contact can be achieved through surface roughening. This process involves sanding the PTFE with sandpaper. In this case, 1000-grit sandpaper was utilized. The PTFE surface was sanded unidirectionally across the surface with a defined polishing cycle repeated 20 times to create a controlled pattern. The modified surface PTFE was obtained as shown in Figure 27.
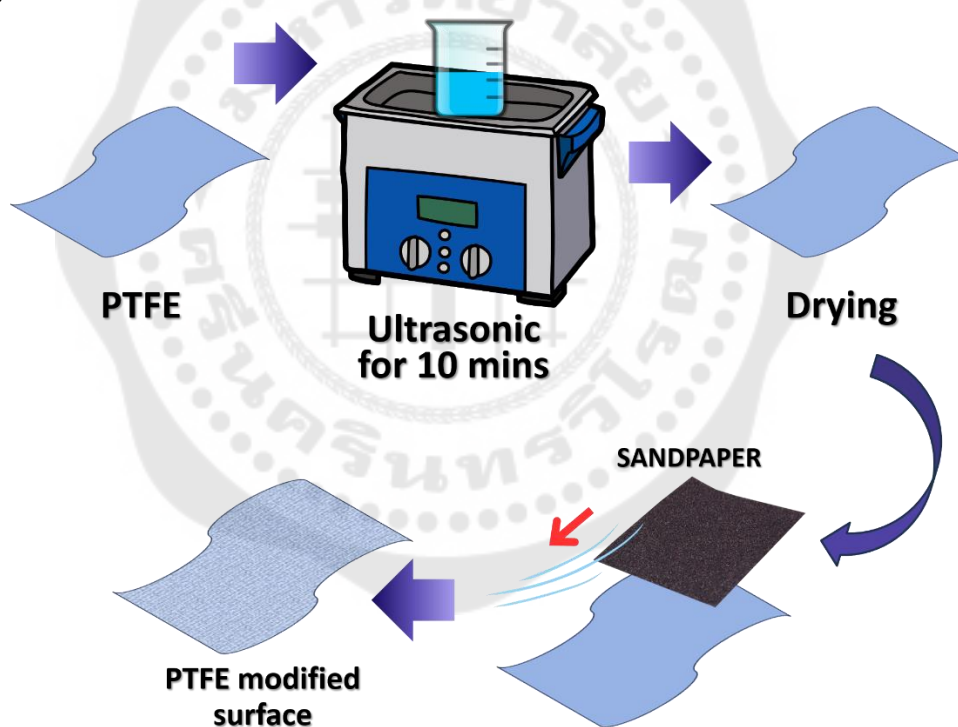
Figure 27 The material surface modification process

3.3 Characterization Techniques of Materials

3.3.1 Scanning Electron Microscope (SEM)

A scanning Electron Microscopy (SEM; FEI QUANTA 250) with the secondary electron detector at accelerating voltages of 20 kV was utilized to study the morphology

of the surface morphology of PTFE both normal and roughen. Moreover, the mechanism at microscale of free-standing mode TES was also studied. Figure 28 shows SEM equipment. For surface morphology, the pristine and modified PTFE films were cut into 1 cm ✕ 1 cm and attached onto the stub. In order to investigate the microscale insight of the free-standing mode TENG mechanism, the sample was prepared for regular FS-TES using the methods described in section 3.4. However, for this particular investigation, the sample was cut to dimensions suitable for stub mounting. It was then mounted on the stub following the specified four step movement mechanism of the FS-TES. The samples then underwent gold coating for a duration of 90 seconds prior to imaging with the SEM. This process was implemented to enhance their conductivity, ensuring optimal performance during imaging.

Figure 28 Scanning Electron Microscope (SEM)

Source: https://th.jeol.com/products/scientific/sem/

3.3.2 Electron Backscatter Diffraction (EBSD)

EBSD is typically performed in a scanning electron microscope (SEM). A focused electron beam is directed at the sample's surface. When the high-energy

electrons interact with the atoms in the sample, they scatter in various directions. Some of these electrons are backscattered towards the detector. The SBSE was employed to study the chemical composition of commercial SUS304 stainless-steel and oscillating weigh stainless steel. The samples were cleaned prior to analysis. It is ultrasonicated in ethanol for 10 minutes to ensure thorough removal of any contaminants. The plate is then allowed to dry completely before it is ready to be attached to the stub for examination.

3.3.3 Atomic Force Microscopy (AFM)

AFM operates on the principle of measuring the interaction forces (typically van der Waals forces) between the atoms on the tip and those on the sample surface. As the probe scans the sample, these forces cause the cantilever to bend, and this bending is detected and used to create an image of the surface. AFM was assisted to determine the surface morphology of PTFE both normal and roughen. Figure 29 shows AFM equipment. This work employs Dynamic Force Mode (DFM) with a 20-um scanner equipped with a cantilever composed of Si, N-type material, coated with Al (Reflex Side). The cantilever dimensions are specified as follows: a length (L) of 225 um and a width (W) of 40 um, with a resistance ranging from 0.01 to 0.025 ohm/cm. The spring constant (k) falls within the range of 36 to 90 N/m. The cantilever's resonance frequencies range from 160 to 225 kHz. DFM scans an area of 10 um x 10 um at a scan speed of 0.5 to 0.7 Hz. The sample was cut to a size of 1 x 1 cm² and mounted onto silica substrates using adhesive tape. For the modified PTFE, the surface with the modification faced upwards for examination. Samples are carefully loaded into the AFM chamber, where they undergo scanning with a cantilever-tipped probe. The probe interacts with the sample surface, generating high-resolution topographical images and data.

Figure 29 Atomic Force Microscopy (AFM)

Source: https://qd-europe.com/nl/en/products/spectroscopy/atomic-force-microscopes-for-research/

3.3.4 Attenuated Total Reflectance Fourier Transform Infrared Spectroscopy (ATR-FTIR)

Infrared (IR) radiation is used as a source of energy. This IR radiation consists of wavelengths that are within the infrared region of the electromagnetic spectrum. The IR region corresponds to the vibrational frequencies of chemical bonds in molecules. ATR-IR spectroscopy (ATR-IR; Shimadzu IRTracer-100) was employed to analyze the functional groups and identify the PTFE film in the spectral range of 4000-550 cm^{-1}. Figure 30 shows the ATR-IR spectroscopy equipment. For investigation, both samples, pristine PTFE and modified PTFE, were cut into the size of 1x1 cm² before being analyzed in the range of the ATR-IR spectrum within 4000-550 cm^{-1}.

Figure 30 Attenuated Total Reflectance Fourier Transform Infrared Spectroscopy (ATR-FTIR)

Source: https://www.ktssci.com/category.php?id=44

3.4 Regular Free-Standing Mode Triboelectric Sensor (FS-TES) Fabrication

The regular FS-TES device consists of two electrodes and a tribomaterial pair, namely PTFE and stainless steel. The assembly process involved taking a 2cm x 2cm piece of modified PTFE, attaching Al tape to it, and connecting it to an electrical wire. This process was repeated to create two sets of PTFE-attached Al electrodes. Additionally, a 2cm x 2cm stainless steel sheet was cut and subjected to ultrasonic cleaning in ethanol for 10 minutes. Subsequently, this cleaned stainless steel sheet was utilized as the contact material on one side of the FS-TES device as shown in Figure 31.

Modified PTFE   **Al electrode**   **Electrical wire**

Stainless-steel

Regular Free-standing Mode TES structure
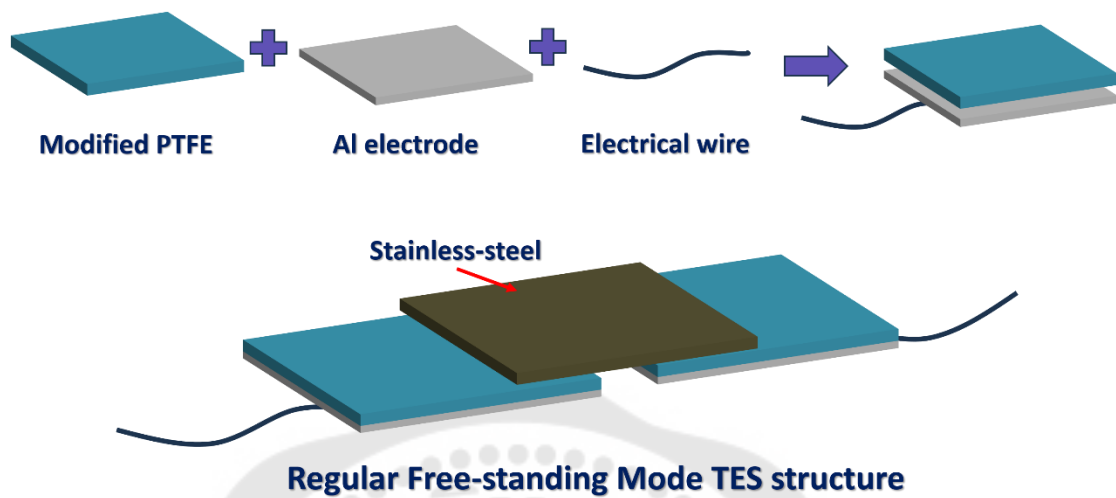
Figure 31 The regular FS-TES fabrication process

3.5 Design of the Wristwatch-Like (WW-TES) Device

The device frame fabrication process involved several key steps, each essential for creating a functional and precisely designed device frame. The process begun with designing the device frame using the Shapr3D program. The frame was designed to be cylindrical with specific dimensions: a width, height, and diameter of 2, 7, and 34 mm, respectively. The frame featured two additional areas extending outward, equipped with strategically placed holes in the wall to allow electrical wires to pass through to the exterior. In the center of the frame, a designated platform was provided for attaching an oscillating weight. With the 3D model ready, the next step was to bring it into the physical realm through 3D printing. A Raise3D 3D printer was used for the printing process. PLA filament was chosen as the printing material. The printing process was completed in approximately 28 minutes. The device's frame fabrication process is illustrated in Figure 32.
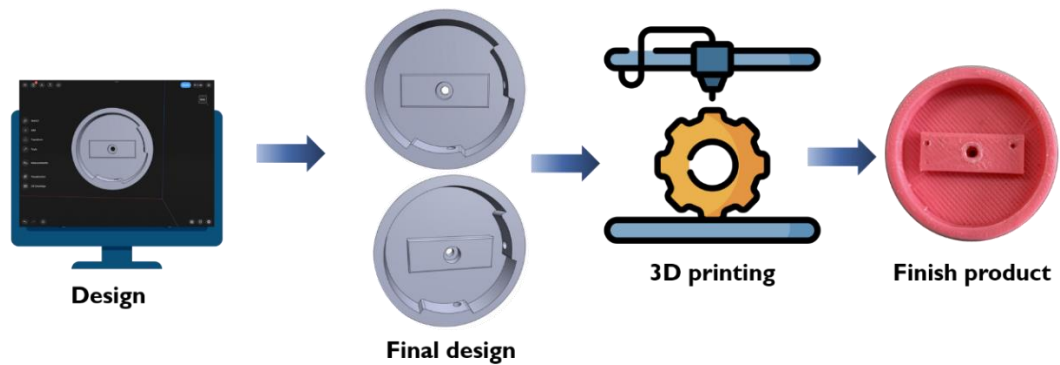
Figure 32 The fabrication of the device's frame

3.5.1 The Device Assembly

The device was designed to operate in free-standing mode. First, a surface-modified PTFE was attached with aluminum tape as an electrode and connected to electrical wires. This was then attached to the frame using double-sided adhesive. The electrical wire was routed out of the frame through holes on the side. The same action was repeated on the other side of the electrode. Next, the oscillating plate was attached to the middle part of the device using hot glue. Additionally, a nut and metal bearing were attached to the oscillating plate to add weight. Finally, careful attention to detail was required to confirm that the PTFE and oscillating plate will indeed make precise contact as intended. The steps of device assembly are demonstrated in Figure 33.
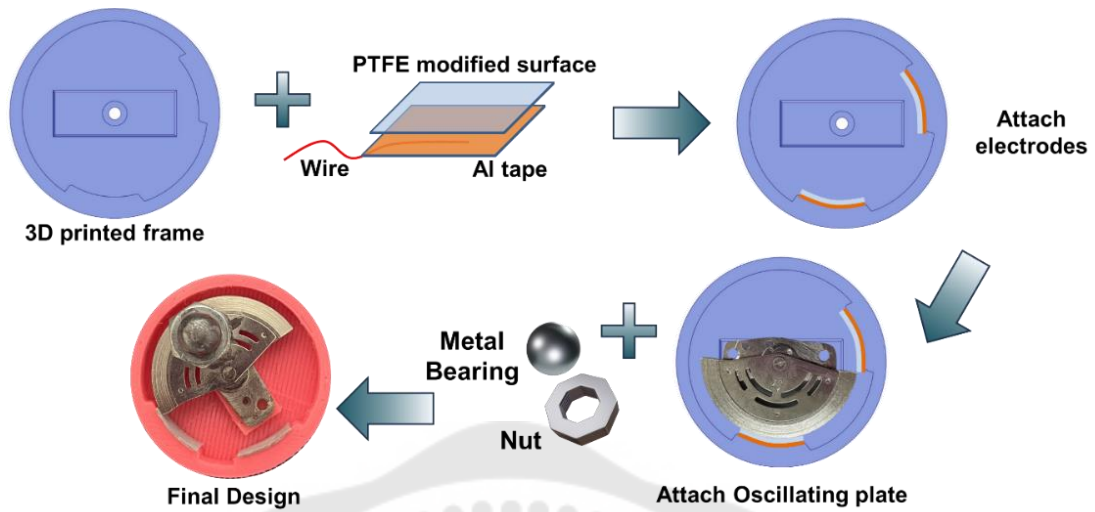
Figure 33 Schematic of device assembly

3.6 Electrical Output Performance

The electrical output performance in this study can be divided in two parts. First, the output including V_{OC} and I_{SC} was measured for the regular free-standing mode TES using stainless steel and PTFE. The samples were cut into 2 x 2 cm^2. The electrical output study involves varying the distance between the electrodes to 0, 5, 12, 17, and 35 mm and varying the frequency from 3 to 7 Hz. The electrical output was obtained using an energy-harvesting automatic sliding machine. The frequency of this machine was controlled by adjusting the motor speed, allowing observation of its effect on the electrical output. Measurements were taken using an oscilloscope and a Digital Multimeter (DMM).

In the second part of the study, the output performance of the PD sensor WW-TES, including V_{OC} and I_{SC}, was measured. The effects of varying the distance between the electrodes (0, 5, 12, 17, and 35 mm) and the frequency, corresponding to the severity of PD tremors (ranging from 3 to 7 Hz), on the output of the WW-TES device were investigated using an orbital shaker for mechanical input as shown in Figure 34a-c, respectively.

Figure 34 a) Oscilloscope, b) Digital multimeter and c) Orbital shaker

3.7 Activities Test for Parkinson's Disease Monitoring.

Once the TES device for measuring PD was assembled, a crucial step involved testing its functionality and practicality. To assess its usability, the device undergoes experimentation by affixing a strap, allowing it to be worn on the wrist like a watch. The experimentation included simulating shaking, mimicking the tremors associated with varying degrees of PD severity through activity testing, involving tasks such as water pouring, eating, writing, *etc*. Testing each activity required wearing a TES device on the wrist, which subsequently shakes or mimics vibrations based on the frequency of the disease. This procedure adhered to the severity scale of the Unified Parkinson's Disease Rating Scale (UPDRS), which classifies the disease on a scale of 0-4 based on its frequency. Level 0 represents normal Level 1 indicates slight, low-frequency tremors (0.5-0.9 Hz) with no significant impact on function. Level 2 represents mild tremors with a frequency of 0.9-1.8 Hz, causing a modest impact on function. Level 3 signifies moderate tremors occurring at a frequency of 1.8-3.4 Hz, considerably affecting function but not preventing it. Level 4 denotes severe tremors with a frequency exceeding 3.4 Hz, leading to symptoms or signs that prevent normal function. Throughout the experiment, shaking was executed at the designated frequency for 50 seconds during each activity. The resulting signal corresponded to the tremor frequency within the UPDRS severity scale.

CHAPTER 4

RESULTS AND DISCUSSIONS

This chapter presents detailed results and discussions stemming from efforts to design and develop a triboelectric sensor specifically tailored for monitoring Parkinson's disease tremors. This includes discussions on material modification, sensor design, and structural optimization. Subsequently, the electrical output performance of the developed sensor is evaluated. Furthermore, practical implications of the sensor design in the context of Parkinson's disease (PD) tremor are explored through activities of daily living (ADLs), such as pouring water and eating, based on the MDS-UPDRS scale. These discussions highlight the sensor's potential for providing real-time tremor monitoring capabilities in a non-invasive manner.

4.1 Material Characterization

4.1.1 The Characterization of Polytetrafluoroethylene (PTFE) Film Before and After Surface Modification.

4.1.1.1 Characterization by Attenuated Total Reflectance Fourier transform Infrared (ATR-FT-IR)

Initially, PTFE film was selected as the tribo-negative material for the sensor construction. The commercial PTFE chosen underwent thorough characterization using ATR-IR technique to verify its functional groups. According to Figure 35 (Red), shows the ATR-IR spectra at 4000-550 cm^{-1} range of pristine PTFE film. The characteristic absorption peaks of CF_2 groups at 1201 cm^{-1} (C–F symmetric stretching) and 1145 cm^{-1} (C–F asymmetric stretching). Additionally, peaks located at lower wavenumber around 637 cm^{-1} is indicated to CF_2 rocking, aligned well with known PTFE peaks reported in the literature (83, 84). Following the confirmation of the PTFE's chemical composition, surface modification was performed using sandpaper polishing. Sandpaper polishing is a simple and cost-effective method to modify the surface roughness of PTFE. This

process involves rubbing the PTFE surface with sandpaper of 1000 grit size and polishing in a unidirectional manner. This physical modification aimed to enhance the output of the TES. The modified PTFE sample was characterized by using ATR-IR to assess any changes in their chemical properties. The ATR-IR analysis of the modified PTFE samples revealed that despite the physical surface modification through sandpaper polishing, there were no significant changes in the chemical properties of the PTFE as shown in Figure 35 (blue). According to Figure 35 (blue), the strong absorptions 2101 cm^{-1} (C–F symmetric stretching) and 1146 cm^{-1} (C–F asymmetric stretching) relate to the CF_2 stretching vibrational, while the signal at 633 cm^{-1} can be attributed to the deformation vibration of the segment CF_2 rocking (85). This indicates that the surface modification process successfully altered the surface morphology of the PTFE while the chemical structure of PTFE remained unchanged throughout the polishing process. Table 2 demonstrates the ATR-IR pattern of the pristine PTFE and rough PTFE.

Since surface modification plays a pivotal role in advancing the capabilities of triboelectric materials, making them more efficient, several research have investigated various surface modification methods to improve the surface properties of triboelectric materials such as Inductively coupled plasma (ICP) (86), Neutral beam (NB) treatment (87), soft lithography (88), photolithography (89), ultrafast laser patterning (90), block copolymer (BCP) self-assembly (91), Ion Injection (92). The above process can be categorized into two types: physical surface modification and chemical surface modification. Physical modification involves altering the material's physical properties, such as surface texture or morphology, without changing its chemical composition. Chemical modification, in contrast, entails altering the material's chemical structure, which can sometimes lead to the degradation or transformation of the original chemical makeup. Moreover, surface functional groups tend to detach under mechanical wear, making them impractical for application (93). Therefore, this work proposes a simple method for modifying surface roughness, such as sandpaper polishing, without compromising the chemical integrity of the material.
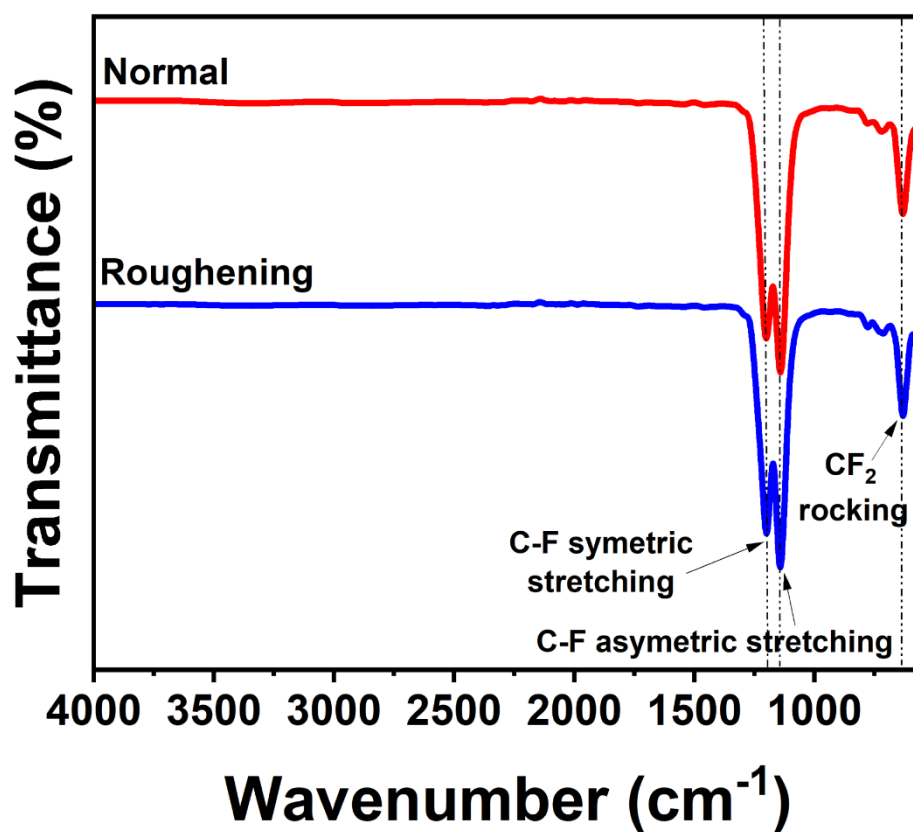
Figure 35 ATR-IR pattern of the pristine PTFE and modified PTFE

Table 2 ATR-IR pattern of the pristine PTFE and roughed PTFE

Wavenumber (cm^{-1})		Characteristic bond
Pristine PTFE	Modified PTFE	
2102	2101	C–F symmetric stretching
1145	1146	C–F asymmetric stretching
637	633	CF$_2$ rocking

4.1.1.2 Characterization by Scanning Electron Microscope (SEM)

The morphological characteristics of PTFE were investigated using Scanning Electron Microscopy (SEM; FEI QUANTA 250) with the secondary electron

detector at accelerating voltages of 20 kV. Figure 36a and b display the SEM images at 100x magnification of the pristine PTFE and surface modified PTFE film, respectively. According to Figure 36a, the surface of the pristine PTFE film showed a fairly smooth and uniform surface, indicating its initial unaltered state. However, the surface morphology clearly changed after polishing with sandpaper for 20 times in unidirectional as shown in Figure 36b. The surface of the polished PTFE film appears to have noticeable streaks on the surface, showing a much rougher texture. This indicated that the surface of PTFE film was successfully modified. The surface pattern was similar to those in previous research, where the tribomaterials underwent surface modification with polishing, which resulted in improved overall output performance (40, 94, 95). Previous research has attempted to improve the roughness of PTFE surfaces using various methods. For instance, plasma treatment has been employed to create nanowire-like structures or ridge patterns on the surface (96). Similarly, Inductively Coupled Plasma Etching (ICP) has been utilized to produce PTFE film with nanowire-like structures on the surface (97, 98). Another technique involves the use of anodic aluminum oxide (AAO) to form nanostructures on the PTFE surface (99). Additionally, thermal imprinting lithography (TIL) has been applied to achieve micro-grooved architectures (100). These methods have enhanced the triboelectrification efficiency of PTFE-based TENGs, resulting in increased electrical output values. However, they often require specialized equipment and are complex. In contrast, sanding the PTFE with sandpaper, as used in this study, offers a simpler and more accessible alternative. Despite its simplicity, this method effectively roughens the PTFE surface, leading to significant improvements in electrical output values.
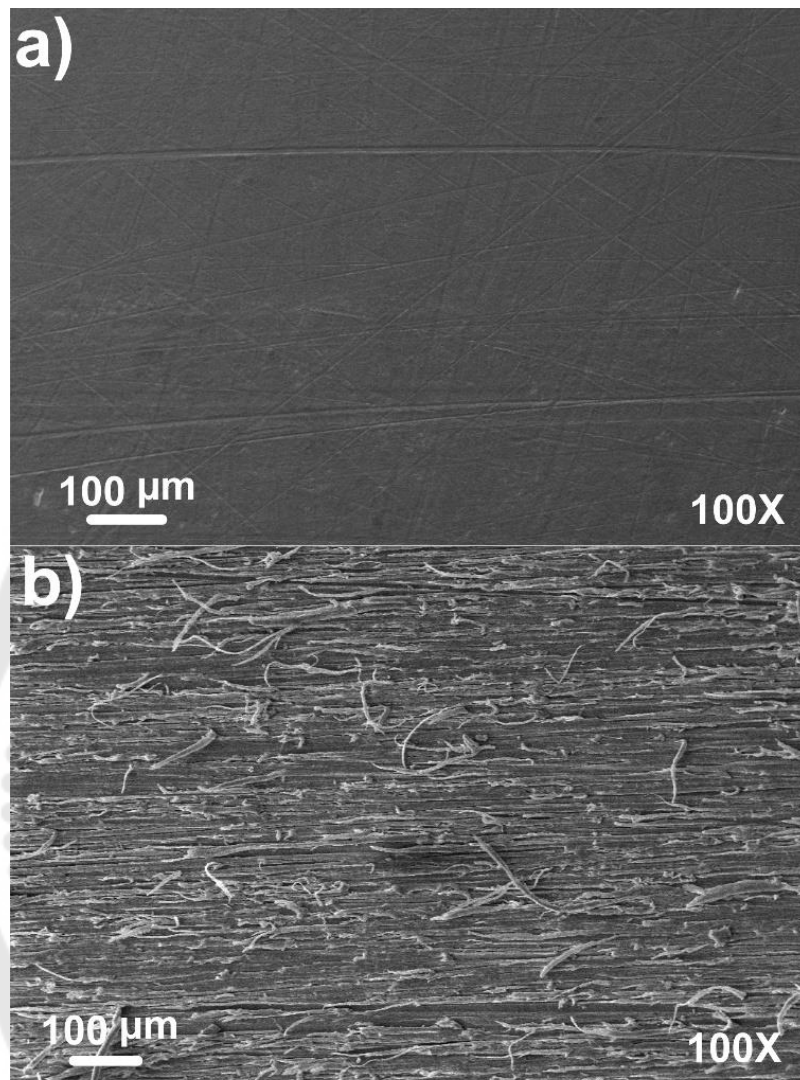
Figure 36 FSEM images showing the surface morphology of PTFE films a) pristine PTFE film and b) modified PTFE film by sandpaper polishing

4.1.1.3 Characterization by High-Resolution Atomic Force Microscopy (AFM)

The surface roughness of PTFE film was analyzed by AFM technique within Dynamic Force Mode (DFM), also known as tapping mode. This mode of operation allows for high-resolution imaging of surfaces by gently tapping a sharp probe tip onto the sample surface, minimizing damage or distortion. A specialized AFM system equipped with a 20 μm scanner was utilized for these measurements, enabling precise scanning over the sample area. The silicon cantilevers coated with a thin reflex aluminum

coating, featuring nominal spring constants (k) ranging from 36-90 N/m and resonance frequencies of 160-225 kHz, were employed. The results of AFM images are shown in Figure 37 with a scan area of 10 μm × 10 μm providing detailed visual representations of the surface topography and 3d orthographic image. The topography images provide a surface top view of the film, with depth information in the Z-direction represented by color intensity. Light-colored regions indicate the highest points or peaks, while dark-colored regions signify the lower points. Additionally, the 3D orthographic images offer three-dimensional representations of the same surface areas, giving a more comprehensive view of the surface topography. Figure 37a and 37b show the AFM images of the pristine PTFE and modified PTFE film, respectively. For the top view topography images of pristine PTFE, the surface appears relatively smooth, with minimal variations in height. The light regions indicate the highest points on the surface, which are evenly distributed. After modification by sandpaper polishing, the surface exhibits a markedly different texture. The light regions, representing the peaks, are more prominent and numerous, indicating increased surface roughness. The 3D orthographic images of pristine PTFE reveal a mostly flat surface with subtle variations in height. The peaks are low and uniformly spaced, giving the surface a smooth appearance. In contrast, the 3D image of the modified PTFE showcases a dramatically altered surface topology. The peaks are higher and more pronounced, and the surface features numerous grooves and valleys created by the sandpaper. This increased roughness and texture are clearly visible in the three-dimensional view, illustrating the significant impact of the sandpaper polishing process.

Therefore, analysis of the AFM images revealed evident changes in the surface roughness of the PTFE film following the modification process. The root means square roughness (Sq), which quantifies the average deviation of surface height from the mean plane, was determined to be 45.4 nm with surface area of 101.16 μm^2 for the pristine PTFE film. However, after undergoing surface modification using sandpaper polishing, the Sq value increased substantially to 227.9 nm with an increasing surface area of 111.32 μm^2. The Sq value of modified PTFE was 5 times higher than that of

pristine PTFE. The root means square roughness (Sq) values derived from AFM data of all the samples are presented in Table 3. The detailed AFM results confirm that after polished PTFE film surface with sandpaper the surface roughness was significantly improved.
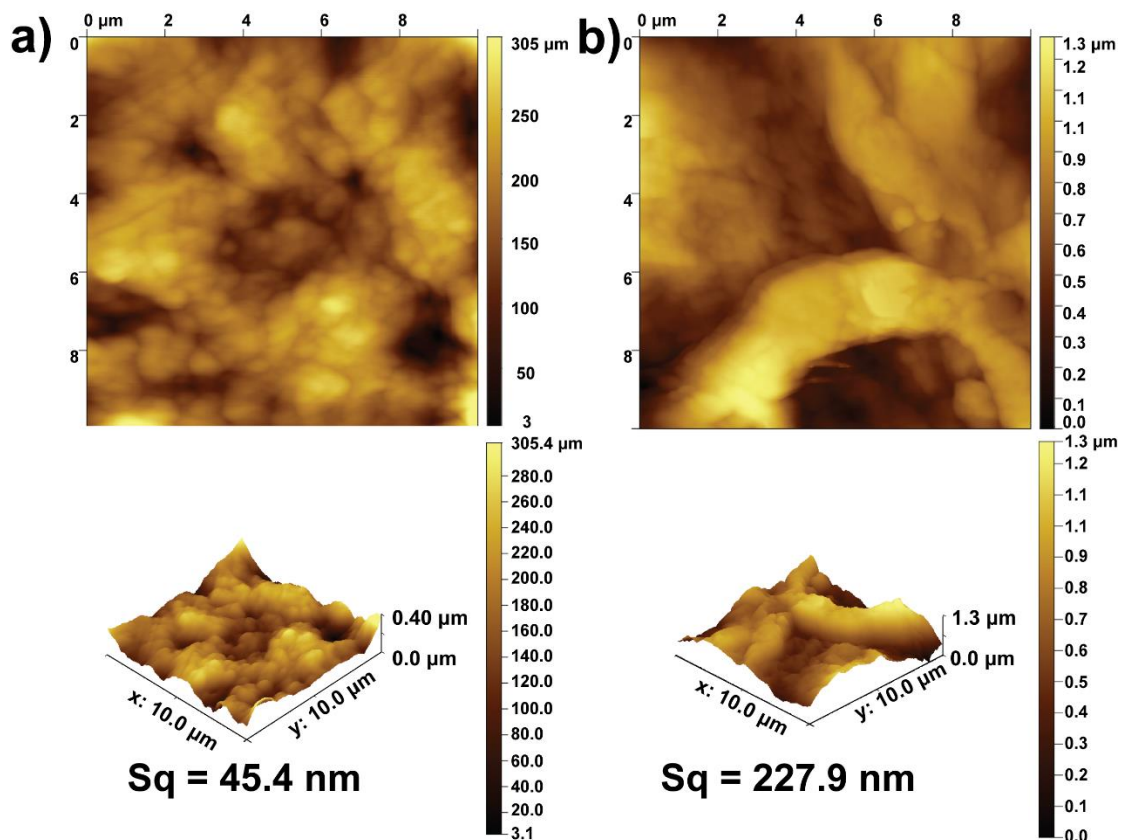
Figure 37 AFM images of PTFE film a) pristine PTFE film and b) modified PTFE film by sandpaper polishing

Table 3 AFM analysis of Sq values, surface areas of pristine PTFE and modified PTFE

PTFE Films	Sq (mm)	Surface area (μm^2)
Pristine PTFE	45.4	101.16
Modified PTFE	227.9	111.32

4.1.2 The Characterization of Stainless-steel by the Energy Dispersive X-ray Spectroscopy (EDS) Technique

A commercial stainless-steel plate grade SUS304 with 0.5 mm in thickness was used as tribo-positive material for the fabrication of regular TES. The composition of SUS304 stainless steel is known for its specific alloying elements. The typical composition of SUS304 includes Chromium (Cr): 18-20%, Nickel (Ni): 8-10.5%, Carbon (C): $\leq$ 0.08%, Manganese (Mn): $\leq$ 2%, Silicon (Si): $\leq$ 1%, Phosphorus (P): $\leq$ 0.045%, Sulfur (S): $\leq$ 0.03% and Iron (Fe): Balance (101).

Metals, composed of atoms in a crystal lattice, do not have the molecular vibrations and dipole moments, hence they do not absorb IR radiation in a detectable way. Moreover, metals are highly reflective in the IR region of the spectrum. They reflect most of the IR radiation rather than absorbing it, which makes it challenging to obtain an IR spectrum of a metal. EDS, on the other hand, provides a direct and reliable method for characterizing the elemental composition of metals, making it the preferred technique for analyzing materials such as stainless steel. The identification of elements was characterized by the EDS as shown in the results in part 4.1.2.1. and 4.1.2.2

4.1.2.1 The Characterization of Commercial Stainless-steel

Stainless-steel Grade SUS304 was utilized in this work. Before being used for testing, the commercial SUS304 stainless steel was inspected to ensure its authenticity as a genuine stainless-steel. The stainless steel was prepared by cutting it into pieces of 0.5 × 0.5 cm. These pieces were then ultrasonically cleaned in ethanol for 10 minutes and allowed to dry. Once dried, the sample was attached to a stub and placed in a chamber for further analysis. The results of the compositional analysis by

EDS mapping are shown in Figure 38. It can be observed that elements such as Fe, Cr, Ni, Si, S, P, C, and Mn are found in commercial stainless steel grade SUS304, which has elements that comply with the specification certificate from reference (102). Confirmation that the material meets the expected standards for SUS304 stainless steel.
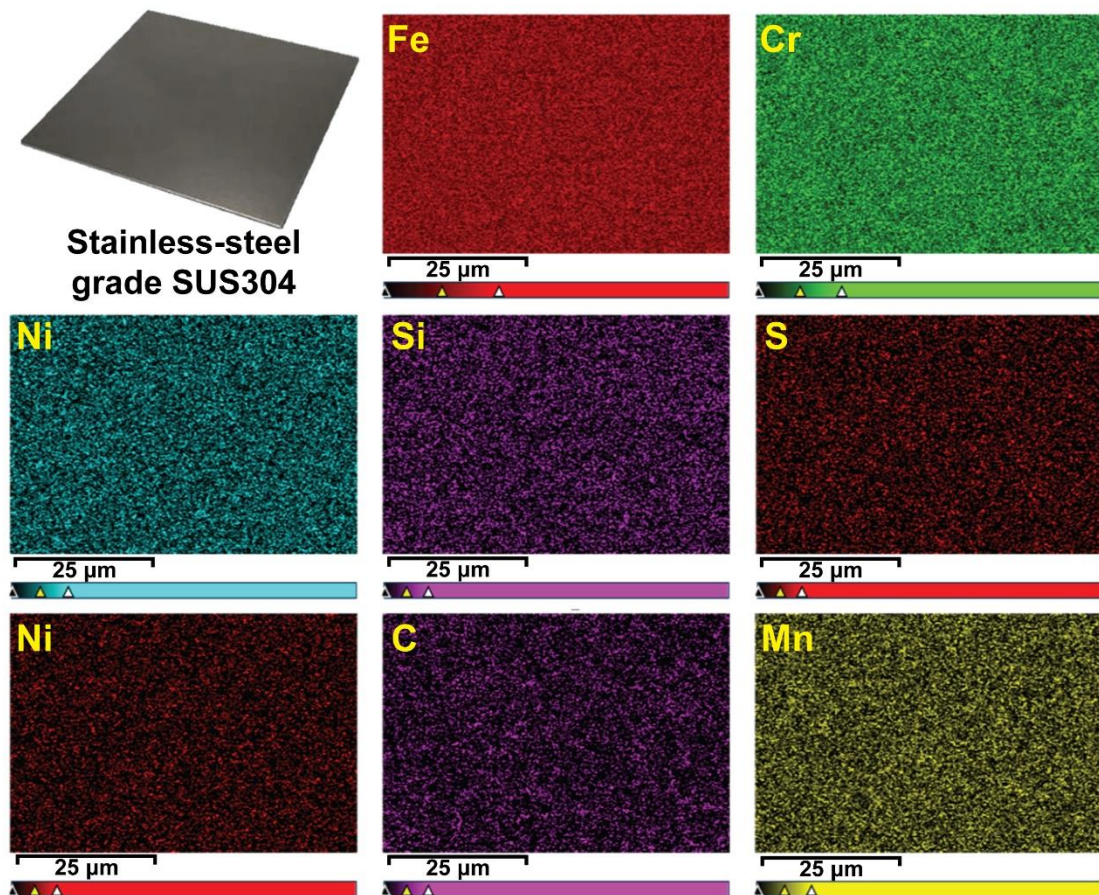
Figure 38 EDS mapping of commercial stainless-steel grade SUS304

4.1.2.2 The Characterization of Automatic Watch Oscillating Plate

Figure 39 shows digital image of oscillating plate and the EDS mapping analysis. The EDS elemental spectra and mapping of oscillating plate results showed the presence of elements consistent with stainless steel, including C, O, Si, P, S, Cr, Fe, and Ni elements by reporting its composition detailed in Table 4. Cr and Ni are the primary alloying elements of stainless steel. These findings are in agreement with prior research references (103, 104). This primarily confirms that the oscillating plate is manufactured

from stainless steel. It is important to note that EDS can identify the elemental composition of a material and confirm that it is stainless steel. Although oxygen (O) is usually not present in stainless steel, in this case, it appears in EDS results. This occurrence could be due to surface oxides that form as a result of the interaction of the stainless steel with oxygen in the surrounding environment (105, 106). Nevertheless, EDS cannot determine the specific type or grade of stainless steel.
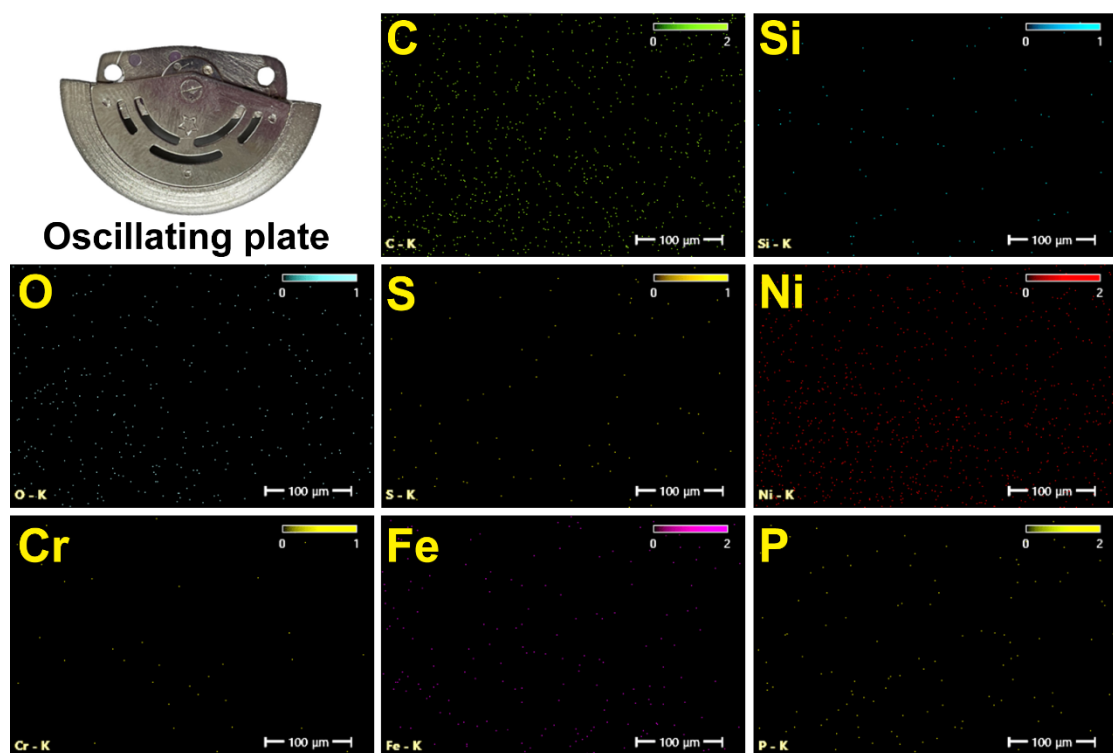
Figure 39 Digital image and EDS mapping analysis of oscillating plate

Table 4 EDS analysis results of elements on the surface of oscillating plate

Element	Atomic %	Atomic % Error	Weight %	Weight % Error
C	62.9	0.9	32.8	0.5
O	14.1	0.6	9.8	0.4
Si	0.1	0.1	0.1	0.1
P	0.8	0.1	1.1	0.1
S	0.0	0.0	0.1	0.1
Cr	0.0	---	0.0	---
Fe	2.2	0.2	5.4	0.4
Ni	19.8	0.5	50.6	1.2

4.2 Regular Free-Standing Mode Triboelectric Sensor (FS-TES) Device

4.2.1 Device Structure and Working Mechanism of the Regular FS-TES

The operating principle of regular FS-TES is based on in-plane charge separation mechanism (107, 108). The regular FS-TES device consists of a free-standing stainless-steel layer with a size of 2x2 cm^2. Two PTFE foils of the same size are connected to the Al tape acting as electrodes (2x2 cm^2) and are attached to the electrical wire for output to an external load. These components are arranged in parallel, with the stainless steel and PTFE films adjacent to each other. The stainless steel is mechanically moved back and forth from one edge of the left-hand PTFE film to the end edge of the right-hand PTFE film. In Figure 40 illustrate the operating principle of regular FS-TES. According to Figure 40, in the initial state (i), there is no mechanical force input to make the stainless-steel move and contact with the PTFE. Therefore, there's no current flow. However, when there is mechanical force triggers the stainless-steel to move and

touch PTFE on the left electrode (LE) in state (ii), a phenomenon known as charge exchange that occurs between the PTFE and stainless-steel materials. This exchange is initiated by the difference in their electronegativity levels, leading to the transfer of charges between the two materials. As a result, positive charges are created on the surface of the stainless-steel and negative charges are created on the surface of the PTFE layer through the triboelectric effect. As negative charges are collected on the PTFE film, an equal number of positive charges are induced in the LE. This makes electrons flow from the LE and accumulate in the RE. As a result, this step causes the flow of current. The current will continue to flow until reaching the equilibrium where the stainless-steel layer moves to completely cover the LE in state (iii). The stainless-steel was further moved towards the RE, gradually overlapping certain regions. This movement is accompanied by the transfer of positive charges from the surface of the stainless-steel layer. The positive charges on the surface of the stainless steel will induce negative charges on the PTFE film on the RE. Consequently, this induction process will result in some of the positive charges being transferred to the RE. As a result, electrons that were previously accumulated on the RE will flow through the load from the RE to the LE, producing an alternative current at state (iv). During this sliding movement, electrons continue to flow between the two electrodes to equalize the local potential differences. This electron movement continues until the system reaches its maximum electrical power, which the stainless-steel completely overlap the RE in state (v). This phase of electron transfer plays a crucial role in the first half cycle of the operation of the FS-TES. The second half of the cycle occurs during the reverse sliding movement, when the stainless-steel layer moves from the RE back to the LE. During this phase, electrons flow in the opposite direction, producing an electrical output corresponding to state (vi). This reverse sliding motion maintains the continuation of the AC cycle within the FS-TES system. The alternating contact and separation between the PTFE with Al electrode and the stainless-steel layer are sustained, resulting in an alternating current (AC) waveform.
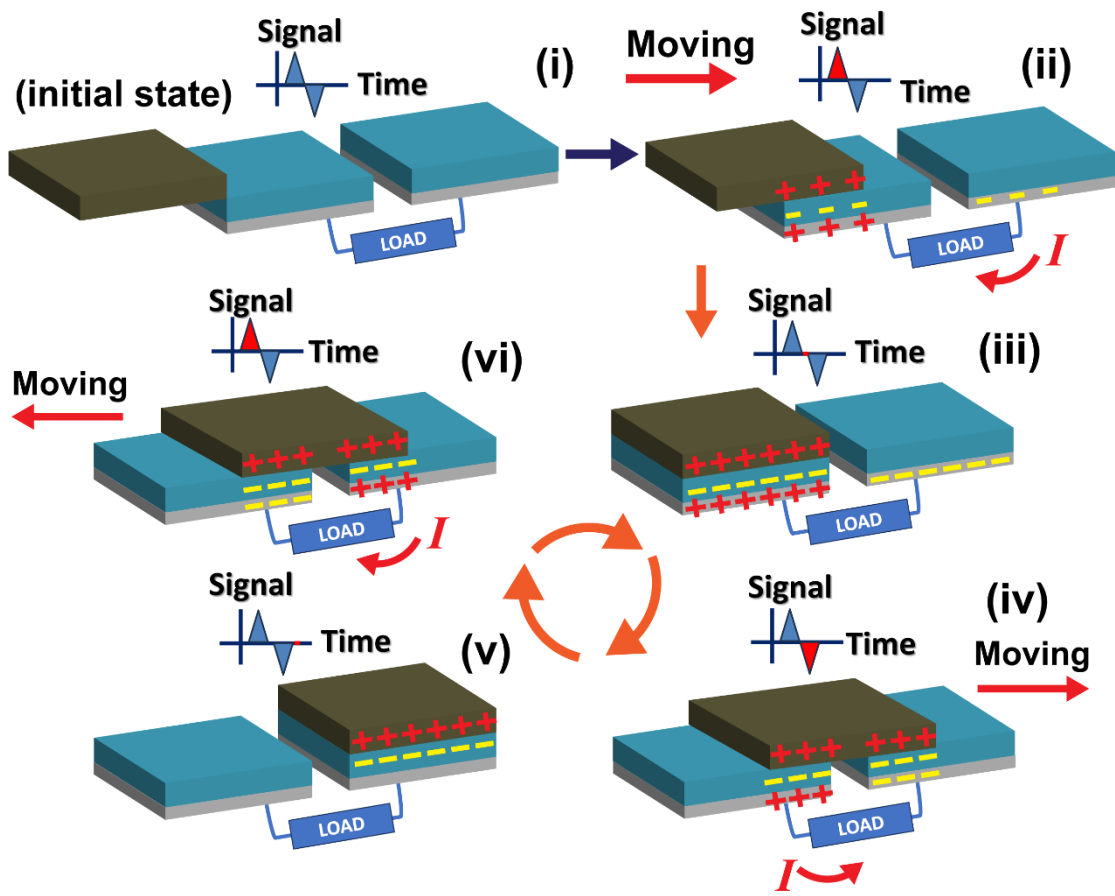
Figure 40 The working principle for traditional FS-TES device

In each contact-separation cycle, the total amount of transferred charges (Q) is determined by:

$$Q = lab \tag{1}$$

, where Q represents the surface triboelectric charge density on the PTFE's surface, and *a* and *b* denote the length and width of the friction area, respectively. The effective range of charge induction (*d*) is assumed to remain constant during both the sliding and FS-mode TES operations. The potential difference can be described by the equation (109):

$$V = \frac{-1}{C} * Q + V_{OC} = -d_0 + \frac{g}{\varepsilon_0 S} * Q + \frac{2\sigma x}{\varepsilon_0} \tag{2}$$

Where *V* is the potential difference between electrodes, *C* represents the capacitance, d_0 stands for the initial gap distance between components in the

nanogenerator, g is the gap distance between the two electrodes, ε_0 represents the permittivity of free space, *S* stands for the area size of the effective surface, σ is the charge density and ε stands the permittivity of the material used in the free-standing layer. The relationship between charge generation and V_{OC}, where *S* is the area size of the effective electrode 1 and 2 (109).

$$V_{OC} = \frac{\Delta Q_{SC} \cdot S}{c} \tag{3}$$

The enhancement of electrical output through increased surface area can be explained by equation (3) which indicates that the electrical output is dependent on the surface area (S). Therefore, increasing the surface contact area leads to a higher total electrical output (96). The generated current can be calculated using equation (4)

$$I = \frac{dQ}{dt} = \frac{\sigma ab}{d/v} = \frac{v\sigma ab}{d} \tag{4}$$

, where d and υ denote the electrode distances and relative speed of contact separation. The I_{SC} refers to transfer charge as a function of sliding time, which can be written as equation (5), which relies on the stainless-steel motion speed (110, 111).

$$I_{SC} = \frac{dQ_{SC}}{dt} = \frac{dQ_{SC}}{dx}\frac{dx}{dt} = \frac{dQ_{SC}}{dx}v \tag{5}$$

Following surface modification, the electrical performance of pristine and surface modified PTFE was investigated. According to Figure 41, it was found that the V_{OC} and I_{SC} of pristine PTFE were around ~17.59 V and ~71.20 nA, while those of modified PTFE were around ~29.53 V and ~112.94 nA. These values are approximately ~1.8 and ~1.6 times higher than those of unmodified PTFE, as shown in Figure 41a and 41b. The results are consistent with results previously reported in previous studies where surface modification was performed using sandpaper. The TENG shows a threefold increase in output voltage and a fivefold increase in power (94). Modifying surface roughness with sandpaper can improve electrical performance, as reported in studies discussing mechanisms for increased electrical efficiency (112, 113). By introducing textures onto the surface of the triboelectric layers, the effective contact area is significantly increased. When the textured surfaces come into contact with another

material, they create more points of interaction compared to a flat surface (114). Figure 42a and 42b show the schematic of diagram of FS-TES with pristine PTFE compared to modified PTFE surface. The available contact area for interaction is notably expanded. When these textured surfaces engage with another material, they establish a greater number of contact points, enhancing the potential for interaction compared to a smooth, flat surface. This increased contact area facilitates more efficient charge generation and transfer, ultimately leading to improved performance and energy output in triboelectric nanogenerators. Consequently, the modified PTFE surface was used in all experiments conducted in this study.
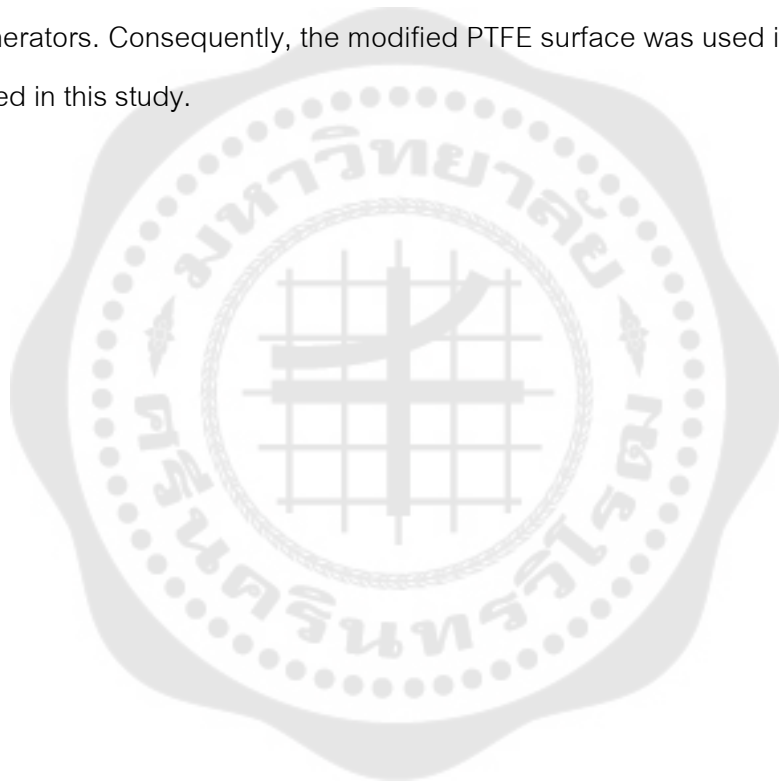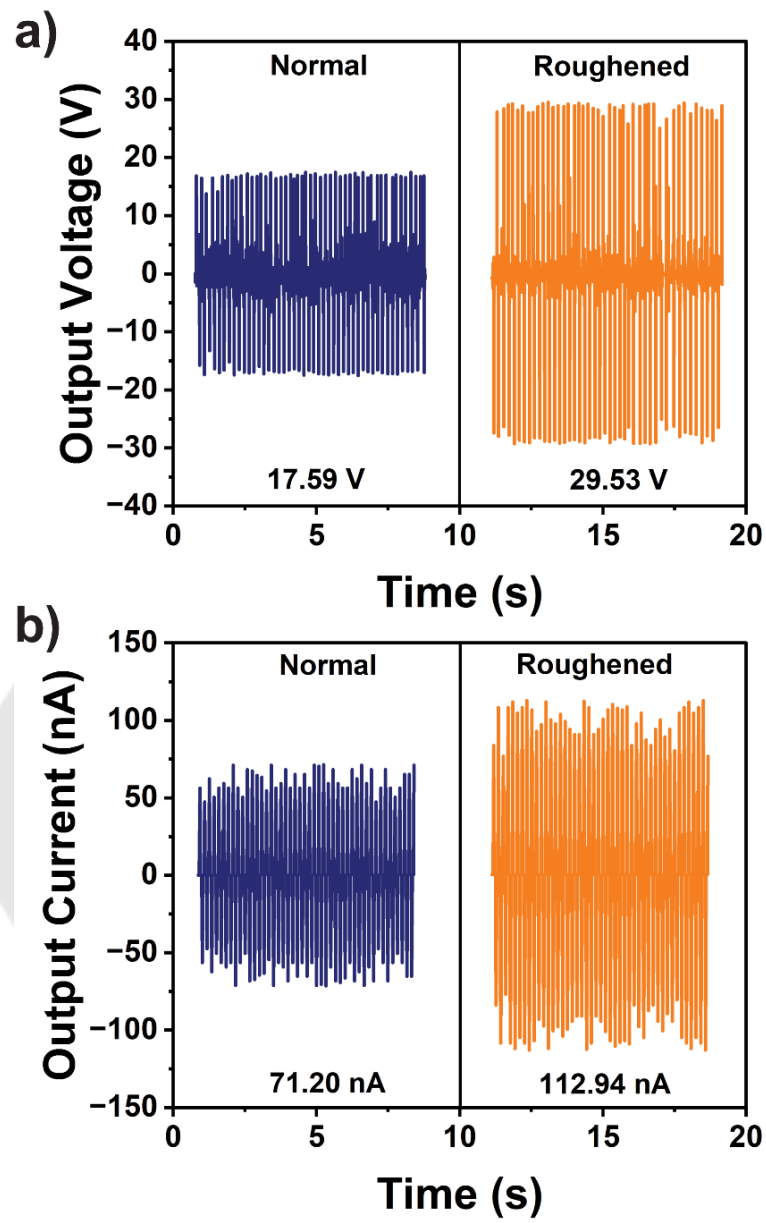
Figure 41 The electrical output a) V_{OC}, and b) I_{SC} of the PTFE before and after surface modification by polishing
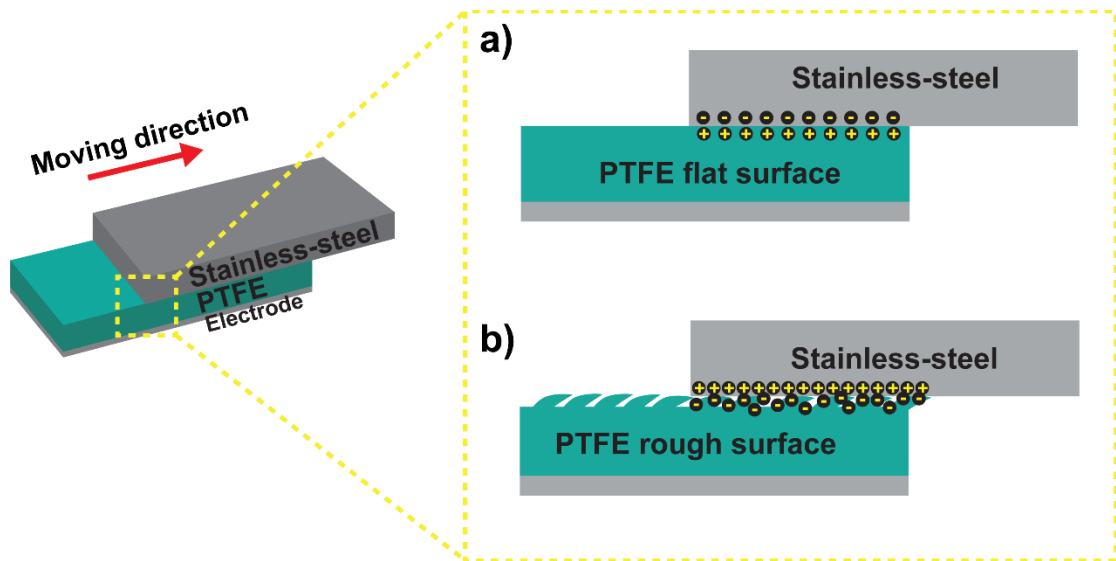
Figure 42 The images of comparing charge generated on the film surface of pristine PTFE and modified PTFE

4.2.2 The Effect of Electrode Distance on Electrical Output for the Regular FS-TES

The regular structure of FS-TES was initially fabricated to determine the key parameters that influence the electrical performance. One of the important parameters is the distance between the two electrodes, which determines the sliding displacement that impacts on power generation. Previous research has shown that the separation distance between the sliding triboelectric surface and the electrodes significantly impacts the output generation capability of a free-standing mode TES (108). This distance affects the charge transfer efficiency and overall output of the TES. Herein, by studying the influence of distance electrode on the TES's performance, the optimal distance that maximizes output performance can be achieved. In order to determine the optimum distance for maximum electrical output, the characteristics of V_{OC} and I_{SC} were studied at various electrode distances of 0, 5, 12, 17 and 35 mm. The electrical output results as a function of electrode distance are shown in Figure 43. According to Figure 43a and 43b, the output signals of V_{OC} and I_{SC} at 0 mm distance are ~8.9 V and ~29.0 nA. When the electrode distance was increased to 5 mm, a significant rise in the output

signal was observed, with V_{OC} reaching ~17.8 V and I_{SC} reaching ~102.5 nA. However, when the electrode distance was increased beyond 5 mm to distances of 12 mm, 17 mm and 35 mm, a significant decrease in electrical signal values was observed. This indicates that exceeding the optimal electrode distance adversely affects the performance, leading to a significant reduction in the V_{OC} and I_{SC}. In the FS-TES, the electrode spacing determines the distance over which the triboelectric charges can transfer between the two surfaces during mechanical motion. When the electrode spacing is too large, the efficiency of charge transfer may decrease due to charge dissipation, leading to a reduction in the output of the device (115).

According to equation (3), by considering ΔQ_{SC} and S as constant, V_{OC} is proportional to C. Typically, dividing the gap between electrodes into smaller segments significantly increases the C, which in turn results in a lower V_{OC} (116). Therefore, in this case, increasing the distance between electrodes can effectively decrease the C value, leading to a higher V_{OC}. Therefore, the output signal demonstrates an increase as the distance between the electrodes extends from 0 mm to 5 mm. However, there is an optimum gap that provides the highest output. Beyond this optimum threshold, the output signal begins to decrease due to the breakdown effect, which is essentially the dissipation of electrostatic energy. The breakdown effect in a FS-TES refers to a phenomenon where the electric field between the electrodes becomes so strong that it causes the surrounding medium (usually air) to become ionized, leading to an unintended discharge or loss of electrostatic energy (117). This breakdown effect, leading to the loss of electrostatic energy in an FS-TES, can be explained by Paschen's Law. Paschen's Law establishes a relationship between the breakdown voltage, the pressure of the gas medium, and the distance between the electrodes. This relationship is crucial for understanding the limitations and behavior of the FS-TES as the electrode gap varies. The law is expressed as (118):

$$V_b = \frac{apd}{ln(pd)} + b \tag{6}$$

where: V_b stands for the breakdown voltage, d is the distance between the electrodes, p represents the pressure of the gas medium, b devotes a constant depending on the gas medium, and a is another constant related to the specific gas. As the electrode distance (d) increases, it can initially increase the output voltage up to an optimal point. Beyond this, if the electric field becomes too strong, it can cause a breakdown. If the voltage across the electrodes approaches the breakdown voltage (V_b), ionization occurs, leading to a conductive path through the medium (air). This causes an unintended discharge, reducing the stored electrostatic energy and thereby decreasing the effective output. When the breakdown effect occurs, the output of the device drops because energy that should be converted to electrical output is lost (118).

The breakdown effect in an FS-TES can be understood in two distinct scenarios: one occurring between the two electrodes, and the other occurring between the triboelectric surfaces and electrode (119). Breakdown between the two electrodes is more common and affects the output than breakdown between the triboelectric surfaces and one of the electrodes. This disparity in impact arises from the significant influence of the gap between the electrodes on the breakdown threshold. As the distance between the electrodes increases, so does the voltage required to produce a discharge spark, known as the breakdown voltage. When the V_{OC} reaches this critical level, it's enough to trigger the formation of a discharge spark. This spark acts as a trigger for the formation of a breakdown channel between the electrodes. Therefore, as the gap widens, the output signal is reduced when the breakdown threshold is exceeded. This underscores the crucial role of electrode spacing in ensuring signal stability and integrity. Similar to the work of W.-Z. Song *et al.* (115), where the influence of electrode spacing on the output of DC-TENG was studied. Therefore, in this study, increasing the distance between the electrodes beyond 5 mm reduces the output signal. As a result, a distance of 5 mm between the electrodes was identified as the optimum distance for this research.
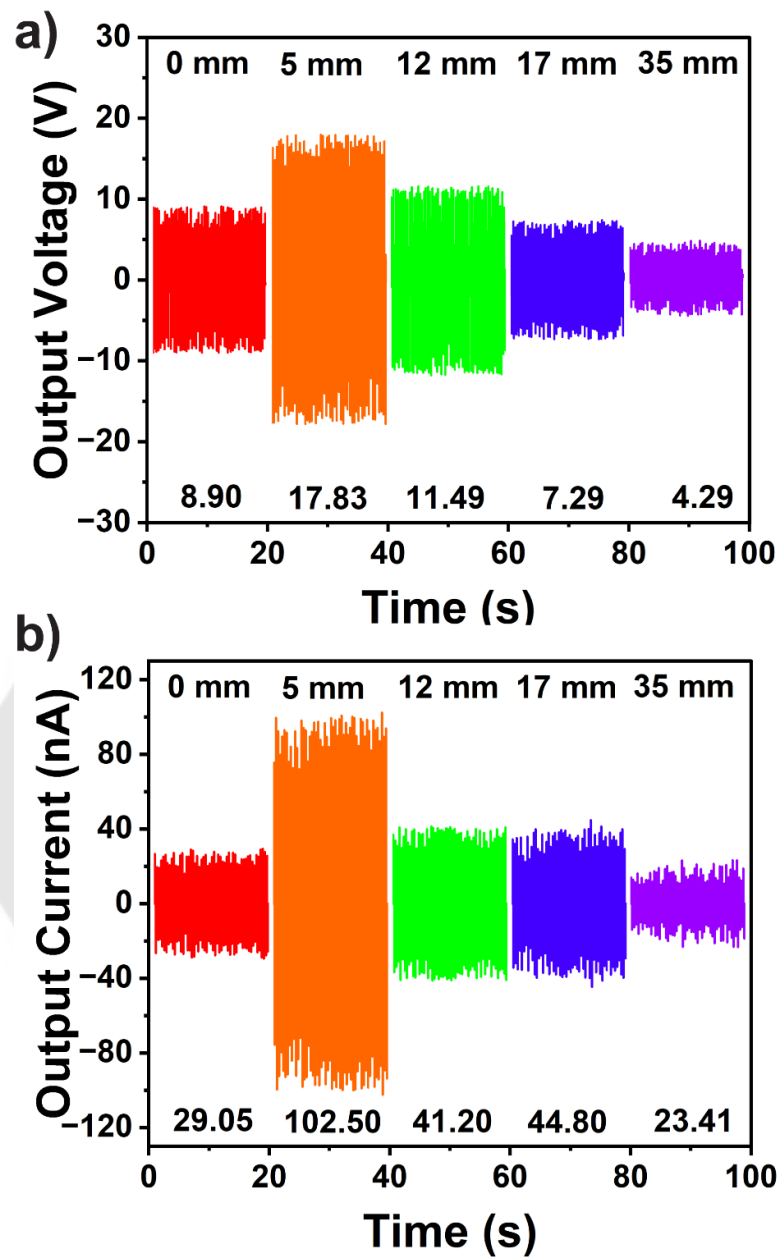
Figure 43 output a) V_{OC} and b) I_{SC} of FS-TES by varying the distance of electrodes

4.2.3 The Effect of Frequency on The Electrical Output of the Regular FS-TES

Considering the goal of this study to develop a wrist-worn sensor for monitoring PD, frequency sensitivity becomes a crucial factor. The frequency of PD's tremor can vary depending on the stage and the verity of the disease. Generally, the typical tremor in PD is reported to be around 3-7 Hz (120). This variability in tremor frequency

necessitates the design of a sensor that is highly sensitive and capable of accurately detecting tremors within this specific frequency range. Understanding and accommodating these frequency variations is essential for creating a reliable and effective monitoring tool that can assist in the management and treatment of PD. Therefore, frequency variability has also been considered as it has a direct impact on output generation of FS-TES.

Output measurements were systematically conducted across a range of frequencies, spanning from 3 to 7 Hz. The FS-TES device, featuring an electrode distance of 5 mm, underwent representative testing. To investigate the effect of frequency on the electrical output produced by the FS-TES, the author used a sliding testing machine. This specialized equipment allows precise manipulation of the experimental frequency by adjusting the motor speed. By controlling the speed of the motor, we were able to systematically change the frequency and observe its effect on the electrical output characteristics of the FS-TES. This method allowed detailed analyses to be carried out, providing valuable insights into how different frequencies affect the performance of the sensor and its ability to generate output. Figures 44a and 44b show output signals of V_{OC} and I_{SC} with various frequency. When the output signal was measured at 3 Hz, ~8.64 V and ~26.29 nA were generated. As the frequency is increased from 3 to 7 Hz, the output signal increases progressively, reaching a maximum V_{OC} and I_{SC} of approximately ~25.35 V and ~149.30 nA respectively at 7 Hz. It is evident that the output signals of both V_{OC} and I_{SC} are directly proportional to the increasing frequency. At lower frequency, the mechanical motion between the triboelectric materials is slower and less intense at lower frequencies. This reduced motion results in weaker frictional forces leads to slower transfer of the generated charges to the external load. At higher frequencies, the duration of each working cycle is shortened, and the number of cycles within a given period increases due to the more rapid and intense mechanical motion between the stainless steel and PTFE films. This increased motion leads to greater frictional forces and more frequent contact and separation between the materials, enhancing the generation of triboelectric charges. The increased charge density means

that more charges are available for transfer, and the high-speed sliding allows for quicker transfer of these charges to the external load, resulting in higher output voltage and current (121-124). As a result, there is an overall increase in total output. This demonstrates that the device can operate at various frequencies, with the output being directly related to the frequency.
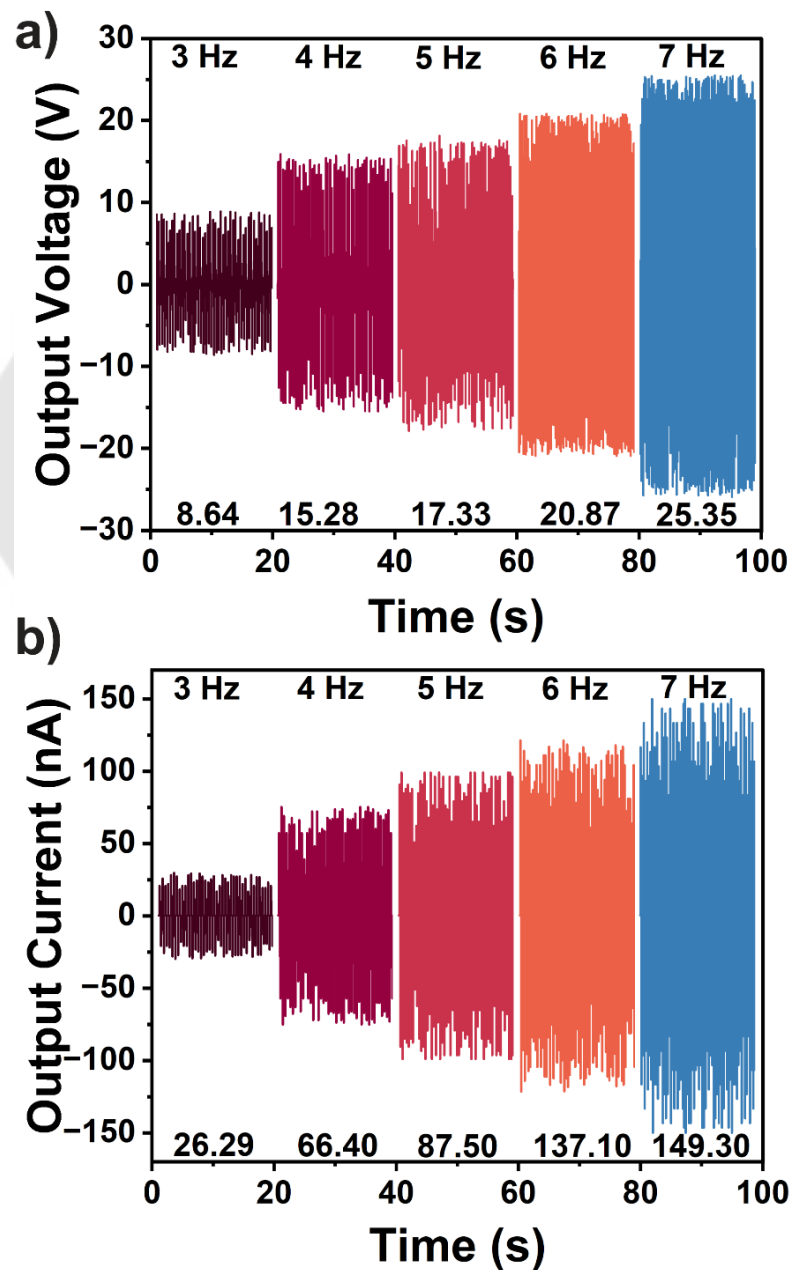
Figure 44 Electrical output a) V_{OC} and b) I_{SC} of FS-TES by varying frequency

4.3 Design and Fabrication of the WW-TES Device

In this study, the objective is to develop a sensor that is both efficient and accurate enough to effectively monitor PD tremor, while also being comfortable and easy to use for daily wear. This is especially important for elderly patients who require a user-friendly device that integrates seamlessly into their everyday lives. Inspired by familiar automatic wristwatches, the sensor is designed to be non-intrusive and minimize discomfort. In addition, automatic wristwatches were renowned for their reliability and longevity, working as long as the wearer remained active. They were able to harvest energy from the irregular and chaotic movements of the wrist (125), making them an ideal model for this application. An automatic watch movement is equipped with a freely rotating metal weight known as an oscillating plate. The movement of the wearer's wrist causes the oscillating plate to rotate. As it rotates, it automatically winds the inner mainspring, which powers the watch (81, 82). The rhythmic rotation of the oscillating plate following the movement of the wrist might allow the triboelectric pair materials to come into contact and separate. Therefore, this work focused on using an oscillating plate to develop a novel WW-TES device.

The device was designed to resemble a circular watch using the Shapr3D App (Version 5.572.6640.0) to precisely create the shape and size of the frame along with all necessary components, such as holes and substrates for material pair attachment. The 3D model files were then imported into the ideamaker software (ideaMaker 4.3.2 Raise3D E2) to slice the model and generate the gcode files. Subsequently, the frame was 3D printed using PLA filament on a Raise3D printer (Fused Deposition Modeling printer; FDM) with a resolution of 0.2 mm. The printing was carried out at a temperature of 210 °C and a speed of 60 mm/s.

4.3.1 The First-Generation of the WW-TES Design

Figure 45a illustrates the material components of the first generation of WW-TES device. Initially, the research goal was to confirm that the contact between oscillating plate and negative material layer can produce electrical signal by taking

triboelectrification and electrostatic induction mechanism. The device was constructed with simple structure. The Kapton tape was assembled into a sphere plate to hold the oscillating plate, meanwhile a material pair was set inside the plastic frame. The device structure and components are shown in Figure 45b. The testing process was conducted by rotating the oscillating plate while simultaneous measuring the output signal by oscilloscope. As can be seen in Figure 45c, the result of the obtained electrical output signal was unclear. The characteristic peak of signal is similar to the output from electrical conductor rather than indicating a triboelectrification signal from the contact of two materials. Consequently, further experimentation and redesign was necessary to create a more stable and robust frame.
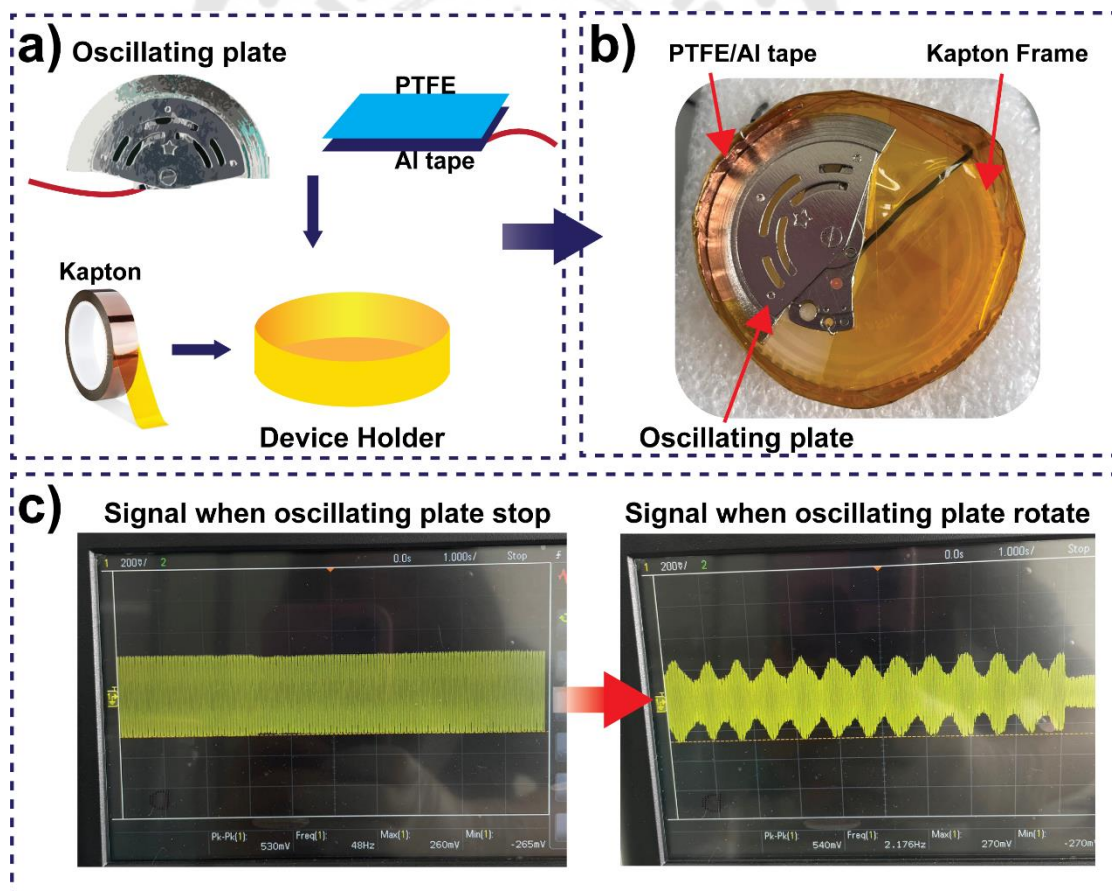
Figure 45 The first-generation of WW-TES design

4.3.2 The Second-Generation of the WW-TES Design

The second generation of the design is shown in Figure 46. Figure 46a illustrates the first design of the WW-TES. The device features a circular frame with a diameter of 34 mm, a height of 7 mm, and a wall thickness of 3.5 mm. At the center of the device, a platform measuring 20 mm $\times$ 5 mm is constructed to hold the oscillating plate. The platform is designed with a central hole to accommodate electrode placement, enabling wires to extend outward without any obstruction. This design feature is intended to connect the electrode to the oscillating plate, incorporating a brush electrode commonly found in motor designs. The wires are carefully routed through the bottom of the device frame to prevent any interference with the rotation of the oscillating plate. On the other hand, another electrode was fabricated composed of PTFE, which is connected to Al tape that attached to electrical wires. Figure 46b displays the schematic diagram and digital images of WW-TES that are fully assembled device with all components installed. And finally, the device tested the electrical output signal. To test the electrical signal, the device was shaken to apply mechanical force. This caused the oscillating plate to rotate and contact the PTFE electrode, aiming to generate an electrical signal from their interaction. However, the experimental results showed no detectable electrical signal. The generated signal was indistinguishable from the baseline noise as shown in 46c, indicating that the intended interaction did not produce a measurable electrical output. Therefore, further design and optimization are required to determine if it's feasible to generate an electrical signal using this configuration of materials in a WW-TES device.
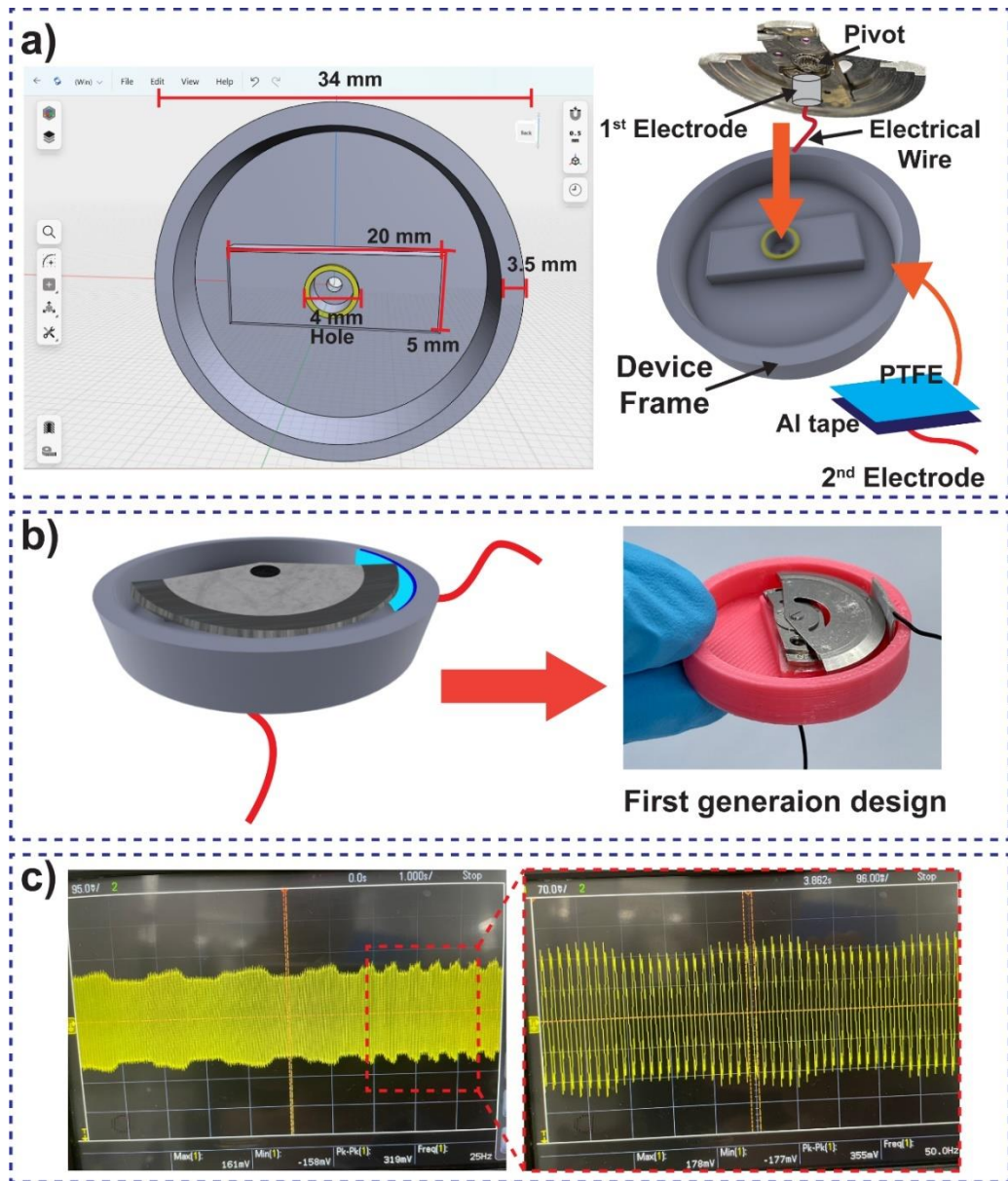
Figure 46 The design of the second-generation WW-TES

Following the initial first-generation design, several improvements were made to enhance the device. While the fundamental characteristics of the device remain consistent with the original design, key adjustments were implemented to optimize its performance and suitability as shown in Figure 47. These modifications have refined the basic elements to develop a device that is more efficient and user-friendly.
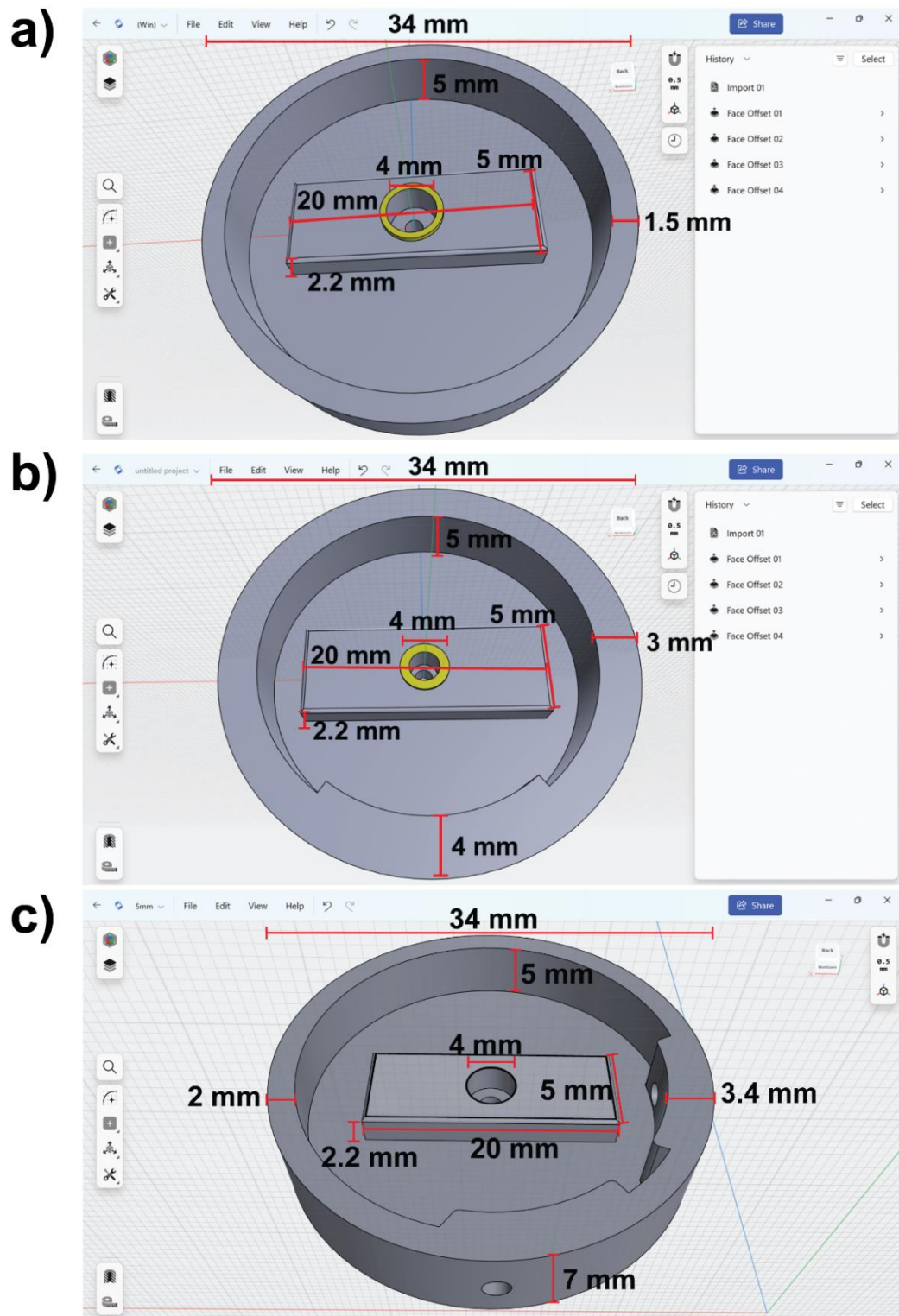
Figure 47 The design of WW-TES frame device a) second b) third and c) forth design

4.3.3 The Third Generation of WE-TES Design

According to Figure 48, the third-generation design of this device can be divided into 3 types. The 1st type was circular with a central platform for attaching the oscillating plate. However, this design was not successful because, when the tribomaterial pairs were attached to the inside of the frame, the distance between the contact materials was not appropriate as shown in Figure 48a. This caused the oscillating plate to rotate without making contact with the tribomaterial pairs. Therefore, the design was revised, resulting in the creation of the second design as shown in Figure 48b. The 2nd type included an inward extension platform for attaching the contact material inside. However, it had only one fixed position. In addition, the size of the platform may have been incorrectly measured, resulting in the oscillating plate getting stuck with the inward extending platform. Despite these changes, the design was still unsuccessful. As the device being designed relied on the free-standing triboelectric sensor mechanism, which required the installation of two electrodes, a new 3rd type was designed as shown in Figure 48c. The final design resulted in a device with a diameter of 33 mm, a height of 7 mm, and a side wall thickness of 2 mm. The inner wall featured a platform for attaching materials at two contact points, and a central platform for attaching the metal oscillating plate. The frame featured a platform in the center and two inward extensions for placement of the oscillating plate and PTFE. Once the third design is finalized and deemed acceptable, it is used as a prototype to create the subsequent device frame.

In this prototype, the distance between the electrodes is further adjusted for achieving the highest amplitude of electrical output. Since the operation of this device relies on a mechanism of contact and separation of materials to produce an electrical signal. This experiment was therefore devised to find the optimum conditions for the proper distance between the electrodes to produce and transport the most electrical charges in time and achieve the highest electrical signal value. The illustration of device frame with various electrode distances is displayed in Figure 48d, showcasing spacings of 0, 5, 12, 17, and 35 mm. The consideration of varying these distance values was decided based on the size of the device frame and the position of electrodes in contact

with oscillating plate. The distance adjustments started at 0 mm, which means there is no distance between two electrodes, and then progressively increased to 5 mm, 12 mm, 17 mm and maximum 35 mm. As depicted in Figure 48d, the electrodes are positioned in opposite way to each other at the maximum distance of 35 mm. Distance Larger than 35 mm was not designed because they will come up with the same spacing of electrodes as 17 mm. Meanwhile, the distance at lower than 5 mm was also not designed because the distance of 5 mm is still too short. The signal amplitude at narrower electrode's distance, for example, 2 or 3 mm, is probably not significantly different. Figure 48e shows the assembled frame devices attached to a tribomaterial to form a complete sensor system. It can be seen from the images that the oscillating plate and PTFE films are firmly affixed to the PLA frame and prepared for testing their electrical output characteristics.
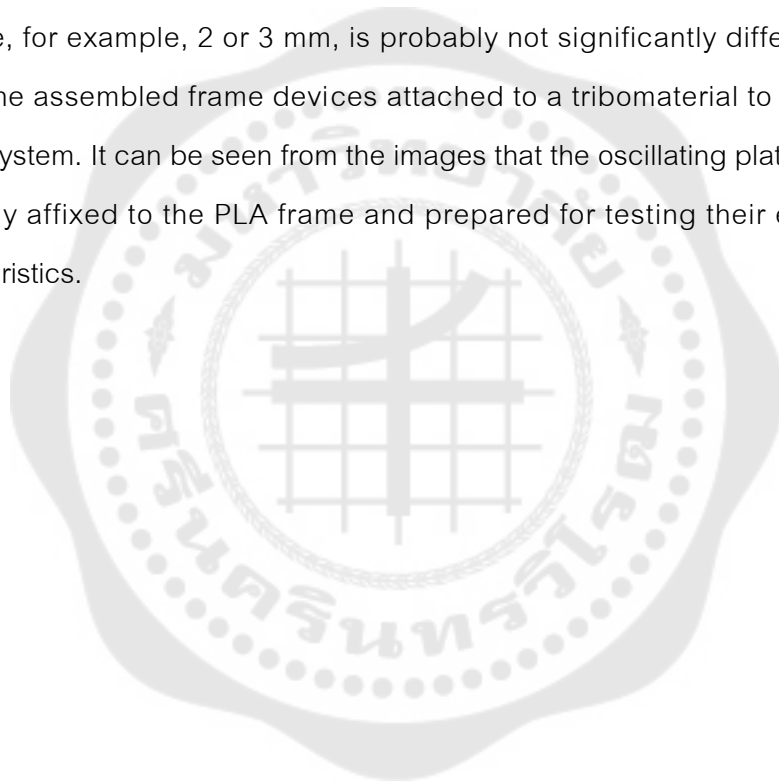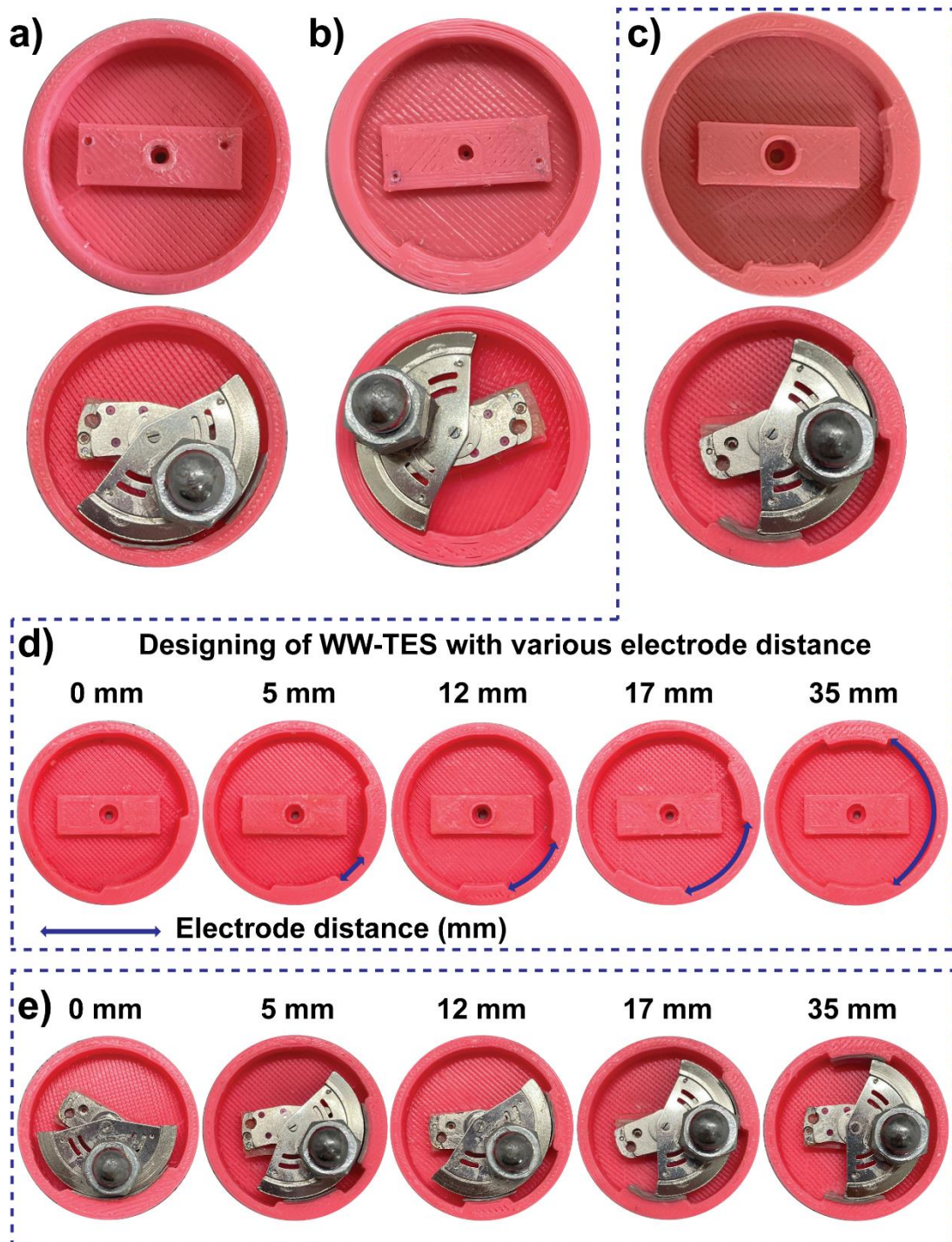
Figure 48 The design for device frame a) The 1st type, b) The 2nd type and c) The 3rd type (Final), d) The device frame with various electrode distances of 0, 5, 12, 17 and 35 mm and e) Frame devices are attached to a tribomaterial and are assembled to form a sensor.

4.4 Proposed Working Mechanism of the WW-TES

According to the structure of the WW-TES, there is an oscillating plate made of stainless steel, which serves as the tribo-positive material. An oscillating plate is attached at the center of the frame with a nut and bolt, acting as the proof mass for smooth rotation. The contact area of the oscillating plate is 40.0 mm diameter x 1.2 mm thickness = 48 mm^2. The two PTFE films used as the tribo-negative material were cut into 10.0 mm × 5.0 mm, which equal to the 50 mm^2 surface area, and attached to the same size of Al electrodes (10.0 mm × 5.0 mm). These sets of PTFE/Al electrodes were positioned within the frame and connected to electrical wires. Each electric wire was then passed outward to the load through a drilled hole. Figure 49a-c illustrates the structural components and the 3 main steps of a stainless-steel oscillating plate movement inside the WW-TES which include the starting of rotation, intermediate rotation and finally the complete cycle. Based on the cross-sectional area of PTFE and the oscillating plate, the total effective contact area, when the rotating material comes into contact with PTFE, is 1.2 mm thickness of oscillating plate x 10 mm PTFE wide = 12 mm².
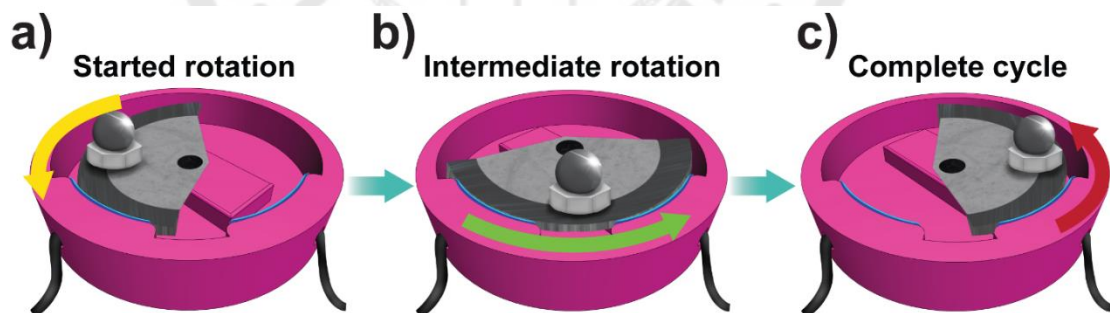
Figure 49 Working mechanism of WW-TES device during a) The starting rotation, b) Intermediate rotation and c) Complete cycle.

The output generation mechanism of the WW-TES device could be described according to Figure 50 by extracting from the real V_{OC} signal. This rotation was recorded in slow motion by a digital camera to match the observed electrical signal with the

mechanism of AC electricity generation. When the rotation of the oscillating plate was observed during operation, it was found that it rotated in an anti-clockwise direction. Figure 50 illustrates the specific working principle of the WW-TES device, highlighting how the oscillating plate undergoes rotation when exposed to an external force. We define the state when the oscillating plate swings and contacts PTFE film as the first state (i). At this state, due to their distinct electron-donating and -receiving properties, metals typically tend to donate electrons, resulting in a positive charge on their surfaces. Conversely, PTFE sheets tend to attract electrons, leading to a negative charge on their surfaces. Since an Al tape is attached to the PTFE film, it undergoes induction from electrical neutrality to positive charges on the electrode. This induces a flow of electrons, causing them to move from the left-hand electrode (LE) to the right-hand electrode (RE). The oscillating plate continues to move, maintaining constant contact with the PTFE and undergoing continuous charge transfer. The induced current is small, resulting in a signal where $I < 0$, until the maximum peak output on the negative side is obtained for $I << 0$, at state (ii). The current flow continues until equilibrium is reached, which occurs when the oscillating plate makes full overlap with the PTFE at state (iii). This induces an equal number of charges, causing no current to flow ($I \approx 0$). During state (iv), the oscillating plate reaches some part of the RE. Inducing electron transfer between the oscillating plate and the PTFE leads to the development of a negative charge on the PTFE's surface. Consequently, the electrons accumulated on the RE now flow backwards towards the LE, creating the opposite direction with $I > 0$ of signal to give an alternative (AC) current. As the oscillating plate rotates further to RE, the flow of electric current continues continuously until it reaches its maximum peak in the positive side at the state (v). The I at this state is supposed to be $I >> 0$. As the oscillating plate continues to rotate, it reaches a point where it passes completely over both PTFE films in state (vi). At this stage there is no current flowing ($I \approx 0$). The oscillating plate continues its rotation, and during stages vii through ix, no electric current is produced. As the oscillating plate moves away from both the LE and RE, the induced charge gradually diminishes as the oscillating plate rotates further away from both LE and RE which is considered the end of

the cycle. The I during state (vii) to (ix) is expected to be I≈0. The charge exchange between the oscillating plate and the PTFE occurs again when the oscillating plate returns to the initial state. This repetition of the initial step results in another exchange of charges, leading to the continuous generation of an electrical signal as previously described.
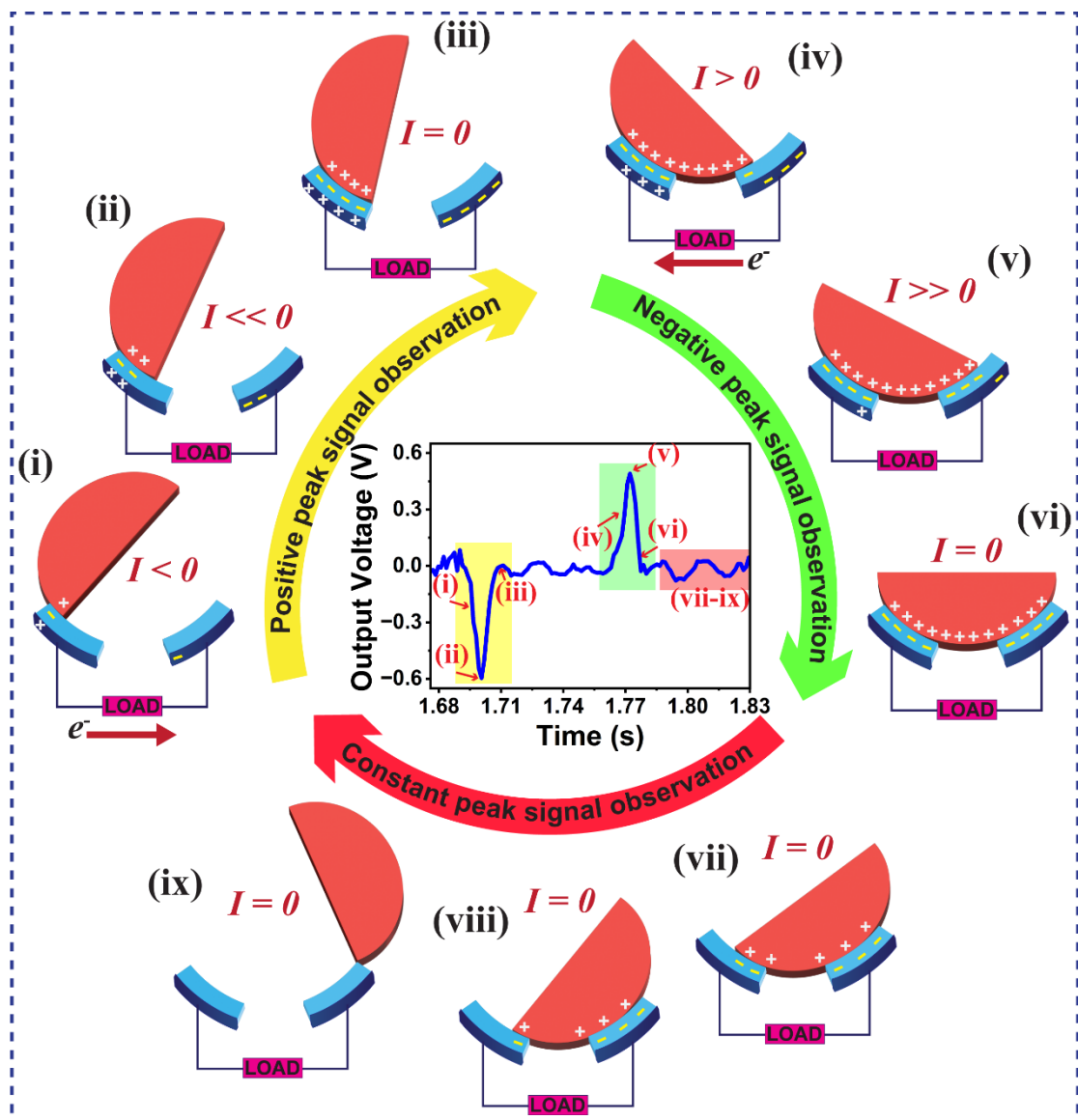
Figure 50 Working principle of WW-TES device

4.5 The Electrical Output Performance of WW-TES Device

4.5.1 The Effect of Electrode Distance on Electrical Output Of WW-TES Device

From an investigation into the optimum distance between the electrodes during the regular FS-TES test procedure, it was found that a distance of 5 mm gave the best electrical signal transmission. To confirm this finding, the WW-TES was assembled with the distance electrodes set at 0, 5, 12, 17 and 35 mm. An additional round of testing was then carried out to confirm the optimum distance electrode consistently produced the highest quality electrical signal. To validate the WW-TES device, the output signals including V_{OC} and I_{SC} were studied by using orbital shaker as a vibration generator to excite the device. The electrodes distance was investigated by adjusting the distance between electrodes during the assembly of the device and observing the corresponding electrical output signal. According to Figure 51a and 51b, the results show that the electrical output signal follows a similar trend to those observed in the basic FS-TES. At 5 mm, the device can provide the highest electrical output signal of both V_{OC} and I_{SC} about ~0.61 V and ~3.5 nA. The electrical output of the WW-TES is lower compared to the regular FS-TES due to differences in the contact area sizes between the two devices. This difference arises from the fact that, during the assembly of the WW-TES device, the sizes of the electrodes and the PTFE film were reduced to accommodate the overall dimensions of the device. Despite this reduction in contact area, the electrical signal values of the WW-TES followed a similar trend to those of the regular FS-TES. This result is truly evident that electrodes distance at 5 mm was the suitable parameter for constructing WW-TES device in this work.
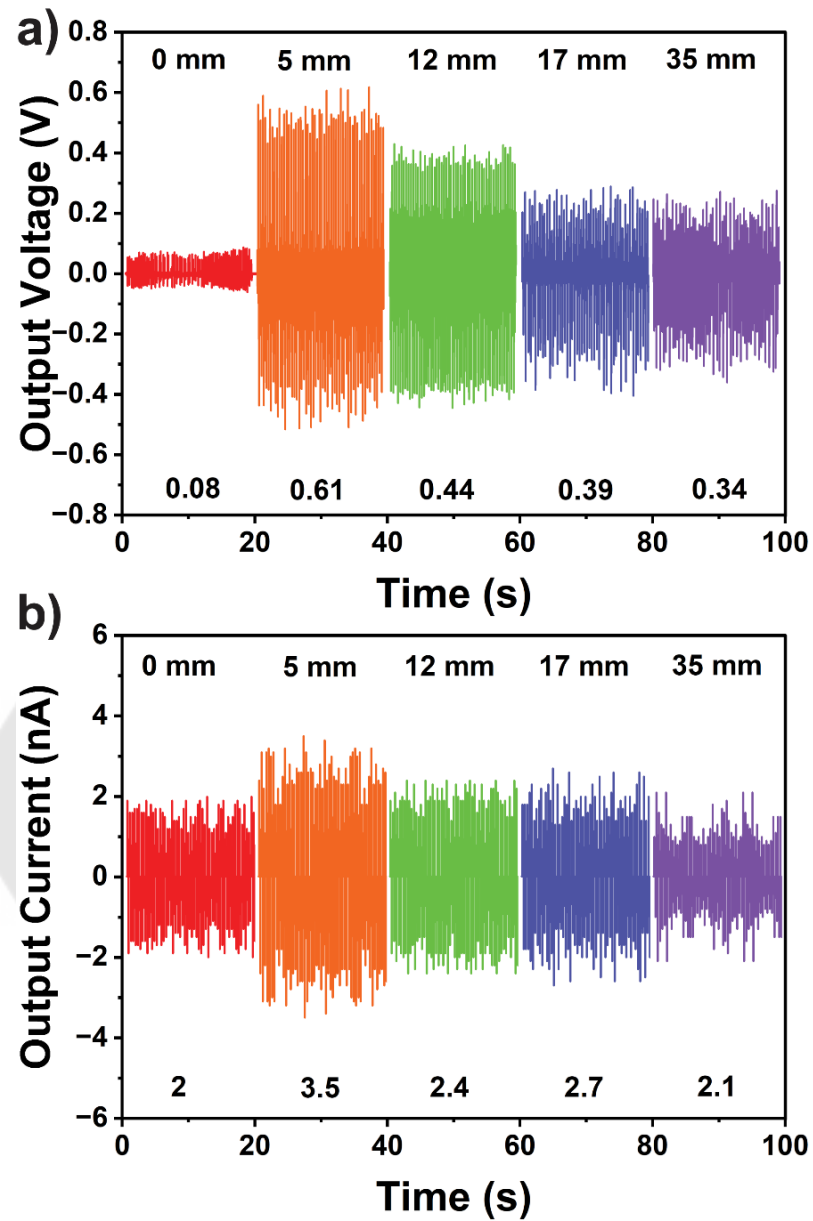
Figure 51 The electrical output V_{OC} a) and I_{SC} b) of WW-TES device by varying the distance of electrodes from 0, 5, 12, 17 and 35 mm.

4.5.2 The Effect of Frequency on Electrical Output of WW-TES Device

After optimization of electrode distance, the effect of different frequency on output amplitude from WW-TES was determined to predict the ability of device to detect signal at various frequencies effectively. Notable, a direct correlation between the amplitude of the output signal and the frequency is quite well known for normal TES.

Herein, since the high- and low-amplitude characteristics of tremors differ in different PD severity, it is therefore essential to determine the output characteristics of the designed WW-TES to be highly sensitive to the specific frequency range. Such sensitivity ensures that the devices can accurately capture and characterize the tremors, providing valuable data for assessing the progression and severity of PD.

In this work, the WW-TES's efficiency was also studied by measuring various input frequencies corresponding with PD severity by placing the device on the vibration shaker that can control the frequency range from 3 to 7 Hz. The signal results are illustrated in Figures 52a and 52b. At 3 Hz, the WW-TES generated the V_{OC} and I_{SC} of ~0.25 V and ~2.0 nA. Then, the output signal of V_{OC} and I_{SC} produced by the WW-TES demonstrated a proportional increase with the increasing input frequency until reaching maximum value at 7 Hz. This result indicates that our design WW-TES device contains capability to generate output signal at various frequencies and was sensitive enough to respond even low frequency of 3 Hz.

By connecting the relationship between frequency detection and severity of disease symptom, the characteristics of PD tremors have been separated into 3 stages of the rest tremor, postural tremor, and kinetic tremor. All detected peaks within the ~3 Hz range are associated with both resting tremors. Resting tremors typically manifest when there is no voluntary muscle activity, occurring when the muscles are at rest. In contrast, postural tremors are specifically found within the 4-6 Hz frequency range, which are evident when maintaining a posture against gravity, such as holding the head, arms, or legs steady. Furthermore, kinetic tremors, which occur during voluntary movement, predominantly fall within the 7-12 Hz range, though they can sometimes be detected at frequencies higher than 12 Hz. These frequency distinctions are critical for the precise detection and monitoring of the various tremor types associated with PD (126). Therefore, it can be claimed that the designed WW-TES in this work is able to detect the mechanical vibration energy at different frequencies, corresponding to different levels of PD tremor. Even though the accelerometer (ACC) sensor developed in previous research can be used to detect PD tremors at 4 to 6 Hz with the signal

amplitude increasing as the frequency increased (127), the ACC equipment was still large and bulky. The WW-TES proposed in this work can be more comfortable used and also provide higher sensitivity to detect signal at even lower frequency at 3 Hz.

5.6.1.1
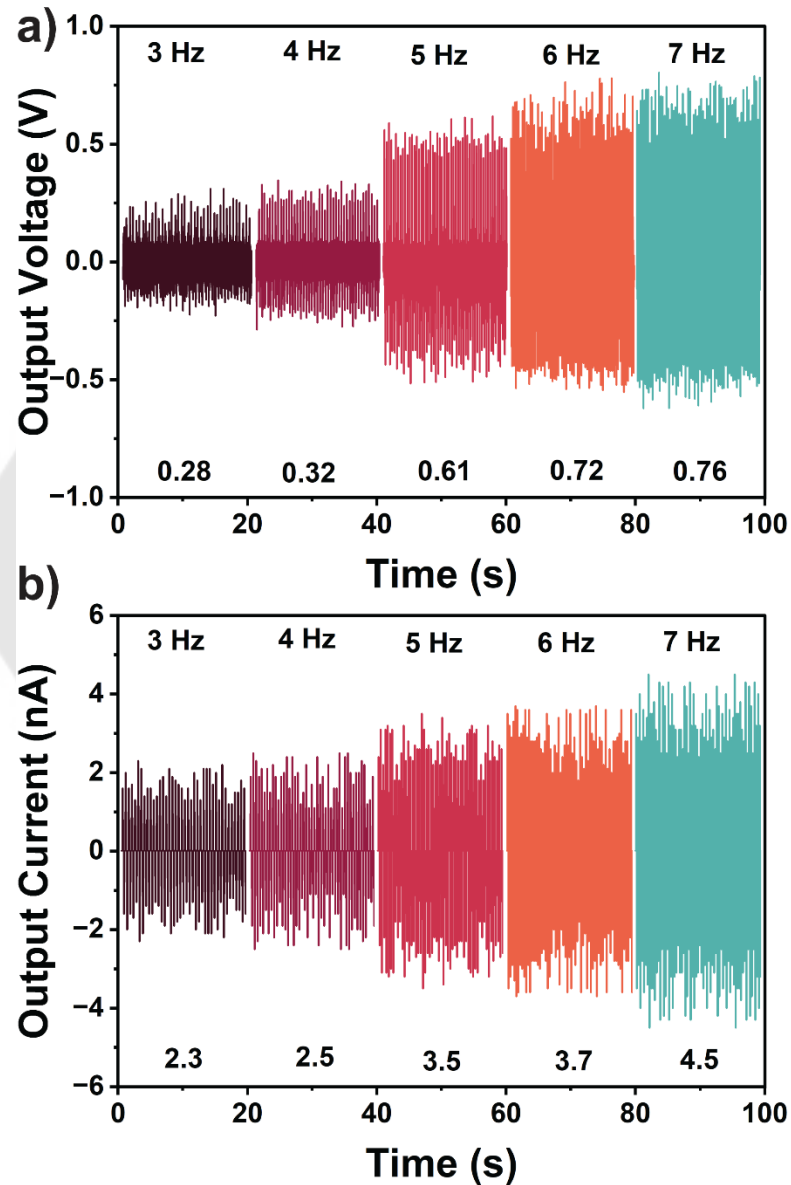
Figure 52 The electrical output V_{OC} a) and I_{SC} b) of TES device with increasing of the frequency from 3-7 Hz.

4.5.3 The Stability Test of WW-TES Device

In addition to the ability to detect mechanical vibration at low frequency, the stability of constant signal providing is also crucial. Ensuring the stability of a WW-TES device is essential for its long-term functionality and accuracy in detecting mechanical stimuli for delivering consistent and reliable performance over extended periods. Figure 53a shows the output signal of WW-TES stability's testing at different frequency from 3, 5 and 7 Hz. The vibration shaker was turned on and off rhythmically while simultaneously measuring the resulting signal. First, the device vibrated at 3 Hz for 10 seconds, followed by a 10 second pause by stopping the shaker, and then the vibration was resumed. This cycle was repeated for 10 rounds. During the experiment, it was observed that the device produced output signals when it was vibrating, and stopped producing output signals when it was not vibrating. In the absence of any shaking, the signal maintains at almost zero, indicating that the electrical value is low attending the baseline. Upon applying mechanical vibration, the device can generate an electrical signal over baseline. At a frequency of 3 Hz, the electrical signal of approximately ~1.0 V was observed and remained consistent at this level over 10 cycles of operation. This trend persisted as the frequency increased. At 5 Hz and 7 Hz, the signal amplitude rose to around ~1.5 V, and ~2.0 V. In the presence of vibrations, the signal magnitude escalates proportionally with the vibration frequency and sustains this behavior throughout all 10 cycles. The consistent and repeatable behavior of the device in responding to vibrations at different frequencies, along with its stability over multiple cycles, suggests that the device is indeed stable in its operation.

Additionally, the long-term operating stability's testing was observed by allowing the WW-TES device to operate continuously for 4000 cycles with simultaneously measuring electrical output signal. It can be seen in Figure 53b that at 7 Hz, the device can maintain a stable electrical output signal at ~2 V along 4000 cycles of continued operation. Therefore, it can be concluded that the designed WW-TES confirms the capability to withstand several cycles of operation without potentially degrading its

performance over time in addition with consistently maintained a stable electrical output throughout the experiment.
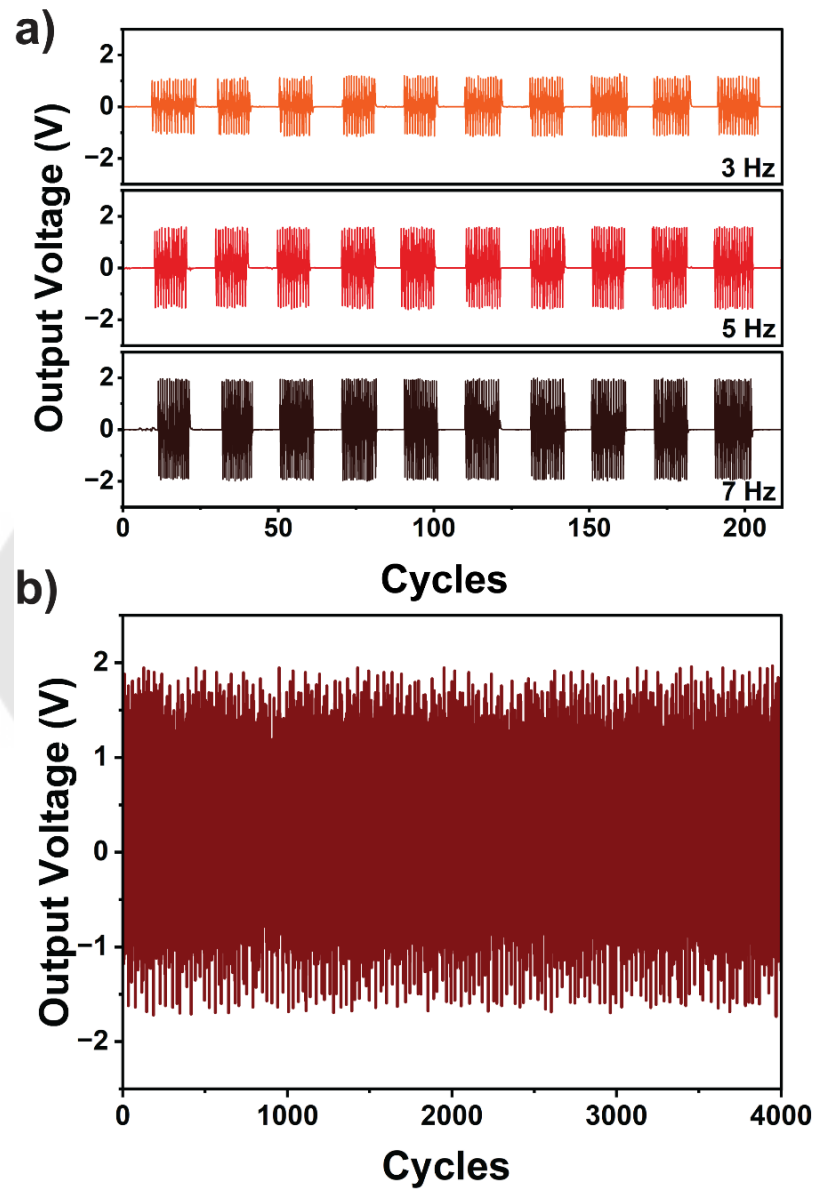
Figure 53 a) The cycles of output signal stability, b) The stability continues at 7 Hz for 4000 seconds.

4.5.4 The Effect of Humidity on the Output Performance of WW-TES Device

Another parameter that is also important for PD sensor application is stability as a function of environment that encompasses the sensor's ability to withstand various environmental conditions without decreasing output performance or degradation. Environmental factors, especially humidity, can significantly affect the dropped performance of TES. According to the TES working mechanism that is based on the coupling of triboelectrification and electrostatic induction, high humidity can cause a layer of water to form on the surface of the triboelectric materials. The higher charged conductivity normally related to humid air will increase the leakage of charges and significantly further reduce the output performance of the TES.

Studying the effect of humidity on the electrical signals of WW-TES is also crucial in the case of WW-TES devices that are aimed at being used in everyday life. They will encounter various atmospheric conditions affecting their electrical signals. Basically, the presence of moisture (water molecules; H_2O) at the material's surface is most often related to the humidity level. Herein, the influence of humidity on the output voltage of the WW-TES was thoroughly investigated. The experiments were carried out at room temperature in ambient air by fixing frequency of 5 Hz, and for a wide range of relative humidity (%RH) from 21 to 81%RH. The device was continuously operated by placing it on the top of orbital shaker and covering it with the humidity control unit. The operation was undergoing at varying humidity levels, ranging from low to high. The experimental set-up can be seen in Figure 54. The initial humidity condition was approximately 21% and was then increased in 10% increments by simultaneously recording the electrical output at each step of operation. This process continued until the humidity reached 81%. This systematic approach allowed a detailed analysis of how different humidity levels affected the performance of the WW-TES, providing insight into its behavior over a range of environmental conditions.
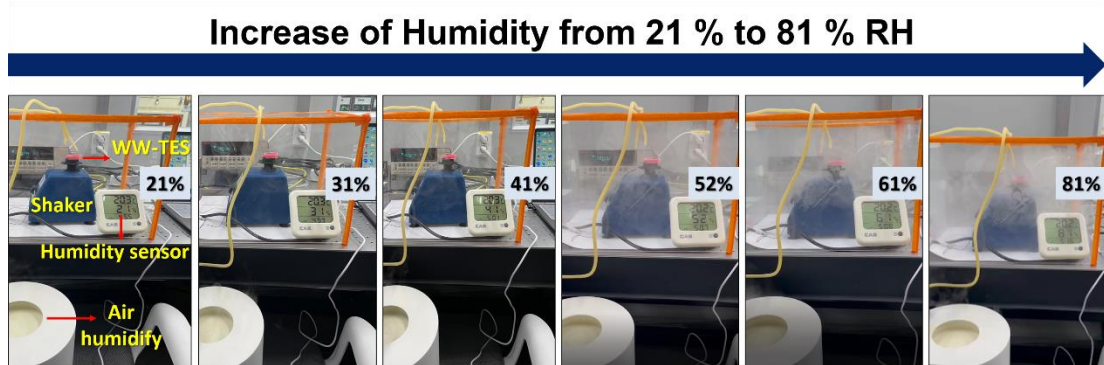
Figure 54 The humidity setup

Figure 55 shows the results of the WW-TES to detect humidity changes in the humidity conditions. The WW-TES displayed noticeable AC voltage variations as humidity levels changed from 21% to 81% RH, with a significant decrease in output voltage. The relationship between output voltage and rising humidity levels is shown. It can be seen that at a humidity level of 21% RH, the output voltage was ~1.0 V. When the humidity increased from 21% to 81% RH, a significant decrease in output voltage to ~0.2 V was observed, reducing by around 5 times. It can be evident that external factors, especially moisture in the air, can significantly affect its electrical output. As mentioned above, in high humidity environment, moisture can form a conductive layer on the surface of the triboelectric material. This conductive layer facilitates charge dissipation, which can interfere with the sensor's ability to generate accurate signals.

Figure 56 displays the working mechanism of the effect of humidity on the output voltage of WW-TES. The absorption of water molecules can be understood in two stages: (1) the chemisorption of the initial H_2O layer and (2) the physisorption of the subsequent H_2O layers. The electric field produced by triboelectrification and electrostatic induction can cause protons (H^+) to hop among the surface-absorbed H_2O molecules, leading to the formation of hydroxide (OH^-) and hydronium (H_3O^+) ions (128). In the initial stage, chemisorption occurs as a small quantity of water molecules forms the initial layer on the triboelectric material surface at low relative humidity. The water molecules chemisorbed onto the surface of triboelectric materials and then undergoes

dissociation into cations H^+ and anions OH^- (73) ($H_2O \rightarrow H^+ + OH^-$). As the relative humidity (RH) level increases further, additional water molecules are physically adsorbed onto the surface of the initial chemisorbed H_2O layer. This physical adsorption process is responsible for the significant drop in the voltage of the WW-TES observed between 21% and 81% RH. During this process, the initial chemisorbed layer is followed by successive layers of adsorbed water molecules, leading to a decrease in the device's voltage output (129). Furthermore, the physically adsorbed layers of H_2O play a role in the dissociation and formation of H_3O^+. In this process, the H_3O^+ group transfers a proton to an adjacent H_2O molecule, resulting in the formation of another H_3O^+ ($H_2O + H_2O \rightarrow OH + H_3O^+$) (130). As humidity levels increase, ions are generated, and they traverse energy barriers between the physiosorbed layers, facilitating proton hopping among adjacent absorbed water molecules. This phenomenon enhances conductivity by enabling the movement of protons through the material. This conduction mechanism is consistent with the well-known proton hopping mechanism of Grotthuss (128). It is shown that the WW-TES should be operated and worked without high humidity or even not further kept in a high humidity environment.
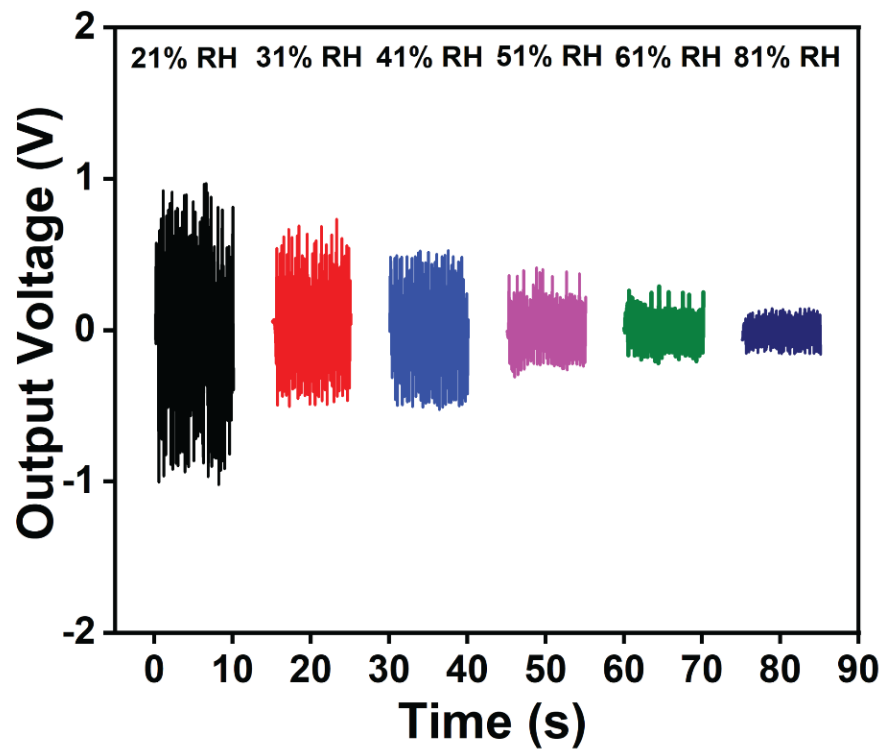
Figure 55 The output voltage of WW-TES and the inset digital picture of the humidity setup and the operation of WW-TES
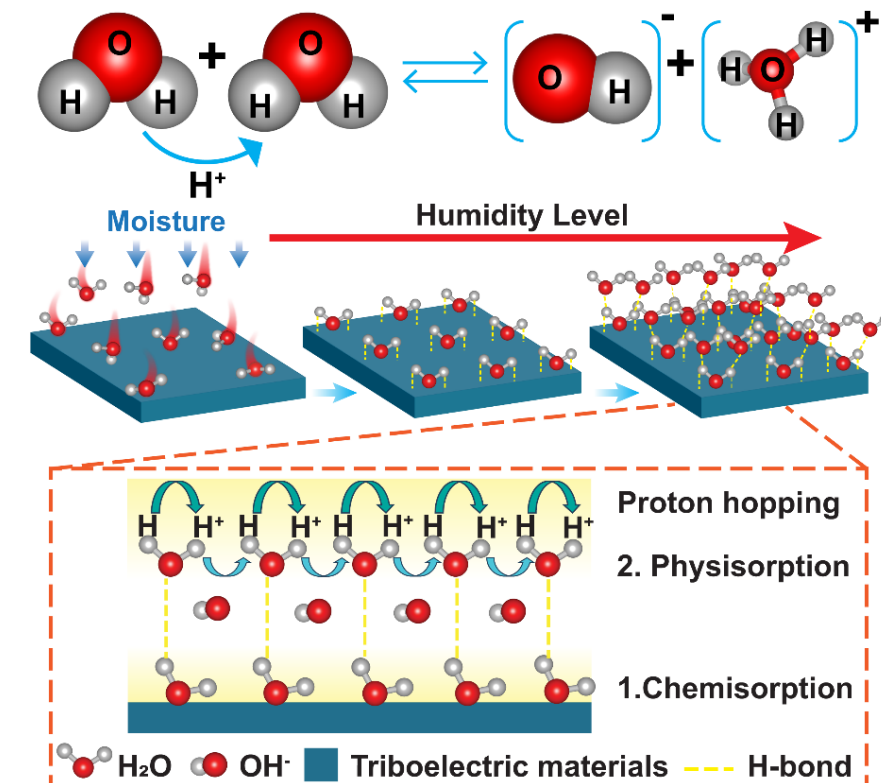
Figure 56 The mechanism of the humidity effect on WW-TES

4.6 Practical Application Test

Tremors are a key symptom in patients with Parkinson's Disease (PD) and often reflect the progression and severity of the condition. Currently, PD tremor severity is evaluated using the MDS-UPDRS scale. This scale classifies the disease on a scale from 0 to 4 according to the frequency of the tremors (131, 132). Level 0 indicates no symptoms or normal function. Level 1 is mild, low frequency tremor (0.5-0.9 Hz) with minimal impact on function. These low frequency or low intensity symptoms do not significantly interfere with daily activities. Level 2 is characterized by mild tremor at a frequency of 0.9-1.8 Hz, resulting in moderate functional impairment and a noticeable impact on daily activities. Level 3 describes moderate tremor at a frequency of 1.8-3.4 Hz. This tremor has a significant impact on function, without being completely disabling. Daily activities such as dressing, eating and writing may become difficult. Level 4 represents severe tremor above 3.4Hz, causing symptoms that significantly affect normal

functioning. These very serious symptoms have a profound effect on daily life, resulting in a significant reduction in activities of daily living, a significant loss of independence, and a serious effect on quality of life (131, 133-135). Based on MDS-UPDRS scale, it can be used as a standardized tool used by clinicians and researchers to assess the severity and progression of PD symptoms, helping clinicians track disease progression, monitor treatment effectiveness, and make informed decisions about patient care (136).

In order to check that the WW-TES can be utilized for real PD monitoring, the device is subjected to experimentation by securing it with a strap, enabling it to be worn on the wrist like a watch as shown in Figure 57. This experimentation involves simulating tremors corresponding to different levels of PD severity through activities of daily living (ADLs) (137). The ADL section of the MDS-UPDRS is of particular importance as it assesses the person's ability to carry out essential daily tasks related to personal care, such as bathing, dressing and feeding, pouring liquids, etc. (138). For people with PD, difficulties with these activities can greatly reduce independence and quality of life. Therefore, in order to assess the ability to use utensils, in this study we performed ADL tasks such as eating, pouring water and writing. These tasks offer valuable insights into an individual's overall motor symptoms. For the water pouring activity, the movements including pick up a container, hold it up, pour water into a glass, and then place the container back down were performed. This simulated the process of pouring water from a container into a glass as shown in Figure 57a. Similarly, for the eating activity, specific movements were performed, including lift the spoon, scooping the food upwards, keep holding up the spoon and put it back down. This mimicked the actions involved in eating as shown in Figure 57b. For the writing activity, an experiment was conducted in which the WW-TES device was worn on the wrist and the spiral drawing test was performed. The Spiral Drawing Test is a clinical assessment tool commonly used in the evaluation of PD (139). In this test, individuals are instructed to draw spirals on a piece of paper to assess motor control, hand-eye coordination, and the presence of tremors or other movement abnormalities, which are common symptoms of PD. In this work, the author has drawn a spiral starting from the center of the paper and extending outwards in a

continuous movement until it reaches the edge of the paper as shown in Figure 57c. The vibration frequency was varied based on the MDS-UPDRS scale during writing to observe the resulting electrical signals.
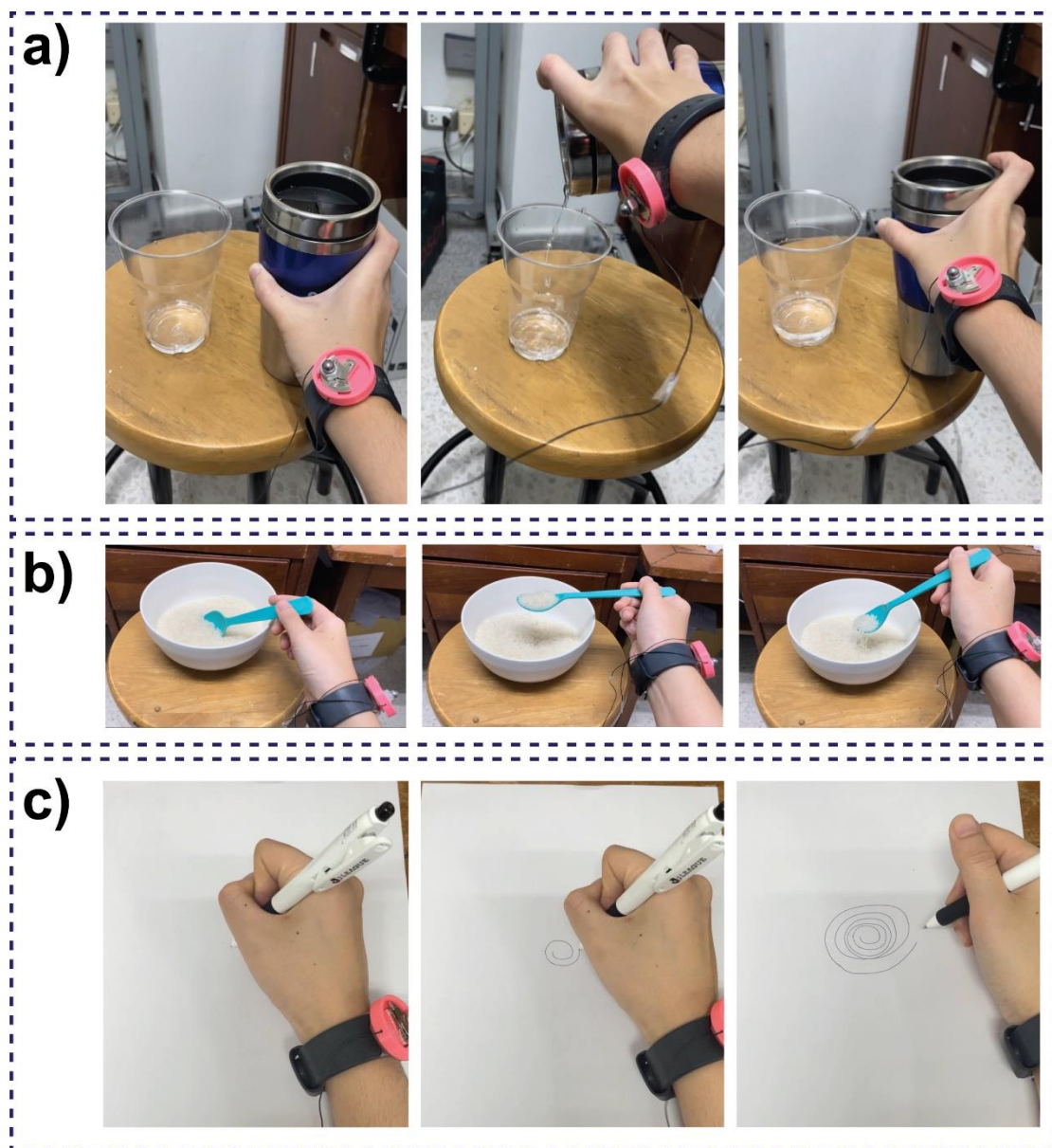
Figure 57 Schematic of activity movement for the experiment, a) Pouring water, b) Eating and c) Writing.

During these activities, the WW-TES device was worn on the wrist. The intensity of tremor was adjusted according to the frequency specified by the MDS-UPDRS scale, which assesses the severity of PD tremor. The output signal presented in Figure 58a (i) shows the output signal for the activity of pouring water, capturing movements of both a normal state (no tremor) and tremor occurrence during the task. In a normal state, the wearer could lift the container and pour water into a glass without any difficulty because there was no hand shaking. Without shaking, there is no mechanical force to cause the oscillating plate within the device to rotate, thus no output signal is generated. However, noticeable peaks appear in the output signal due to wrist movement when picking up the container and pouring water. This hand movement causes the oscillating plate to rotate against the PTFE plate, producing a small electrical peak output. In contrast, when the frequency of the tremor increased, the WW-TES device generated output signals that were directly proportional to the intensity of the tremor frequency. According to Figure 58a (ii-v), two regions of signal amplitude were observed within a single output signal: a higher amplitude region and a lower amplitude region. The higher amplitude region corresponds to picking up and holding the container, while the lower amplitude region corresponds to the wrist turning to pour water into a glass with a shaking hand. In addition, Wavelet Packet Transform (WPT) analysis shows that the color coding in WPT changes patterns according to different signal amplitudes, which correspond to varying tremor severity levels within the MD-UPDRS scale as shown in Figure 58b.

Similar to output signals have been observed from eating experiment. In Figure 59a (i), the normal state is depicted, where no peak output is generated due to the absence of hand tremors. However, some peak outputs appear due to hand movements while scooping rice. These movements cause the oscillating plate to rotate against the PTFE films, generating small peak signals. On the other hand, as the tremor frequency increases, the output signal also increases as can be seen in Figure 59a (ii-v). During eating movements with hand tremors, the output signal displays two distinct regions: a lower amplitude region during spoon lifting and rice scooping, and a higher amplitude region when attempting to hold up the spoonMoreover, WPT analysis of the eating

activity signal also observed changes in color coding patterns according to different signal amplitudes, as shown in Figure 59b. In the writing test section, experimental results show that when writing in a normal state, there is no vibration other than the movement of the wrist (Figure 60(i)). Therefore, there is no electrical signal. However, as the frequency of the vibrations increases, the electrical output also increases in amplitude (Figure 60(ii-v)). The analysis of these activities revealed a clear relationship between frequency and output signal amplitude, where an increase in frequency corresponded with a proportional increase in the output signal amplitude, aligned with the tremor frequency levels 0-4 as defined by the MDS-UPDRS scale. This finding highlights the capability of the WW-TES device to accurately detect the severity of PD and track its progression. The variation in electrical signals serves as a reliable indicator of disease severity, with more intense tremors generating higher electrical output signals. This innovative approach has significant potential to shift the management of PD from traditional treatment to the development of personalized treatment strategies, ultimately leading to better patient outcomes and more effective disease management.
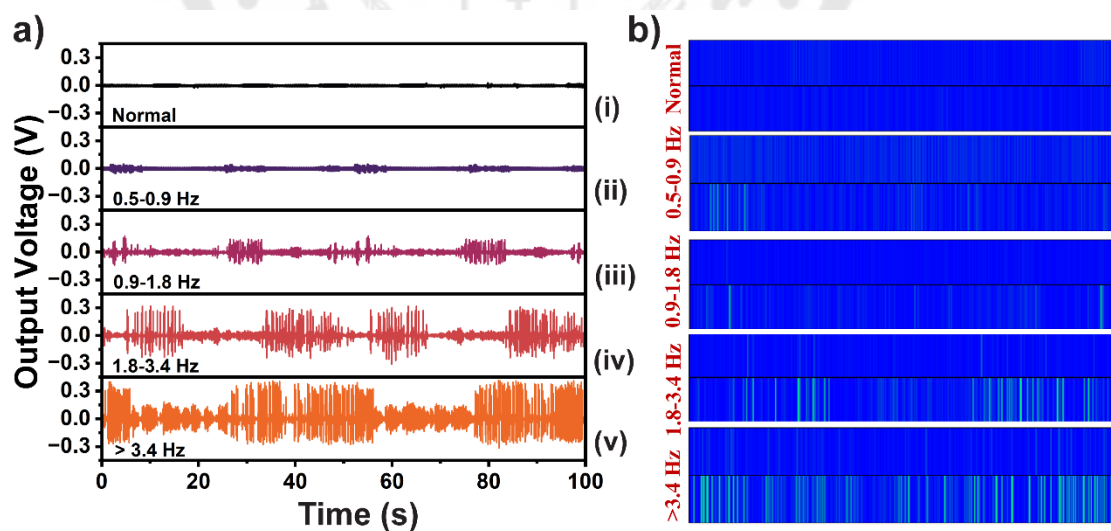
Figure 58 a) Output signal for water pouring activity and b) Wavelet packet transform decomposition of water pouring activity.
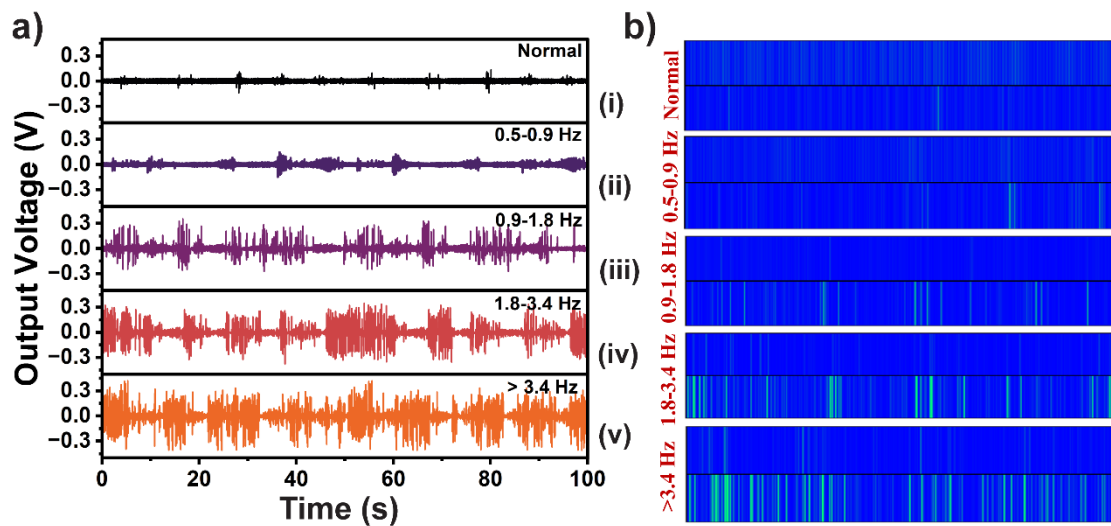
Figure 59 a) Output signal for eating activity and b) Wavelet packet transform decomposition of eating activity
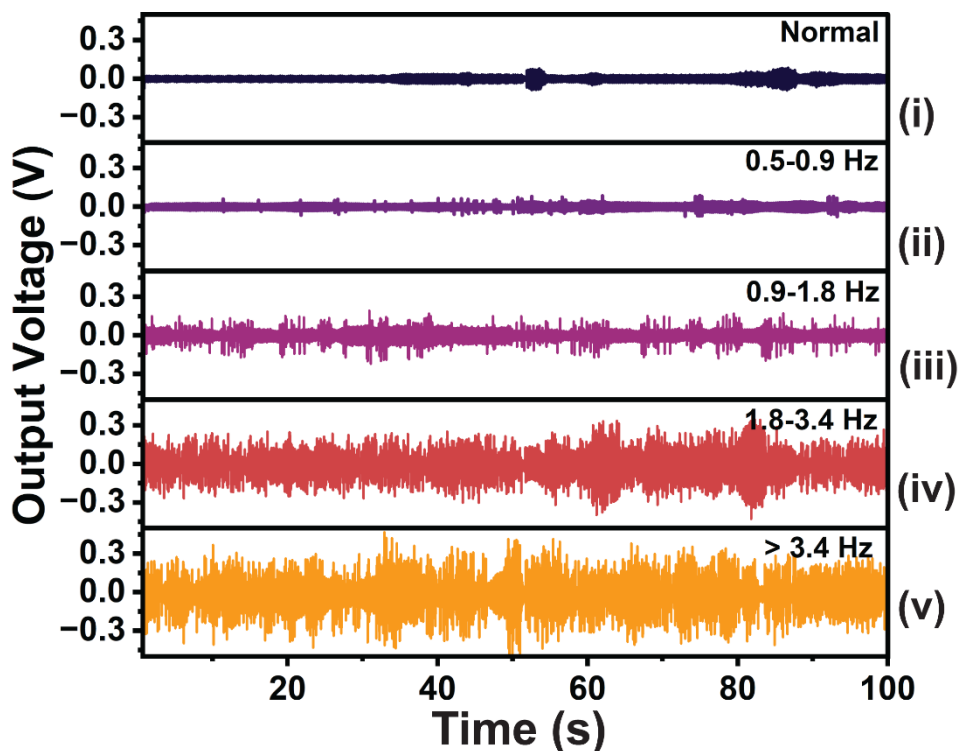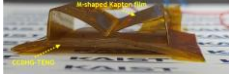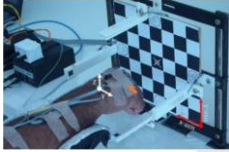
Figure 60 Output signal for writing activity

In this research, a new type of tremor sensor named WW-TES was designed to monitor tremors in PD. Unlike previous work that integrated various sensors such as Accelerometers (ACC), Gyroscopes, and Inertial Measurement Units (IMUs) into the main sensor, the WW-TES sensor is designed to be compact and lightweight. Previous studies have shown that sensors like ACC, Gyro, and IMUs can effectively detect the frequency range of PD tremors. However, integrating multiple sensors into one device can result in a larger and heavier tremor sensor. The WW-TES sensor was developed using a triboelectric sensor mechanism approach. The results of the study demonstrated that the WW-TES sensor could accurately detect tremors in the frequency range associated with PD. Furthermore, due to its compact size and lightweight design, it is more convenient for patients to use compared to traditional sensors as shown in table 5.

Table 5 Comparison of sensor devices for monitoring tremor in Parkinson's disease.

Device/ Body Position	Frequency (Hz) test	Weight	Sensor type and Sensing principle	Output signal	Power source	Ref.
RoMM (1999)	0.25 -3.25	Not portable	**Gyro**: Measures angular velocity	Frequency power spectrum (FPS) indicated to dyskinesia severity	Battery	(63)
A Mobile Cloud-Based sensor (2015)	4-6	heavy	**ACC**: Measures acceleration force	Electrical signal proportional to acceleration	Battery	(127)
(2016)	3-12	Heavy	**ACC**: detect changes in acceleration, **Gyro**: Measures angular velocity, **Mag**: Magnetic field	Magnitude of electrical signal proportional to motions	Battery	(140)
SensHand (2020)	3.5–7.5	Light weight	**IMUs**: Combination of ACC, GYRO, and sometimes MAG	Electrical signals (combined)	Battery	(141)

Device/ Body Position	Frequency (Hz) test	Weight	Sensor type and Sensing principle	Output signal	Power source	Ref.
CCDHG-TENG (2021)	2-10	Light weight	**TENG:** Converts mechanical energy into electrical energy through triboelectrification and electrostatic induction.	Electrical output relatively to frequency	Self-powered	(30)
NCC sensor (2021)	-	Not portable	**Capacitive sensor:** Measure change in capacitance **Gyro:** Measures angular velocity	Electrical signal related to movement patterns and position changes	Battery	(142)
(2022)	2	Not portable	**EMG:** Muscle electrical activity	Electrical signal related to tremor activity	Battery	(143)
WW-TES (2024)	3-7 Hz	Light weight	**Triboelectric sensor:** Converts mechanical energy into electrical energy through triboelectrification and electrostatic induction.	Electrical voltage or current proportion to the movement	Self-powered	This work

CHAPTER 5

CONCLUSIONS

5.1 The Results of Materials Characterization and Electrical Output

5.1.1 The Results Polytetrafluoroethylene (PTFE) Surface Modification Characterization and Electrical Output

Significant insights have been gained from investigating the use of PTFE film as a tribo-negative material for sensor construction. The initial characterization of commercial PTFE through ATR-IR confirmed its chemical composition, revealing characteristic absorption peaks associated with PTFE functional groups. Subsequent surface modification *via* sandpaper polishing aimed to enhance the sensor's output, with ATR-IR analysis confirming the alteration of surface morphology while maintaining the chemical structure of PTFE.

The SEM results further revealed the morphological changes induced by surface modification, showcasing a noticeable enhancement in surface roughness. This enhancement was corroborated by AFM, which revealed a significant increase in Sq from 45.4 to 227.9 nm post-polishing.

The electrical performance evaluation of both pristine and surface-modified PTFE demonstrated marked improvements in V_{OC} and I_{SC} for the modified PTFE. It was found that the VOC and ISC of pristine PTFE were measured at approximately 17.59 V and 71.20 nA, respectively. In contrast, the V_{OC} and I_{SC} of modified PTFE were found to be approximately 29.53 V and 112.94 nA, respectively. These values represent an approximate increase of 1.8 times for V_{OC} and 1.6 times for I_{SC} compared to pristine PTFE.

5.1.2 The Results of Oscillating Plate

The characterization of the automatic watch oscillating plate using the EDS technique has provided valuable insights into its elemental composition. The EDS analysis revealed the presence of elements consistent with stainless steel, including C, O, Si, P, S, Cr, Fe, and Ni, confirming the material's composition. It is important to

emphasize that while EDS can accurately identify the elemental composition of a material, it cannot determine the specific type or grade of stainless steel. Nonetheless, the confirmation of stainless-steel composition adds to our understanding of the oscillating plate's properties and materials used in its construction.

5.2 The Results of Electrical Output Performance of Regular Free-Standing Mode Triboelectric Sensor (FS-TES)

The electrical output performance of a regular free-standing triboelectric sensor (FS-TES) was investigated to assess the effect of the electrode distance parameter on the electrical output signal. The aim of this analysis was to identify the most suitable distance to optimize the performance of subsequent devices.

The investigation into the FS-TES operation revealed a critical dependence on electrode distance for optimal electrical output. Results indicated that an electrode distance of 5 mm provides the highest output signals of both V_{OC} and I_{SC} around 17.8 V and 102.5 nA, respectively. Beyond this distance, a reduction in output signals was observed due to the breakdown effect, underscoring the importance of maintaining an optimal electrode gap.

5.3 The Results of Fabrication of The Wristwatch-Like TES (WW-TES)

The fabrication of the device frame is a crucial aspect of developing a functional WW-TES. Beginning with the design phase using the Shapr3D program. The cylindrical frame, measuring 2 mm in width, 7 mm in height, and 34 mm in diameter, was carefully crafted to accommodate the necessary components. Transitioning from the digital design to physical realization, 3D printing using PLA filament and a Raise3D printer facilitated the fabrication process, and the final result was a device with a diameter of 33 mm, a height of 7 mm, and a side wall thickness of 2 mm. Initial designs of the WW-TES focused on incorporating the oscillating plate within a circular frame. However, the first and second designs encountered challenges related to the distance between the contact materials, hindering effective contact with the oscillating plate. Subsequent revisions led to the development of a third design, featuring a more optimized structure with appropriate design. The final design of the WW-TES, characterized by a diameter of

33 mm, a height of 7 mm, and a side wall thickness of 2 mm. The frame featured a platform in the center and two inward extensions for placement of the oscillating plate and PTFE.

5.4 The Results of Electrical Output Performance of The Wristwatch-Like TES (WW-TES)

The electrical output performance of the WW-TES underwent comprehensive evaluation to validate its efficacy as a tremor detection device. Utilizing an orbital shaker as a vibration generator, the device's output signals, including V_{OC} and I_{SC}, were studied across varying electrode distances of 0, 5, 12, 17 and 35 mm. Results mirrored those of the regular FS-TES, with optimal electrical output observed at an electrode distance of 5 mm, showcasing V_{OC} and I_{SC} values of approximately 0.61 V and 3.5 nA, respectively. This finding underscores the significance of electrode distance in enhancing device performance, establishing 5 mm as the optimal parameter for constructing the WW-TES. Further investigation focused on the device's frequency sensitivity, crucial for detecting tremors associated with PD severity. By assessing tremor frequencies ranging from 3 to 7 Hz, the WW-TES demonstrated remarkable sensitivity and responsiveness, aligning with characteristic PD tremor frequencies.

To assess device stability, the WW-TES underwent rigorous testing under controlled vibration conditions using an orbital shaker. Results revealed consistent electrical output throughout vibration cycles, affirming the device's stability and reliability in detecting tremors. Furthermore, extended testing over 4000 seconds demonstrated sustained performance, highlighting the device's robustness and suitability for long-term monitoring applications.

However, the performance of the WW-TES is sensitive to environmental factors, particularly humidity levels, which can affect the electrical output signal. Increased humidity levels will result in a reduced output signal, highlighting the importance of operating the WW-TES in low humidity environments to ensure reliable and accurate performance.

5.5 The Results of Practical Test

The practical application testing of the WW-TES has demonstrated its potential as a valuable tool for monitoring PD tremors. Tremors are a key symptom of PD, and their severity often correlates with the progression of the disease. By simulating tremors corresponding to different levels of PD severity through activities of daily living (ADLs), such as pouring water, eating, and writing, the WW-TES device was evaluated for its proficiency in detecting tremors.

During the experiments, the WW-TES device was worn on the wrist, and the intensity of tremors was adjusted according to the frequency specified by the MDS-UPDRS scale. The output signals generated by the device accurately reflected the tremor intensity, with higher tremor frequencies resulting in higher electrical output signals. This direct correlation between tremor severity and electrical output signal amplitude indicates that the WW-TES device is capable of detecting the severity of PD tremors and tracking disease progression.

Overall, the results of the practical application testing highlight the efficacy and promise of the WW-TES device as a valuable tool for monitoring PD tremors in clinical settings and improving the quality of life for PD patients.

5.6 Remarks and Future Perspectives

This thesis presents the developments on triboelectric sensors for such an application as PD monitoring by designing the TES in the frame by wristwatch liked structure. The device is called WW-TES. The results indicated that this WW-TES can be used to effectively detect PD tremor from tracking electrical output signal. Discrimination of signals can be observed by their amplitude corresponding to tremor severity levels ("normal" to "severe") based on MDS-UPDRS tremor frequency. However, there is still plenty of room for development of this kind of device to further enhance the sensor performance. There are many aspects to consider for optimization. Firstly, a thorough understanding of the limitations of the sensor is essential. In addition, the characterization of sensor performance through key parameters, with a particular focus on the 3S properties: stability, selectivity, and sensitivity, should be addressed. By addressing

these aspects, we can significantly improve the detection of PD while ensuring the accuracy and reliability of the results that will not only strengthen the sensor's effectiveness in PD detection but also contribute to its overall performance in practical applications.

5.6.1 WW-TES Limitations

In actual use, the sensor will be exposed to a variety of atmospheric conditions, and there may be other uncontrollable factors that affect its performance. One significant factor is humidity. Experimental results indicate that humidity has a substantial impact on the electrical output signal of the sensor. Specifically, as humidity increases, the output signal decreases significantly. To mitigate this issue, several strategies can be employed. First, the sensor should be designed with a protective cover to shield it from humidity. Additionally, the materials used in the sensor's fabrication can be enhanced to possess hydrophobic property. This would help repel water or moisture that may adhere to the tribomaterials, thereby preserving the sensor's functionality and accuracy in various environmental conditions.

Repeatability is one of the factors in sensor design. A well-designed sensor should be able to consistently reproduce the same electrical output when exposed to identical conditions. This means that the sensor should be highly reliable in its measurements, ensuring that it provides consistent results each time it is used or reassembled.

5.6.2 WW-TES properties

5.6.2.1 Stability of WW-TES

The stability of a PD tremor sensor refers to its ability to detect tremors consistently and accurately over time, without fluctuation or error. Here are some key aspects that define the stability requirements for such sensors:

- Consistency: The sensor should provide a consistent output signal of tremor severity based on tremor frequency over multiple sessions and extended periods of use. This ensures reliable monitoring of PD progression. In this study, the consistency of the output signal was

evaluated through a series of tests. The WW-TES device was subjected to a cyclical vibration pattern: vibration for 10 seconds, followed by a 10 second pause and then resumption of vibration, repeated for a total of 10 cycles. This was done to monitor the consistency of the generated electrical output signals. The results showed that the WW-TES device maintained a consistent electrical output signal amplitude throughout the experiment.

- Long-term Performance: The sensor should maintain its ability to detect tremors over a long period of time, ensuring reliable data collection for ongoing monitoring and treatment adjustments. In this study, the long-term performance of the WW-TES device was tested by subjecting it to rotate 4000 cycles. The results revealed that the device could operate continuously for 4000 cycles without any decrease in electrical output signal throughout the operation.

5.6.2.2 Sensitivity of WW-TES

The sensitivity of a PD tremor sensor refers to its ability to detect tremors very quickly. A high sensitivity sensor can detect even the lowest frequency tremor. This includes detecting subtle tremors characteristic of PD, across a wide dynamic range of severity (from mild to severe), and within the specific frequency range typical of PD tremors (3 to 7 Hz). When tremor occurs, the oscillating plate within the device must promptly respond by rotating against the PTFE and generating an output signal corresponding to the tremor level. This sensitivity plays a critical role in enabling the sensor to effectively monitor and assess tremor severity over time, thereby facilitating better management and treatment of PD. To assess the sensitivity of the WW-TES device to PD tremor, an experiment can be performed in which the frequency of the simulated tremor gradually varied from the lowest to the highest range typical of PD. The electrical signals received should correspond directly to the frequencies, particularly at lower frequencies where the tremor is less pronounced. At these frequencies the peak amplitude of the signal should remain relatively low. As the tremor frequency increases,

simulating the more intense tremors typical of PD, the peak amplitude of the output signal should increase proportionally. The sensor should be able to discriminate between signals based on the differing frequencies.

5.6.2.3 Selectivity of WW-TES

The selectivity refers to the sensor ability to specifically identify and measure tremors associated with PD while distinguishing them from other types of movements. Selectivity is crucial for ensuring that the sensor accurately targets the PD tremors without being influenced by other physiological or environmental signals. The ability to differentiate between can be tested by conducting the experiment with various types of vibrations and frequencies. First, test the WW-TES device with known PD tremor frequencies, typically ranging from 3-7 Hz. This helps establish amplitude, and rhythmic patterns specific to PD tremors. Next, perform various voluntary movements such as tapping, shaking, or waving the hands, and observe the output signal's amplitude and pattern. Then, conduct tests where both voluntary movements and simulated PD tremors are performed simultaneously. The observed output signals should exhibit greater peak amplitude due to the increased intensity from the combined forces of voluntary movements and tremors. Keep this data as standard information and consider using advanced data analysis techniques, such as machine learning algorithms, to process the sensor data. These techniques can help differentiate between PD tremors and other movements by learning from a large dataset of labeled examples. In addition, the freestanding design of the WW-TES has the advantage of separating the signals when the wearer experiences hand tremor by twisting the wrist either to the left or to the right. This action causes the oscillating plate inside the device to rotate, making contact with the PTFE on either side in a clockwise or anti-clockwise direction, generating different patterns of electrical signals. This makes it possible to determine whether the patient has PD tremor or another type of tremor pattern.

5.6.3 Possible Future Designs for Improving the Sensor's Properties and Facilitating Potential Commercialization

To further enhance the future design of the WW-TES sensor for efficiency and commercialization, consider the following points

5.6.3.1 Structural Design Improvements

Future design and development efforts will be crucial in improving the capabilities of the WW-TES device to ensure that it is able to effectively monitor PD tremors. With a focus on the design of a suitable structure, the efficiency of the sensor in terms of sensitivity, selectivity and stability can be significantly improved. Here are key areas for further development:

- To increase the sensitivity of the WW-TES sensor's structural design, it is important to optimize the contact surfaces between the triboelectric materials to maximize charge generation and increase the effective contact area. This enhancement improves the sensor's responsiveness to even the slightest vibrations.

- To enhance selectivity in the structural design, optimize electrode placement and sensor positioning on the wrist. Consider that different areas such as above, below, or to the side of the wrist may capture distinct signal patterns corresponding to various tremor intensities. The device may respond differently to different levels of tremors and detect signals with varying patterns depending on the severity of tremors. Therefore, further research into these factors is necessary to effectively differentiate between the severity levels of Parkinson's disease tremors.

- To enhance stability in the structural design, ensure the sensor housing is robust and durable enough to withstand daily wear and humidity by using high-strength, lightweight materials. Additionally, prevent humidity from affecting the device by considering methods such as adding a sealing component to shield the sensor from

moisture, dust, and contaminants, thereby maintaining consistent performance in diverse environments. Securely fasten components such as the oscillating plate, triboelectric materials, and electrodes to withstand strong tremors, ensuring they are tight, stable, and resistant to loosening.

5.6.3.2 Integration with Electronic Circuits

Integrating the WW-TES sensor with advanced electronic circuits can significantly enhance signal processing capabilities will allow for signal amplification, and real-time analysis, thus improving the accuracy and reliability of tremor detection. Incorporating wireless communication modules will enable seamless data transmission to external devices such as smartphones, tablets, or computers, facilitating remote monitoring and data analysis.

5.6.3.3 Commercially Development

The primary focus should be on developing scalable manufacturing processes to produce the WW-TES device cost-effectively, while ensuring consistently high reliability of the output signal. This can be achieved by ensuring stable performance and integrating electronic circuits, along with enabling wireless functionality, which would significantly enhance the device's reliability. Additionally, consideration should be given to obtaining the necessary certifications and regulatory approvals for medical device standards. Develop a comprehensive commercialization strategy including market analysis, pricing strategies, distribution plans and robust customer support to facilitate successful market entry.

REFERENCES

1.   Pringsheim T, Jette N, Frolkis A, Steeves TD. The prevalence of Parkinson's disease: a systematic review and meta-analysis. Mov Disord. 2014;29(13):1583-90.

2.   Tysnes OB, Storstein A. Epidemiology of Parkinson's disease. J Neural Transm (Vienna). 2017;124(8):901-5.

3.   Bastide MF, Meissner WG, Picconi B, Fasano S, Fernagut PO, Feyder M, et al. Pathophysiology of L-dopa-induced motor and non-motor complications in Parkinson's disease. Prog Neurobiol. 2015;132:96-168.

4.   Jost WH, Brück C. Drug interactions in the treatment of Parkinson's disease. Journal of Neurology. 2002;249(3):iii24-iii9.

5.   Wiseman V, Conteh L, Matovu F. Using diaries to collect data in resource-poor settings: questions on design and implementation. Health Policy and Planning. 2005;20(6):394-404.

6.   Lonini L, Dai A, Shawen N, Simuni T, Poon C, Shimanovich L, et al. Wearable sensors for Parkinson's disease: which data are worth collecting for training symptom detection models. npj Digital Medicine. 2018;1(1):64.

7.   Nguyen A, Roth N, Ghassemi NH, Hannink J, Seel T, Klucken J, et al. Development and clinical validation of inertial sensor-based gait-clustering methods in Parkinson's disease. Journal of NeuroEngineering and Rehabilitation. 2019;16(1):77.

8.   San-Segundo R, Zhang A, Cebulla A, Panev S, Tabor G, Stebbins K, et al. Parkinson's Disease Tremor Detection in the Wild Using Wearable Accelerometers. Sensors [Internet]. 2020; 20(20).

9.   Anicet Zanini R, Luna Colombini E. Parkinson's Disease EMG Data Augmentation and Simulation with DCGANs and Style Transfer. Sensors [Internet]. 2020; 20(9).

10.   O'Day J, Lee M, Seagers K, Hoffman S, Jih-Schiff A, Kidziński Ł, et al. Assessing inertial measurement unit locations for freezing of gait detection and patient preference. Journal of NeuroEngineering and Rehabilitation. 2022;19.

11.   Warmerdam E, Romijnders R, Welzel J, Hansen C, Schmidt G, Maetzler W. Quantification of Arm Swing during Walking in Healthy Adults and Parkinson's Disease Patients: Wearable Sensor-Based Algorithm Development and Validation. Sensors. 2020;20:5963.

12.   Cole BT, Roy SH, Nawab SH, editors. Detecting freezing-of-gait during unscripted and unconstrained activity. 2011 Annual International Conference of the IEEE Engineering in Medicine and Biology Society; 2011 30 Aug.-3 Sept. 2011.

13.   Suppa A, Kita A, Leodori G, Zampogna A, Nicolini E, Lorenzi P, et al. l-DOPA and Freezing of Gait in Parkinson's Disease: Objective Assessment through a Wearable Wireless System. Front Neurol. 2017;8:406.

14.   Williamson JR, Telfer B, Mullany R, Friedl KE. Detecting Parkinson's Disease from Wrist-Worn Accelerometry in the U.K. Biobank. Sensors [Internet]. 2021; 21(6).

15.   Albert M, Toledo S, Shapiro M, Koerding K. Using Mobile Phones for Activity Recognition in Parkinson's Patients. Frontiers in Neurology. 2012;3.

16.   Koo J, MacEwan MR, Kang S-K, Won SM, Stephen M, Gamble P, et al. Wireless bioresorbable electronic system enables sustained nonpharmacological neuroregenerative therapy. Nature Medicine. 2018;24(12):1830-6.

17.   Pu X, Liu M, Chen X, Sun J, Du C, Zhang Y, et al. Ultrastretchable, transparent triboelectric nanogenerator as electronic skin for biomechanical energy harvesting and tactile sensing. Science Advances.3(5):e1700015.

18.   Niu S, Wang ZL. Theoretical systems of triboelectric nanogenerators. Nano Energy. 2015;14:161-92.

19.   Wang H, Sakamoto H, Asai H, Zhang J-H, Meboso T, Uchiyama Y, et al. An all-fibrous triboelectric nanogenerator with enhanced outputs depended on the polystyrene charge storage layer. Nano Energy. 2021;90:106515.

20.   Kim DW, Lee JH, You I, Kim JK, Jeong U. Adding a stretchable deep-trap interlayer for high-performance stretchable triboelectric nanogenerators. Nano Energy. 2018;50:192-200.

21.   Lu Z, Xie Z, Zhu Y, Jia C, Zhang Y, Yang J, et al. A Stable and Durable Triboelectric Nanogenerator for Speed Skating Land Training Monitoring. Electronics [Internet]. 2022; 11(22).

22.   Li W, Lu L, Kottapalli AGP, Pei Y. Bioinspired sweat-resistant wearable triboelectric nanogenerator for movement monitoring during exercise. Nano Energy. 2022;95:107018.

23.   Su K, Lin X, Liu Z, Tian Y, Peng Z, Meng B. Wearable Triboelectric Nanogenerator with Ground-Coupled Electrode for Biomechanical Energy Harvesting and Sensing. Biosensors [Internet]. 2023; 13(5).

24.   Delgado-Alvarado E, Martínez-Castillo J, Zamora-Peredo L, Gonzalez-Calderon JA, López-Esparza R, Ashraf MW, et al. Triboelectric and Piezoelectric Nanogenerators for Self-Powered Healthcare Monitoring Devices: Operating Principles, Challenges, and Perspectives. Nanomaterials [Internet]. 2022; 12(24).

25.   Pu X, An S, Tang Q, Guo H, Hu C. Wearable triboelectric sensors for biomedical monitoring and human-machine interface. iScience. 2021;24(1):102027.

26.   Yi Q, Pei X, Das P, Qin H, Lee SW, Esfandyarpour R. A self-powered triboelectric MXene-based 3D-printed wearable physiological biosignal sensing system for on-demand, wireless, and real-time health monitoring. Nano Energy. 2022;101:107511.

27.   Zhang X-S, Han M, Kim B, Bao J-F, Brugger J, Zhang H. All-in-one self-powered flexible microsystems based on triboelectric nanogenerators. Nano Energy. 2018;47:410-26.

28.   Li R, Wei X, Xu J, Chen J, Li B, Wu Z, et al. Smart Wearable Sensors Based on Triboelectric Nanogenerator for Personal Healthcare Monitoring. Micromachines (Basel). 2021;12(4).

29.   Vera Anaya D, Yuce MR. Stretchable triboelectric sensor for measurement of the forearm muscles movements and fingers motion for Parkinson's disease assessment and assisting technologies. MEDICAL DEVICES & SENSORS. 2021;4(1):e10154.

30.   Kim J-N, Lee J, Lee H, Oh I-K. Stretchable and self-healable catechol-chitosan-diatom hydrogel for triboelectric generator and self-powered tremor sensor targeting at Parkinson disease. Nano Energy. 2021;82:105705.

31.   Liu G, Liu R, Guo H, Xi Y, Wei D, Hu C. A Novel Triboelectric Generator Based on the Combination of a Waterwheel-Like Electrode with a Spring Steel Plate For Efficient Harvesting of Low-Velocity Rotational Motion Energy. Advanced Electronic Materials. 2016;2(5):1500448.

32.   Yu Y, Li H, Zhao D, Gao Q, Li X, Wang J, et al. Material's selection rules for high performance triboelectric nanogenerators. Materials Today. 2023;64:61-71.

33.   Zhang R, Olin H. Material choices for triboelectric nanogenerators: A critical review. EcoMat. 2020;2(4):e12062.

34.   Ibrahim M, Jiang J, Wen Z, Sun X. Surface Engineering for Enhanced Triboelectric Nanogenerator. Nanoenergy Advances [Internet]. 2021; 1(1):[58-80 pp.].

35.   Li M, Cheng W-Y, Li Y-C, Wu H-M, Wu Y-C, Lu H-W, et al. Deformable, resilient, and mechanically-durable triboelectric nanogenerator based on recycled coffee waste for wearable power and self-powered smart sensors. Nano Energy. 2021;79:105405.

36.   Vivekananthan V, Chandrasekhar A, Alluri N, Purusothaman Y, Khandelwal G, Kim S-J. Triboelectric Nanogenerators: Design, Fabrication, Energy Harvesting, and Portable-Wearable Applications. 2020.

37.   Nahian SA, Cheedarala RK, Ahn KK. A study of sustainable green current generated by the fluid-based triboelectric nanogenerator (FluTENG) with a comparison of contact and sliding mode. Nano Energy. 2017;38:447-56.

38.   Qiu Y, Yang D, Li B, Shao S, Hu L. Wearable triboelectric nanogenerators based on hybridized triboelectric modes for harvesting mechanical energy. RSC Advances. 2018;8(46):26243-50.

39.   Chen J, Guo H, Hu C, Wang ZL. Robust Triboelectric Nanogenerator Achieved by Centrifugal Force Induced Automatic Working Mode Transition. Advanced Energy Materials. 2020;10(23):2000886.

40.   Pongampai S, Pakawanit P, Charoonsuk T, Vittayakorn N. Low-cost fabrication of the highly efficient triboelectric nanogenerator by designing a 3D multi-layer origami structure combined with self-charged pumping module. Nano Energy. 2021;90:106629.

41.   Lin Z, Zhang B, Guo H, Wu Z, Zou H, Yang J, et al. Super-robust and frequency-multiplied triboelectric nanogenerator for efficient harvesting water and wind energy. Nano Energy. 2019;64:103908.

42.   Liao J, Zou Y, Jiang D, Liu Z, Qu X, Li Z, et al. Nestable arched triboelectric nanogenerator for large deflection biomechanical sensing and energy harvesting. Nano Energy. 2020;69:104417.

43.   Nagatsu T. Catecholamines and Parkinson's disease: tyrosine hydroxylase (TH) over tetrahydrobiopterin (BH4) and GTP cyclohydrolase I (GCH1) to cytokines, neuromelanin, and gene therapy: a historical overview. Journal of Neural Transmission. 2023.

44.   Barone P. Neurotransmission in Parkinson's disease: beyond dopamine. European Journal of Neurology. 2010;17(3):364-76.

45.   DeMaagd G, Philip A. Parkinson's Disease and Its Management: Part 1: Disease Entity, Risk Factors, Pathophysiology, Clinical Presentation, and Diagnosis. P t. 2015;40(8):504-32.

46.   Hallett M. Parkinson's disease tremor: pathophysiology. Parkinsonism & Related Disorders. 2012;18:S85-S6.

47.   Berardelli A, Rothwell JC, Thompson PD, Hallett M. Pathophysiology of bradykinesia in Parkinson's disease. Brain. 2001;124(11):2131-46.

48.   Berardelli A, Sabra AF, Hallett M. Physiological mechanisms of rigidity in Parkinson's disease. Journal of Neurology, Neurosurgery &amp; Psychiatry. 1983;46(1):45.

49.   Bloem BR. Postural instability in Parkinson's disease. Clinical Neurology and Neurosurgery. 1992;94:41-5.

50.   Poewe W. Non-motor symptoms in Parkinson's disease. European Journal of Neurology. 2008;15(s1):14-20.

51.   Church FC. Treatment Options for Motor and Non-Motor Symptoms of Parkinson's Disease. Biomolecules [Internet]. 2021; 11(4).

52.   Amara AW, Memon AA. Effects of Exercise on Non-motor Symptoms in Parkinson's Disease. Clinical Therapeutics. 2018;40(1):8-15.

53.   Lamba R, Gulati T, Jain A. COMPARATIVE ANALYSIS OF PARKINSON'S DISEASE DIAGNOSIS SYSTEM: A REVIEW. Advances in Mathematics: Scientific Journal. 2020;9:3401-8.

54.   Jankovic J. Parkinson's disease: clinical features and diagnosis. Journal of Neurology, Neurosurgery &amp; Psychiatry. 2008;79(4):368.

55.   Heim B, Krismer F, De Marzi R, Seppi K. Magnetic resonance imaging for the diagnosis of Parkinson's disease. Journal of Neural Transmission. 2017;124(8):915-64.

56.   Deeb J, Shah M, Muhammed N, Gunasekera R, Gannon K, Findley LJ, et al. A basic smell test is as sensitive as a dopamine transporter scan: comparison of olfaction, taste and DaTSCAN in the diagnosis of Parkinson's disease. QJM: An International Journal of Medicine. 2010;103(12):941-52.

57.   Wiseman V, Conteh L, Matovu F. Using diaries to collect data in resource-poor settings: questions on design and implementation. Health Policy Plan. 2005;20(6):394-404.

58.   Achey M, Aldred JL, Aljehani N, Bloem BR, Biglan KM, Chan P, et al. The past, present, and future of telemedicine for Parkinson's disease. Movement Disorders. 2014;29(7):871-83.

59.   Cubo E, Delgado-López PD. Telemedicine in the Management of Parkinson's Disease: Achievements, Challenges, and Future Perspectives. Brain Sci. 2022;12(12).

60.   Linares-del Rey M, Vela-Desojo L, Cano-de la Cuerda R. Mobile phone applications in Parkinson's disease: a systematic review. Neurología (English Edition). 2019;34(1):38-54.

61.   Lee J, Yeom I, Chung ML, Kim Y, Yoo S, Kim E. Use of Mobile Apps for Self-care in People With Parkinson Disease: Systematic Review. JMIR Mhealth Uhealth. 2022;10(1):e33944.

62.   Lu R, Xu Y, Li X, Fan Y, Zeng W, Tan Y, et al. Evaluation of Wearable Sensor Devices in Parkinson's Disease: A Review of Current Status and Future Prospects. Parkinsons Dis. 2020;2020:4693019.

63.   Burkhard PR, Shale H, Langston JW, Tetrud JW. Quantification of dyskinesia in Parkinson's disease: Validation of a novel instrumental method. Movement Disorders. 1999;14(5):754-63.

64.   Salarian A, Russmann H, Wider C, Burkhard PR, Vingerhoets FJ, Aminian K. Quantification of tremor and bradykinesia in Parkinson's disease using a novel ambulatory monitoring system. IEEE Trans Biomed Eng. 2007;54(2):313-22.

65.   Aich S, Pradhan PM, Park J, Sethi N, Vathsa VS, Kim H-C. A Validation Study of Freezing of Gait (FoG) Detection and Machine-Learning-Based FoG Prediction Using Estimated Gait Characteristics with a Wearable Accelerometer. Sensors [Internet]. 2018; 18(10).

66.   Vescio B, Quattrone A, Nisticò R, Crasà M, Quattrone A. Wearable Devices for Assessment of Tremor. Frontiers in Neurology. 2021;12.

67.   Daube JR, Rubin DI. Needle electromyography. Muscle & Nerve. 2009;39(2):244-70.

68.   Qiang Z, Shi B, Wang Z. Recent Progress on Piezoelectric and Triboelectric Energy Harvesters in Biomedical Systems. Advanced Science. 2017;4:1700029.

69.   Khan U, Hinchet R, Ryu H, Kim S-W. Research Update: Nanogenerators for self-powered autonomous wireless sensors. APL Materials. 2017;5.

70.   Qin K, Chen C, Pu X, Tang Q, He W, Liu Y, et al. Magnetic Array Assisted Triboelectric Nanogenerator Sensor for Real-Time Gesture Interaction. Nano-Micro Letters. 2021;13(1):51.

71.   Zhang D, Yang Y, Xu Z, Wang D, Du C. An eco-friendly gelatin based triboelectric nanogenerator for a self-powered PANI nanorod/NiCo2O4 nanosphere ammonia gas sensor. Journal of Materials Chemistry A. 2022;10(20):10935-49.

72.   Luo Y, Cao X, Wang ZL. Self-powered smart agriculture sensing using triboelectric nanogenerators based on living plant leaves. Nano Energy. 2023;107:108097.

73.   Sardana S, Singh Z, Sharma AK, Kaur N, Pati PK, Mahajan A. Self-powered biocompatible humidity sensor based on an electrospun anisotropic triboelectric

nanogenerator for non-invasive diagnostic applications. Sensors and Actuators B: Chemical. 2022;371:132507.

74. Ramaswamy SH, Shimizu J, Chen W, Kondo R, Choi J. Investigation of diamond-like carbon films as a promising dielectric material for triboelectric nanogenerator. Nano Energy. 2019;60:875-85.

75. Wang H, Zhu J, He T, Zhang Z, Lee C. Programmed-triboelectric nanogenerators—A multi-switch regulation methodology for energy manipulation. Nano Energy. 2020;78:105241.

76. Kwak MS, Lim K-W, Lee HY, Peddigari M, Jang J, Jeong CK, et al. Multiscale surface modified magneto-mechano-triboelectric nanogenerator enabled by eco-friendly NaCl imprinting stamp for self-powered IoT applications. Nanoscale. 2021;13(18):8418-24.

77. Zhu G, Yang WQ, Zhang T, Jing Q, Chen J, Zhou YS, et al. Self-Powered, Ultrasensitive, Flexible Tactile Sensors Based on Contact Electrification. Nano Letters. 2014;14(6):3208-13.

78. Xu Z, Zhang D, Cai H, Yang Y, Zhang H, Du C. Performance enhancement of triboelectric nanogenerators using contact-separation mode in conjunction with the sliding mode and multifunctional application for motion monitoring. Nano Energy. 2022;102:107719.

79. Zhang Z, Bai Y, Xu L, Zhao M, Shi M, Wang ZL, et al. Triboelectric nanogenerators with simultaneous outputs in both single-electrode mode and freestanding-triboelectric-layer mode. Nano Energy. 2019;66:104169.

80. Xie L, Menet CG, Ching H, Du R. The Automatic Winding Device of a Mechanical Watch Movement and Its Application in Energy Harvesting. Journal of Mechanical Design. 2009;131(7).

81. Zurbuchen A, Haeberlin A, Pfenniger A, Bereuter L, Schaerer J, Jutzi F, et al. Towards Batteryless Cardiac Implantable Electronic Devices—The Swiss Way. IEEE Transactions on Biomedical Circuits and Systems. 2017;11(1):78-86.

82.   Zurbuchen A, Haeberlin A, Bereuter L, Wagner J, Pfenniger A, Omari S, et al. The Swiss approach for a heartbeat-driven lead- and batteryless pacemaker. Heart Rhythm. 2017;14(2):294-9.

83.   Bhullar S, Çelik Bedeloǧlu A, Jun M. Characterization and Auxetic effect of Polytetrafluoroethylene Tubular structure. International Journal of Advanced Science and Engineering. 2014;1:8-13.

84.   Palmaz JC. Review of polymeric graft materials for endovascular applications. J Vasc Interv Radiol. 1998;9(1 Pt 1):7-13.

85.   Mahltig B. High-Performance Fibres – A Review of Properties and IR-Spectra. Tekstilec. 2021;64:96-118.

86.   Yang W, Chen J, Zhu G, Yang J, Bai P, Su Y, et al. Harvesting Energy from the Natural Vibration of Human Walking. ACS Nano. 2013;7(12):11317-24.

87.   Kim W, Okada T, Park H-W, Kim J, Kim S, Kim S-W, et al. Surface modification of triboelectric materials by neutral beams. Journal of Materials Chemistry A. 2019;7(43):25066-77.

88.   Huang T, Lu M, Yu H, Zhang Q, Wang H, Zhu M. Enhanced Power Output of a Triboelectric Nanogenerator Composed of Electrospun Nanofiber Mats Doped with Graphene Oxide. Scientific Reports. 2015;5(1):13942.

89.   Lee JH, Yu I, Hyun S, Kim JK, Jeong U. Remarkable increase in triboelectrification by enhancing the conformable contact and adhesion energy with a film-covered pillar structure. Nano Energy. 2017;34:233-41.

90.   Cui N, Gu L, Lei Y, Liu J, Qin Y, Ma X, et al. Dynamic Behavior of the Triboelectric Charges and Structural Optimization of the Friction Layer for a Triboelectric Nanogenerator. ACS Nano. 2016;10(6):6131-8.

91.   Jeong CK, Baek KM, Niu S, Nam TW, Hur YH, Park DY, et al. Topographically-Designed Triboelectric Nanogenerator via Block Copolymer Self-Assembly. Nano Letters. 2014;14(12):7031-8.

92.   Wang S, Xie Y, Niu S, Lin L, Liu C, Zhou YS, et al. Maximum surface charge density for triboelectric nanogenerators achieved by ionized-air injection: methodology and theoretical understanding. Adv Mater. 2014;26(39):6720-8.

93.   Zhou Y, Deng W, Xu J, Chen J. Engineering Materials at the Nanoscale for Triboelectric Nanogenerators. Cell Reports Physical Science. 2020;1(8):100142.

94.   Zhao L, Zheng Q, Ouyang H, Li H, Yan L, Shi B, et al. A size-unlimited surface microstructure modification method for achieving high performance triboelectric nanogenerator. Nano Energy. 2016;28:172-8.

95.   Zhao J, Mu J, Cui H, He W, Zhang L, He J, et al. Hybridized Triboelectric-Electromagnetic Nanogenerator for Wind Energy Harvesting to Realize Real-Time Power Supply of Sensor Nodes. Advanced Materials Technologies. 2021;6(4):2001022.

96.   Prada T, Harnchana V, Lakhonchai A, Chingsungnoen A, Poolcharuansin P, Chanlek N, et al. Enhancement of output power density in a modified polytetrafluoroethylene surface using a sequential O2/Ar plasma etching for triboelectric nanogenerator applications. Nano Research. 2022;15(1):272-9.

97.   Maharjan P, Cho H, Rasel MS, Salauddin M, Park JY. A fully enclosed, 3D printed, hybridized nanogenerator with flexible flux concentrator for harvesting diverse human biomechanical energy. Nano Energy. 2018;53:213-24.

98.   Liu X, Yu A, Qin A, Zhai J. Highly Integrated Triboelectric Nanogenerator for Efficiently Harvesting Raindrop Energy. Advanced Materials Technologies. 2019;4(11):1900608.

99.   Lin Z-H, Cheng G, Lee S, Pradel KC, Wang ZL. Harvesting Water Drop Energy by a Sequential Contact-Electrification and Electrostatic-Induction Process. Advanced Materials. 2014;26(27):4690-6.

100.   Dudem B, Kim DH, Mule AR, Yu JS. Enhanced Performance of Microarchitectured PTFE-Based Triboelectric Nanogenerator via Simple Thermal Imprinting Lithography for Self-Powered Electronics. ACS Applied Materials & Interfaces. 2018;10(28):24181-92.

101. Yasuoka M, Wang P, Zhang K, Qiu Z, Kusaka K, Pyoun Y-S, et al. Improvement of the fatigue strength of SUS304 austenite stainless steel using ultrasonic nanocrystal surface modification. Surface and Coatings Technology. 2013;218:93-8.

102. MatWeb. 304 Stainless Steel. 2024.

103. Onwudili A, Iweka C. Full-annealing and its effect on the Mechanical Properties of Alloy 304H Stainless Steel. Journal of Engineering Research and Reports. 2021:28-44.

104. Calle L, MacDowell L, Vinje R. Electrochemical Evaluation of Stainless Steels in Acidic Sodium Chloride Solutions. 2004.

105. Loto R, Loto C, Popoola P, Ranyaoa Ms. Corrosion resistance of austenitic stainless steel in sulphuric acid. International journal of physical sciences. 2012;7:1677-88.

106. Toloei A, Stoilov V, Northwood D. Simultaneous effect of surface roughness and passivity on corrosion resistance of metals2015. 355-67 p.

107. Zhu G, Chen J, Zhang T, Jing Q, Wang ZL. Radial-arrayed rotary electrification for high performance triboelectric generator. Nature Communications. 2014;5(1):3426.

108. Wang S, Xie Y, Niu S, Lin L, Wang ZL. Freestanding Triboelectric-Layer-Based Nanogenerators for Harvesting Energy from a Moving Object or Human Motion in Contact and Non-contact Modes. Advanced Materials. 2014;26(18):2818-24.

109. Niu S, Liu Y, Chen X, Wang S, Zhou YS, Lin L, et al. Theory of freestanding triboelectric-layer-based nanogenerators. Nano Energy. 2015;12:760-74.

110. Wang X, Niu S, Yin Y, Yi F, You Z, Wang ZL. Triboelectric Nanogenerator Based on Fully Enclosed Rolling Spherical Structure for Harvesting Low-Frequency Water Wave Energy. Advanced Energy Materials. 2015;5(24):1501467.

111. Zhang Z, Hu Z, Wang Y, Wang Y, Zhang Q, Liu D, et al. Multi-Tunnel Triboelectric Nanogenerator for Scavenging Mechanical Energy in Marine Floating Bodies. Journal of Marine Science and Engineering [Internet]. 2022; 10(4).

112. Nur Farahana Mat I, Hafizal Y, Muhammad Mahfuz S, Nur Aisyah Mohd Y, Ahmad Nazirul M, Zul Izie Hafifi Mohammad G, et al. The Effect of Surface Texture on Teflon as Electrification Layer of 360° Lateral-Sliding Mode Triboelectric Generator. Journal of Advanced Research in Applied Mechanics. 2023;106(1):48-56.

113. Sriphan S, Vittayakorn N. Facile roughness fabrications and their roughness effects on electrical outputs of the triboelectric nanogenerator. Smart Materials and Structures. 2018;27(10):105026.

114. Zou Y, Xu J, Chen K, Chen J. Advances in Nanostructures for High-Performance Triboelectric Nanogenerators. Advanced Materials Technologies. 2021;6(3):2000916.

115. Song W-Z, Qiu H-J, Zhang J, Yu M, Ramakrishna S, Wang ZL, et al. Sliding mode direct current triboelectric nanogenerators. Nano Energy. 2021;90:106531.

116. Xie Y, Wang S, Niu S, Lin L, Jing Q, Yang J, et al. Grating-Structured Freestanding Triboelectric-Layer Nanogenerator for Harvesting Mechanical Energy at 85% Total Conversion Efficiency. Advanced Materials. 2014;26(38):6599-607.

117. He W, Liu W, Chen J, Wang Z, Liu Y, Pu X, et al. Boosting output performance of sliding mode triboelectric nanogenerator by charge space-accumulation effect. Nature Communications. 2020;11(1):4277.

118. Guo X, Li F, Xi Z, Hong J, Wang Y, Qian Z, et al. Boosting Free-Rotating Disk Triboelectric Nanogenerator through Alcohol-Soluble Nylon Film, Preventing Air Breakdown. ACS Applied Electronic Materials. 2024;6(1):376-85.

119. Fu J, Xia X, Xu G, Li X, Zi Y. On the Maximal Output Energy Density of Nanogenerators. ACS Nano. 2019;13(11):13257-63.

120. Lee HJ, Lee WW, Kim SK, Park H, Jeon HS, Kim HB, et al. Tremor frequency characteristics in Parkinson's disease under resting-state and stress-state conditions. Journal of the Neurological Sciences. 2016;362:272-7.

121. Ko YH, Lee SH, Leem JW, Yu JS. High transparency and triboelectric charge generation properties of nano-patterned PDMS. RSC Advances. 2014;4(20):10216-20.

122. Yang W, Chen J, Zhu G, Wen X, Bai P, Su Y, et al. Harvesting vibration energy by a triple-cantilever based triboelectric nanogenerator. Nano Research. 2013;6(12):880-6.

123. Fan F-R, Tian Z-Q, Lin Wang Z. Flexible triboelectric generator. Nano Energy. 2012;1(2):328-34.

124.   Sintusiri J, Harnchana V, Amornkitbamrung V, Wongsa A, Chindaprasirt P. Portland Cement-TiO2 triboelectric nanogenerator for robust large-scale mechanical energy harvesting and instantaneous motion sensor applications. Nano Energy. 2020;74:104802.

125.   Zurbuchen A, Pfenniger A, Stahel A, Stoeck CT, Vandenberghe S, Koch VM, et al. Energy Harvesting from the Beating Heart by a Mass Imbalance Oscillation Generator. Annals of Biomedical Engineering. 2013;41(1):131-41.

126.   Chan PY, Ripin ZM, Halim SA, Arifin WN, Yahya AS, Eow GB, et al. Motion characteristics of subclinical tremors in Parkinson's disease and normal subjects. Scientific Reports. 2022;12(1):4021.

127.   Pan D, Dhall R, Lieberman A, Petitti D. A Mobile Cloud-Based Parkinson's Disease Assessment System for Home-Based Monitoring. JMIR mHealth and uHealth. 2015;3:e29.

128.   Mohamadbeigi N, Shooshtari L, Fardindoost S, Vafaiee M, Iraji zad A, Mohammadpour R. Self-powered triboelectric nanogenerator sensor for detecting humidity level and monitoring ethanol variation in a simulated exhalation environment. Scientific Reports. 2024;14(1):1562.

129.   Panda S, Jeong H, Hajra S, Rajaitha PM, Hong S, Kim HJ. Biocompatible polydopamine based triboelectric nanogenerator for humidity sensing. Sensors and Actuators B: Chemical. 2023;394:134384.

130.   Yin F, Guo Y, Qiu Z, Niu H, Wang W, Li Y, et al. Hybrid electronic skin combining triboelectric nanogenerator and humidity sensor for contact and non-contact sensing. Nano Energy. 2022;101:107541.

131.   AlMahadin G, Lotfi A, Carthy MM, Breedon P. Enhanced Parkinson's Disease Tremor Severity Classification by Combining Signal Processing with Resampling Techniques. SN Computer Science. 2021;3(1):63.

132.   Goetz CG, Tilley BC, Shaftman SR, Stebbins GT, Fahn S, Martinez-Martin P, et al. Movement Disorder Society-sponsored revision of the Unified Parkinson's Disease Rating Scale (MDS-UPDRS): Scale presentation and clinimetric testing results. Movement Disorders. 2008;23(15):2129-70.

133.   Lu M, Zhao Q, Poston KL, Sullivan EV, Pfefferbaum A, Shahid M, et al. Quantifying Parkinson's disease motor severity under uncertainty using MDS-UPDRS videos. Medical Image Analysis. 2021;73:102179.

134.   Dai H, Zhang P, Lueth TC. Quantitative Assessment of Parkinsonian Tremor Based on an Inertial Measurement Unit. Sensors (Basel). 2015;15(10):25055-71.

135.   Goetz CG, Fahn S, Martinez-Martin P, Poewe W, Sampaio C, Stebbins GT, et al. Movement Disorder Society-sponsored revision of the Unified Parkinson's Disease Rating Scale (MDS-UPDRS): Process, format, and clinimetric testing plan. Mov Disord. 2007;22(1):41-7.

136.   Regnault A, Boroojerdi B, Meunier J, Bani M, Morel T, Cano S. Does the MDS-UPDRS provide the precision to assess progression in early Parkinson's disease? Learnings from the Parkinson's progression marker initiative cohort. Journal of Neurology. 2019;266(8):1927-36.

137.   Cronin-Golomb A, Gilmore GC, Miller IN, Neargarder S, Riedel TM, Seichepine DR. Relation of Parkinson's Disease Subtypes to Visual Activities of Daily Living. Journal of the International Neuropsychological Society. 2011;17(5):841-52.

138.   Shulman LM, Pretzer-Aboff I, Anderson KE, Stevenson R, Vaughan CG, Gruber-Baldini AL, et al. Subjective report versus objective measurement of activities of daily living in Parkinson's disease. Movement Disorders. 2006;21(6):794-9.

139.   Chandra J, Muthupalaniappan S, Shang Z, Deng R, Lin R, Tolkova I, et al. Screening of Parkinson's Disease Using Geometric Features Extracted from Spiral Drawings. Brain Sciences [Internet]. 2021; 11(10).

140.   Angeles P, Mace M, Admiraal M, Burdet E, Pavese N, Vaidyanathan R, editors. A Wearable Automated System to Quantify Parkinsonian Symptoms Enabling Closed Loop Deep Brain Stimulation. Towards Autonomous Robotic Systems; 2016 2016//; Cham: Springer International Publishing.

141.   Rovini E, Maremmani C, Cavallo F. A Wearable System to Objectify Assessment of Motor Tasks for Supporting Parkinson's Disease Diagnosis. Sensors [Internet]. 2020; 20(9).

142.   Monteiro Oliveira FH, Fernandes da Cunha D, Gomes Rabelo A, David Luiz LM, Fraga Vieira M, Alves Pereira A, et al. A non-contact system for the assessment of hand motor tasks in people with Parkinson's disease. SN Applied Sciences. 2021;3(1):11.

143.   Deuschl G, Becktepe JS, Dirkx M, Haubenberger D, Hassan A, Helmich RC, et al. The clinical and electrophysiological investigation of tremor. Clin Neurophysiol. 2022;136:93-129.

VITA